

SEASONAL CLIMATE EXTREMES: MECHANISMS,  
PREDICTABILITY AND RESPONSES TO GLOBAL  
WARMING

Mxolisi Excellent Shongwe

ISBN : 978-90-902-5046-5

SEASONAL CLIMATE EXTREMES: MECHANISMS,  
PREDICTABILITY AND RESPONSES  
TO GLOBAL WARMING

Seizoensgebonden Klimaat Extremen:  
Mechanismen, Voorspelbaarheid en Reacties op de  
Opwarming van de Aarde  
(met een samenvatting in het Nederlands)

PROEFSCHRIFT

ter verkrijging van de graad van doctor aan de Universiteit Utrecht  
op gezag van de rector magnificus, prof. dr. J. C. Stoof, ingevolge  
het besluit van het college voor promoties in het openbaar te  
verdedigen op woensdag 20 januari 2010 des morgen te 10.30 uur

door

Mxolisi Excellent Shongwe

geboren op 4 maart 1970 te Manzini, Swaziland

Promotor: Prof. dr. B. J. J. M. van den Hurk

Co-promotor: Dr. G. J. van Oldenborgh

...Dedicated to my late father John Mabhensa Shongwe

## ABSTRACT

Climate extremes are rarely occurring natural phenomena in the climate system. They often pose one of the greatest environmental threats to human and natural systems. Statistical methods are commonly used to investigate characteristics of climate extremes. The fitted statistical properties are often interpolated or extrapolated to give an indication of the likelihood of a certain event within a given period or interval. Under changing climatic conditions, the statistical properties of climate extremes are also changing. It is an important scientific goal to predict how the properties of extreme events change. To achieve this goal, observational and model studies aimed at revealing important features are a necessary prerequisite.

Notable progress has been made in understanding mechanisms that influence climate variability and extremes in many parts of the globe including Europe. However, some of the recently observed unprecedented extremes cannot be fully explained from the already identified forcing factors. A better understanding of why these extreme events occur and their sensitivity to certain reinforcing and/or competing factors is useful. Understanding their basic form as well as their temporal variability is also vital and can contribute to global scientific efforts directed at advancing climate prediction capabilities, particularly making skilful forecasts and realistic projections of extremes.

In this thesis temperature and precipitation extremes in Europe and Africa, respectively, are investigated. Emphasis is placed on the mechanisms underlying the occurrence of the extremes, their predictability and their likely response to global warming. The focus is on some selected seasons when extremes typically occur.

An atmospheric energy budget analysis for the record-breaking European Autumn 2006 event has been carried out with the goal to identify the sources of energy for the extreme event. Net radiational heating is compared to surface turbulent fluxes of energy and dynamic horizontal advection of heat. There is clear evidence that the central North Atlantic Ocean was the major source of energy for the Autumn 2006 extreme event. Within Europe, anomalously high atmospheric water-vapor loading played a significant role through its strong greenhouse effect which resulted in an increase of downwelling infrared flux to the surface.

Potential influences and connections between boreal snow cover during the melt

season (February–April) and near-surface temperature in the spring season are established. Large amounts of snow act as a precursor to cold spring seasons by altering the coupling between the land and the overlying air through a modification of the surface energy and hydrological processes. In operational numerical models, a snow signal is found to provide some seasonal forecast skill for cold spring seasons in Europe.

Changes in the intensity of droughts and floods in Africa in response to global warming are investigated and compared with changes in mean precipitation simulated by an ensemble of climate models selected from the Intergovernmental Panel on Climate Change (IPCC) fourth assessment report (AR4) set. The model simulations are objectively combined using a Bayesian weighting procedure. In southern Africa south of about 15° S, the most robust climate-change signal is a shortening of the main rainfall season. This arises from a delayed onset of seasonal rainfall associated with a reduction in lower-tropospheric moisture advection from the southwestern Indian Ocean. The semi-arid areas closer to the Kalahari desert are projected to become drier, while the wet areas are projected to become wetter. East Africa is projected to get wet in the future climate, much wetter than other regions within the same latitudinal belt. The zonal asymmetry in tropical precipitation increase is associated with a shift towards positive Indian Ocean Zonal Mode (IOZM)-like events via an alteration in the structure of the Eastern Hemisphere Walker circulation.

## CONTENTS

<i>Abstract</i> . . . . .	vi
<i>1. Introduction</i> . . . . .	1
1.1 Climate extremes . . . . .	1
1.2 Mechanisms responsible for climate extremes . . . . .	2
1.3 Seasonal predictability . . . . .	5
1.4 Future precipitation projections . . . . .	6
1.5 Objectives . . . . .	7
1.6 Questions addressed in this thesis . . . . .	8
<i>2. Energy budget of the extreme Autumn 2006 in Europe</i> . . . . .	11
2.1 Introduction . . . . .	12
2.2 Data description . . . . .	13
2.3 Analysis methods . . . . .	15
2.3.1 Atmospheric energy budget . . . . .	15
2.3.2 Atmospheric energy transport . . . . .	16
2.4 SON06 energy balance and anomalies . . . . .	17
2.5 Temporal and spatial details of the anomalies . . . . .	19
2.5.1 SON06 air temperature time series . . . . .	20
2.5.2 Sea-surface temperatures and wind . . . . .	20
2.5.3 Energy budget terms . . . . .	21
2.5.4 Cloud radiative effect . . . . .	27
2.6 Discussion and conclusions . . . . .	28
<i>3. Predictability of Cold Spring Seasons in Europe</i> . . . . .	31
3.1 Introduction . . . . .	31
3.2 Data and Methods . . . . .	33
3.2.1 CGCM predictions . . . . .	33
3.2.2 Observations . . . . .	33
3.2.3 Forecast verification . . . . .	34
3.2.4 Near-surface temperature – snow relationships . . . . .	38



3.3	Skill of MAM 2-m temperature forecasts . . . . .	39
3.3.1	Model ROC scores . . . . .	39
3.3.2	Model Brier skill scores . . . . .	41
3.3.3	Ensemble 2-m temperature predictions in eastern Europe . . . . .	41
3.4	Snow influence . . . . .	43
3.4.1	2-m temperature – snow relationships in observations . . . . .	43
3.4.2	Model snow predictions . . . . .	48
3.5	Discussion and conclusions . . . . .	52
4.	<i>Projected changes in mean and extreme precipitation in Africa under global warming. Part I: Southern Africa . . . . .</i>	56
4.1	Introduction . . . . .	57
4.2	Data and Methods . . . . .	59
4.2.1	Model simulations and observations . . . . .	59
4.2.2	Clustering stations . . . . .	62
4.2.3	Extreme value analysis . . . . .	64
4.2.4	Multi-model ensembling . . . . .	64
4.3	Projected precipitation changes . . . . .	65
4.3.1	Changes in transition season mean precipitation . . . . .	66
4.3.2	Changes in mean and extreme summer precipitation rates . . . . .	67
4.4	Projected changes in atmospheric large-scale features . . . . .	70
4.4.1	Future moisture characteristics in spring . . . . .	72
4.4.2	The tropical-temperate trough (TTT) system . . . . .	76
4.5	Discussion and conclusions . . . . .	77
5.	<i>Projected changes in mean and extreme precipitation in Africa under global warming. Part II: East Africa . . . . .</i>	82
5.1	Introduction . . . . .	83
5.2	Data and Methods . . . . .	85
5.2.1	Model simulations and observations . . . . .	85
5.2.2	Extreme value analysis . . . . .	86
5.2.3	Multi-model ensembling . . . . .	88
5.3	Changes in mean and extreme precipitation . . . . .	89
5.3.1	Short-rains season (October–December; OND) . . . . .	89
5.3.2	Long-rains season (March–May) . . . . .	91
5.3.3	Time series analysis . . . . .	91
5.4	Projected changes in large-scale forcing . . . . .	93
5.4.1	Projected OND Indian Ocean SST pattern and rainfall relationship . . . . .	94
5.4.2	Changes in Eastern Hemisphere Walker circulation . . . . .	99
5.5	Discussion and Conclusions . . . . .	100

---

<i>6. Summary and Implications</i> . . . . .	104
6.1 Summary . . . . .	104
6.2 Implications of this research . . . . .	106
<i>Appendix</i> . . . . .	108
<i>Bibliography</i> . . . . .	111
<i>Samenvatting</i> . . . . .	130
<i>Acknowledgments</i> . . . . .	134
<i>Curriculum Vitae</i> . . . . .	136
<i>Publications</i> . . . . .	137

# 1. INTRODUCTION

## 1.1 *Climate extremes*

The occurrence of extreme weather events constitutes a primary natural hazard around the globe owing to the severe impacts they often have on many aspects of human activities and on ecosystems. Extremes have deservedly attracted significant research interest and attention in recent decades (Klein Tank, 2004; van den Brink, 2005; IPCC, 2007, and many other studies). From a climatological perspective, extreme events are either those classified as rare on the basis of a predefined reference or those considered intense in terms of their absolute deviations from the norm. These two definitions are adopted in this thesis. In some climate-sensitive sectors e.g., agriculture and infrastructure, an event is classified as extreme on the basis of the losses associated with it.

Extreme events occur at various temporal and spatial scales. Compared to short-duration events, seasonal (three-month) extremes are potentially more devastating because they result from either a few extremely intense events or a persistence of anomalies of the same sign over an extended period of time. Moreover, seasonal extremes tend to affect wider areas. They therefore deserve the considerable research attention they have received in recent decades (Wehner, 2004; Tebaldi et al., 2006).

Of all climate variables, near-surface temperature and precipitation have a large impact on human activity. High-quality and long observations-derived records of these two variables are available, particularly in the northern hemisphere extratropics (e.g., Jones, 1994; Peterson et al., 1997; New et al., 2000). This permits a successful application of statistical models such as extreme value models to the archived records. Furthermore, owing to the quality of the records, a meaningful validation of climate models' precipitation and near-surface temperature simulations or a verification of operational forecasts is possible. For these reasons, this thesis focuses on an analysis of seasonal near-surface temperature and precipitation extremes, which are generally referred to as climate extremes in the discussion.

Many of the severe impacts of climate extremes are felt at regional or smaller scales. Accordingly, there is a clear incentive for the analyses of continental or

regional-scale climate extremes. The studies constituting this thesis focus on Europe and Africa.

In recent years, Europe has experienced some devastating climate extremes, some of which were record-breaking. In the summer 2002, Europe was struck by heavy precipitation leading to severe flooding in central Europe (Toothill, 2003). The following summer (2003) was extremely warm/hot and dry in many parts of Europe (Schär and Jendritzky, 2004). This extreme event resulted in severe losses, including deaths and crop failures. Owing to its adverse effects, the summer 2003 event has attracted a lot of research attention in recent years (Beniston, 2004; Luterbacher et al., 2004; Schär et al., 2004; Stott et al., 2004; Ferranti and Viterbo, 2006; Chase et al., 2006, and many others). The 2006/07 cold season (from fall to the next spring) also came as a climate surprise. Luterbacher et al. (2007) show that autumn 2006 was probably the warmest in about 500 years. Compared to the summer 2003 extreme event, underlying mechanisms responsible for the 2006/07 cold season temperature extremes have been less explored.

One of the greatest concerns regarding climate extremes is the likely change in the frequency and intensity of droughts and floods in response to global warming. The developing world, with the least adaptive capacity is most vulnerable to the severe impacts of precipitation extremes. In Africa, for instance, there is evidence of an increase in the frequency of precipitation extremes and their associated socio-economic losses in recent years (Hellmuth et al., 2007). Examples of recent precipitation extremes that have had devastating effects include: the 1997 and 2006 intense floods in East Africa, the 2009 severe drought in East Africa, the 2000 intense floods in southeastern Africa and the 2006 severe drought in southern Africa. The Sahel region of West Africa experienced prolonged drought during the 1970s and 1980s (Hagos and Cook, 2008), which had severe impacts on the economy and the population. Among others, these reasons invited an investigation of how the intensity of extreme precipitation is likely to change in future climate conditions in selected regions of Africa. The Sahelian droughts have been a subject of extensive research in recent decades (Ward, 1998; Zeng et al., 1999; Giannini et al., 2003; Lu and Delworth, 2005; Haarsma et al., 2005; Biasutti and Giannini, 2006; Cook and Vizzy, 2006, and many others), while climate extremes in southern and East Africa have received lesser research attention.

## 1.2 *Mechanisms responsible for climate extremes*

Many recent studies have tended to focus on the statistical analysis of climate extremes, whereas less attention is paid to linking the extremes to underlying physical mechanisms responsible for them (e.g., Wehner, 2004). Understanding the statistics of extremes is important as a first step. However, this has little appli-

cation in the context of the predictability of extremes, which is crucial in devising strategies that may help reduce their adverse effects. In this thesis, physical factors responsible for some of the recently observed climate extremes in Europe are investigated.

With regard to future climate conditions, confidence in the projected precipitation changes can be achieved if changes in the underlying physical mechanisms are consistent. Future changes in climate controls known to influence precipitation in southern and East Africa are also investigated and compared to the simulated changes in mean and extreme precipitation.

Climate extremes result from a combination of various mechanisms and feedbacks, and their interactions. Numerous studies have identified a wide variety of slowly evolving oceanic and land-surface conditions, and large-scale circulation patterns, which exert a discernible influence on climate variability from seasonal to longer timescales. In most cases, seasonal extreme events result from extreme phases of the various slowly evolving local, regional or remote climate controls.

The El Niño-Southern Oscillation (ENSO) (Neelin et al., 1998), a principal mode of climate variability, has been found to have a large impact on seasonal climate extremes in many locations around the world (e.g., Gershunov and Barnett, 1998; Gershunov, 1998). ENSO refers to the anomalous warming of the ocean surface in the eastern equatorial Pacific Ocean and the associated changes in the atmospheric circulation. Several studies have identified spatial locations where and seasons when extreme climate events have a discernible response to ENSO phases. In many regions, however, the ENSO signal on seasonal extremes is modulated by local controls such as sea-surface conditions from nearby oceans. The influence of the tropical Indian Ocean on extreme precipitation in southern (Washington and Preston, 2006) and East Africa (e.g., Black et al., 2003) is a prime example. The modulating effect of the North-Atlantic Ocean on European climate can be inferred from previous studies (e.g. Mathieu et al., 2004).

An influence of the Atlantic Ocean on climate variability and on seasonal extremes in Europe has been suggested (e.g., Cassou et al., 2005). One possible pathway through which North-Atlantic SSTs' signal can propagate to the European seasonal temperature field is via the North-Atlantic Oscillation (NAO; Hurrell et al., 2003). NAO refers to a vasilation in atmospheric mass between the subtropical North Atlantic close to Portugal and latitudes further north close to Iceland. The NAO, which attains its peak amplitude in boreal winter is associated with a change in low-level atmospheric circulation patterns around the mid-latitude North-Atlantic Ocean, directly impacting the seasonal climate (e.g. Hurrell and van Loon, 1997) and extremes (Scaife et al., 2008) in Europe. Temperature extremes in Europe respond much stronger to NAO than to ENSO (Kenyon and Hegerl, 2008). The relative influence of the North-Atlantic SSTs on the NAO appears debatable. Nu-

merous studies support the existence of a SST-NAO link (e.g., Peng and Robinson, 2001; Peng et al., 2003; Cassou et al., 2004) while others argue that this link is not strong enough for the purposes of NAO predictability (Doblas-Reyes et al., 2003; van Oldenborgh, 2005).

Other circulation patterns, which have been found to exert a non-negligible influence on seasonal extremes in Europe, include the northern Hemisphere annular mode (NAM; Thompson and Wallace, 2001), north-Atlantic blocking highs and mid-tropospheric troughs (Cassou et al., 2005). The NAM gives a measure of the variation in atmospheric pressure between the northern Hemisphere mid-latitudes and polar regions. In literature, the NAM is regarded as a hemispheric-scale pattern in the Northern Hemisphere north of about 20° N, while the closely related NAO refers to a Euro-Atlantic phenomenon. Kenyon and Hegerl (2008) argue that the NAM influence on temperature extremes in Europe is similar to that of the NAO, which is related to the impact that both patterns have on the mid-latitude westerlies. Blocking highs refer to large scale patterns of higher-than-average pressure that are nearly stationary in time, which block or divert the climatological westerly flow and migratory low pressure patterns into western Europe northward towards Scandinavia.

There is a growing body of evidence supporting that land-atmosphere interactions could play a significant role in forcing climate extremes in Europe, particularly the probability (Seneviratne et al., 2006) and intensity of heat waves (Ferranti and Viterbo, 2006; Fischer et al., 2007) and droughts via an alteration of the energy and hydrological cycles through soil-moisture patterns. Snow cover at the surface is potentially important in forcing climate extremes through its influence on the terrestrial energy balance by e.g., increasing the surface albedo and limiting heat fluxes through its low thermal conductivity.

The climate controls identified so far explain a small percentage of the long-term (e.g., seasonal and inter-annual) variability in temperature and precipitation in Europe. Furthermore, regional teleconnections may either be less robust or be modulated by local forcings. For instance, Yiou et al. (2007) show that while circulation features were favourable for a mild autumn 2006 in Europe, they were not unprecedented. This demonstrates that there are other important contributing factors which need to be accounted for. Therefore, there is room for further research aimed at identifying these mechanisms which vary from event to event. Mechanisms responsible for extreme events is one of the subjects investigated here. The goal is to use the findings to develop climate models to a point where skilful seasonal forecasts of climate extremes and changes in their characteristics in response to changes in atmospheric chemical composition can be made.

### 1.3 Seasonal predictability

The occurrence of record-breaking climate extremes in recent decades provides an incentive to determine and improve their predictability. Seasonal predictability refers to the ability to foretell (within some uncertainty range) what is likely to happen within the next months to a season given certain initial and slowly-evolving boundary conditions. Predictability efforts rely on purely statistical methods, numerical physically-based models or a combination of both. Statistical approaches use empirical relationships between predictor variables (e.g., sea-surface temperatures) and a response variable (e.g., air temperature). Their success is therefore dependent on availability of long records and/or stability of the statistical connections between variables. Numerical models are systems of differential equations based on the physical laws governing fluid motion, physical and chemical processes occurring within the climate system. These models are able to capture non-linear relationships between climate variables and can cope with the random dynamical nature of the earth's atmosphere. Tools used in climate prediction and a range of other issues involved are discussed by Goddard et al. (2001) and van den Hurk and Jacob (2009).

To date, predictability of large-scale controls of climate extremes beyond a certain time horizon ( $\sim 14$  days) is perceived to be quite low, particularly at higher latitudes (e.g., Johansson, 2007). Notwithstanding, potentially useful seasonal forecasts of climate extremes are possible to the extent that the slowly changing environmental factors and large-scale atmospheric circulation patterns mentioned in Sec. 1.2 and their associated climate impacts are reproducible in numerical experiments and simulations. Although the prediction information may not be very specific at spatial and temporal scales, it can still give indications of the most likely scenarios under certain conditions.

ENSO is an important factor for seasonal predictability of climate extremes in the tropical regions (Goddard et al., 2001). Its influence in the mid-latitudes remote from the Pacific Ocean (e.g., in Europe) is weaker. As discussed in Sec. 1.2, atmospheric circulation patterns such as the NAO and Atlantic–European blocking highs exert a stronger influence on climate extremes in Europe than ENSO. For example, during the exceptionally warm summer 2003, two warm regimes (blocking and the Atlantic low) persisted much longer than on average (Cassou et al., 2005) in the Atlantic–European area. The fact that the predictability of atmospheric circulation in Europe is low (Palmer et al., 2004) places a limit on the seasonal predictive skill of climate extremes that can be achieved on the basis of atmospheric circulation.

Several studies have attributed the European summer 2003 extreme event to soil-moisture deficits in southern Europe (Ferranti and Viterbo, 2006; Vautard et al., 2007). The weaker influence of neighboring SSTs relative to soil-moisture condi-

tions in summer 2003 (Ferranti and Viterbo, 2006) demonstrates the importance of land-atmosphere coupling for predicting climate extremes in Europe. There is also modelling evidence that land-surface-atmosphere coupling from snow properties can offer an improved seasonal climate prediction skill in Europe (Douveille, 2009). The effect of snow on European climate extremes and their predictability is investigated in this thesis (see Sec. 1.6).

An assessment of seasonal predictability of climate extremes can be done using hindcasts/forecasts from state-of-the-art climate models which are used operationally by several groups within Europe and elsewhere. Both in the model world and in observations, seasonal climate extremes are defined based on a threshold exceedance. Probabilistic forecasts can be derived from ensemble prediction systems. By quantitatively comparing the model simulations with observations, an estimate of the predictive skill of extremes can be made. Jolliffe and Stephenson (2003) present an overview of the standard measures of forecast skill in atmospheric sciences. Various scores are used to measure different aspects of forecast performance. For instance, the relative operating characteristic (ROC; Mason and Graham, 1999) measures a model's ability to discriminate between events and non-events. Reliability diagrams and rank histograms are used to detect model under- or over-confident predictions (Mason and Mimmack, 2002). Several skill scores such as the Brier skill score (BSS) and the ranked probability skill score (RPSS; Weigel et al., 2007) which measure the improvement of the model forecasts over a reference system are also in use.

#### 1.4 *Future precipitation projections*

Potential changes in mean precipitation, and in the frequency and intensity of droughts and floods in many parts of the globe (including Africa) have been a focus of many climate studies in recent years. In general, there are indications for wetter conditions in the wet mid-latitudes and tropical regions, and drying in the sub-tropics in the future climate (IPCC, 2007, and references therein). However, in cases when the interannual precipitation variability also increases, changes in extreme seasonal rainfall may not parallel those of mean annual or seasonal rainfall. Also, regional and local features induce inhomogeneities in the precipitation response to global warming. Therefore, the need to determine changes in the intensity of precipitation extremes at regional rather than global scales is evident. However such regional scale studies are still few, particularly in Africa, where they are supposed to be natural priorities because of the rising trends of extremes and their devastating effects (Hellmuth et al., 2007; van Aalst et al., 2007).

Most climate change studies where Africa is included have identified certain regions where mean or extreme precipitation changes across the IPCC AR4 mod-



els are consistent (Kharin et al., 2007). However, even where models agree, the physical mechanisms through which the climate signal will propagate to the precipitation field remain uncertain. They therefore deserve more research attention. Likely candidates include the role of sea-surface temperatures and their associated teleconnection patterns (e.g., Nicholson and Kim, 1997), atmospheric circulation features (e.g., Todd and Washington, 1999) and atmospheric moisture characteristics, which are influenced by moisture fluxes and soil-moisture-precipitation feedbacks (e.g., Cook et al., 2006).

Despite of the significant progress made in numerical model development, many uncertainties in simulating the future climate exist. These arise from natural variability, model errors and emission scenarios used to force the models. For this reason, no single climate model is considered accurate (i.e., free from biases). For example, Hoerling et al. (2006) show that most models fail to reproduce the pattern of the late twentieth century drying in southern and West Africa. A considerable inter-model spread is also found. This demonstrates a need for objective methods to be used in combining model simulations such that the least performing models are downweighted. This has become an area of active research (e.g., Giorgi and Mearns, 2002; Tebaldi et al., 2005; Smith et al., 2008; Tebaldi and Sanso, 2008) whose findings have found useful application in this thesis.

Trends in twentieth century climate extreme indices in southern and East Africa have been detected (New et al., 2006). An observation of this trend, particularly that of precipitation extremes provided the motivation for the Netherlands Red Cross/Red Crescent (RC/RC) Climate Centre coordinated research project. In this research project, an analysis of projected changes in several characteristics of precipitation in almost the whole of sub-Saharan Africa was carried out. Changes in mean seasonal rainfall, the intensity of precipitation extremes and the rainfall seasonal cycle were investigated. A time-series analysis of the precipitation simulations was also carried out. Some results from the RC/RC project form part of this thesis (Chapters 4 and 5). Other results are available on the KNMI Africa scenarios web-site ([http://www.knmi.nl/africa\\_scenarios/](http://www.knmi.nl/africa_scenarios/)).

## 1.5 Objectives

The main goal of the studies presented in this thesis is to go beyond the statistical analyses of seasonal extremes and provide a physical explanation of why they occur. We also investigate the extent to which adequate representation of the underlying mechanisms leads to skilful seasonal forecasts in current operational numerical models. Furthermore, possible future changes in the forcing factors are probed and linked to those of mean and extreme precipitation. The findings herein are expected to inspire their validation through numerical experiments.

Ultimately, the findings can contribute to the global scientific effort aimed at advancing capabilities for predicting climate extremes and making realistic future projections. To achieve our goals, two questions are posed:

- **Which fundamental physical linkages associated with the occurrence of seasonal climate extremes need to be represented comprehensively in numerical models in order to improve the prediction skill of the extremes?**
- **How consistent are the projected changes of climate extremes in Africa and their underlying mechanisms in climate change scenarios?**

To accomplish our scientific objectives, observations, reanalysis data, and climate model simulations and forecasts are used. To seek answers to the key questions, we break them down into the specific questions listed below.

### 1.6 Questions addressed in this thesis

- **WHAT PHYSICAL MECHANISMS WERE RESPONSIBLE FOR THE RECORD-BREAKING MILD AUTUMN 2006 SEASON IN EUROPE? *Chapter 2***

Excessive atmospheric energy/heat was an essential ingredient for the occurrence of the Autumn 2006 extremely mild episode. To have a deeper understanding of the underlying physical mechanisms and their temporal evolution, an investigation of the major regional energy sources and sinks, and possible interactions between them is a prerequisite. An understanding of the mechanisms responsible for this extreme event has a potential for significant contributions towards exploring the predictability potential of the occurrence of similar events in future.

In **Chapter 2** (*published in Climate Dynamics*), an observational analysis of the atmospheric energy budget for the exceptionally mild Autumn 2006 in Europe is undertaken. Top of the atmosphere (TOA) and surface radiation, surface turbulent fluxes and lateral energy-transport-convergence terms are investigated for their relative contributions in forcing the extreme event. Factors that influence the atmospheric energy budget such as clouds and water vapor, and their effect on the regional radiation budget are also considered.

- **ARE THE MECHANISMS IMPORTANT FOR SKILFUL FORECASTS OF COLD SPRING SEASONS ADEQUATELY REPRESENTED IN CURRENT OPERATIONAL, SEASONAL FORECAST MODELS? *Chapter 3***

Similar to other mid-latitude regions, seasonal predictability of near-surface temperature in Europe remains low. There has been some hope that some NAO-related

predictability could be achieved particularly during the Northern Hemisphere winter (Rodwell, 2003). Outside the winter, the influence of other slowly-varying boundary conditions have a larger influence relative to the largely unpredictable atmospheric circulation. Factors such as SST in coastal areas (van den Dool and Nap, 1985), snow (Douville, 2009) and soil moisture (Douville, 2000b; Douville and Chauvin, 2004) give rise to seasonal predictability in these seasons. In eastern Europe, an area classified as being sensitive to snow during the cold season (Groisman et al., 1994), some potential predictability may exist. It is well known that snow cover and snow depth are variables that can potentially have an impact on cold temperature extremes, particularly in snow transient regions. It is surprising though that in contrast to the oceanic parameters, the predictability of snow and its influence on climate predictability and extremes in Europe have received less research attention.

In **Chapter 3** (*published in Monthly Weather Review*), an objective verification of cold spring hindcasts/forecasts produced by three operational numerical models is carried out. A lag-relationship between snow and near-surface temperature during spring in eastern Europe is established. The predictability of snow and the migration of the snow-line during the melt season in the operational models is assessed. Evidence of useful predictability of extremely cold spring seasons in Europe has emerged.

- **HOW DO CHANGES IN FACTORS KNOWN TO CONTROL SEASONAL TO INTERANNUAL RAINFALL VARIABILITY IN AFRICA RELATE TO CHANGES IN THE INTENSITY OF EXTREMELY WET AND DRY SEASONS IN AFRICA IN IPCC MODELS?**  
*Chapters 4 and 5*

A rigorous regional statistical analysis has been carried out to investigate how seasonal mean and extreme precipitation in Africa are projected to change by a subset of climate models selected from the Intergovernmental Panel on Climate Change (IPCC) Fourth Assessment Report (AR4) ensemble. The changes are estimated from a fractional change in statistics computed in the control simulations and those forced by the intermediate SRES A1b scenario. The analyses have been carried out on objectively delineated climate zones of smaller spatial scale than the commonly used Giorgi regions (Giorgi and Francisco, 2000). Extreme value statistical theory (Coles, 2001) has been applied to estimate the intensity of observed and model simulated 10-year droughts and floods. Anderson-Darling goodness-of-fit tests (Laio, 2004) are performed. The model simulations are then combined through an unequal weighting procedure based on Bayesian statistics (Tebaldi et al., 2005). The Bayesian procedure attempts to penalize models that show significant biases in their twentieth century precipitation simulations, particularly when they are outliers with respect to the large ensemble in their future climate simulations.

In **Chapter 4** (*published in Journal of Climate*) projected changes in mean and extreme precipitation in southern Africa are investigated. With the precipitation annual cycle in mind, changes in mean precipitation during the transition seasons (i.e. austral spring and autumn) are investigated. This is to identify any changes in the duration of the rainy season, which typically spans September of one year to about the following May. Moisture availability, mainly from advection, which influences the rainfall onset, is also investigated and associated with the changes in rainfall during the onset season.

The analysis of changes in extreme precipitation are undertaken during the peak of the rainy season (December–February). The likely future behavior of the tropical-temperate-trough system (TTT; Washington and Todd, 1999), a major rain-bearing mechanism in southern Africa (Kuhnel, 1989) is probed and linked to the projected changes in precipitation patterns.

The results presented in **Chapter 5** (*submitted to Journal of Climate*) apply the same statistical analysis to East Africa precipitation data. Because of its geographical location, East Africa has both bimodal and unimodal rainfall regimes. Our focus has been on the peak of the rainfall seasons in each regime. In East Africa, interannual rainfall variability and seasonal extremes respond to the Indian Ocean zonal mode (IOZM) during boreal autumn. The extent to which the IOZM-rainfall relationship is reproduced by IPCC AR4 models is assessed. We further establish likely changes in the tropical Indian Ocean zonal SST gradients and their consequences for the IOZM probability-density function. Possible alterations in the structure of the eastern Hemisphere zonal circulation, which communicates the IOZM signal on rainfall, are also investigated.

The main findings from our research aimed at answering the above questions are summarized in **Chapter 6** concluding with some recommendations.

## 2. ENERGY BUDGET OF THE EXTREME AUTUMN 2006 IN EUROPE

Autumn 2006 was extraordinarily mild in many parts of Europe. Near-surface temperatures were more than three standard deviations above the 1961–90 climatology. Even accounting for global warming, this event was far outside the probability density function (PDF) of previous observations or climate model simulations. To investigate the mechanisms behind this event, the energy-budget for Autumn 2006 in Europe is estimated. Atmospheric energy-transport convergence over Europe is calculated and compared with the net energy flux at the top of the atmosphere (TOA) as well as at the earth's surface.

The central North-Atlantic Ocean constituted the major source of energy. Here, the release of both sensible and latent heat was anomalously high. Atmospheric circulation played a crucial role by transporting the excess energy into Europe. Of this energy excess, dry-static energy was larger than the latent part, partly due to an additional contribution derived from a conversion of latent energy to sensible heat, which occurred upstream of the study area in the eastern Atlantic. In Europe, surface turbulent-energy fluxes into the atmosphere respond to atmospheric energy-transport convergence and are accordingly suppressed due to the anomalously high temperature and humidity content of the overlying air. The net outflow of radiational energy to space is anomalously high but not sufficient to offset the large positive anomaly of energy found over Europe.

Even though the relative humidity was near its normal values in Europe, the specific humidity was considerably higher than usual. The high water-vapour content induced a local radiative positive feedback, increasing the opacity of the atmosphere to long-wave radiation. This appears to have significantly contributed to the extreme event. Atmospheric circulation played a crucial role in sustaining this feedback loop.

---

This chapter is based on the article “Energy budget of the extreme Autumn 2006 in Europe.” by Mxolisi E. Shongwe, Rune G. Graversen, Geert Jan van Oldenborgh, Bart J. J. M. van den Hurk, and Francisco J. Doblas-Reyes, 2009, published in *Climate Dynamics* doi:10.1007/S00382-009-0689-2.

## 2.1 Introduction

Mean and extreme climate conditions are changing in many parts of the globe, partly as a response to anthropogenic changes in the chemical composition of the earth's atmosphere (IPCC, 2007). Mean and extreme temperatures are directly affected by changes in radiative forcing. Changes in global temperature extremes have attracted much interest in recent years (Alexander et al., 2006), primarily because of their impact across different sectors such as terrestrial ecosystems (Ciais et al., 2005). There has also been growing interest in studying changes in continental scale temperature variability and extremes (Klein Tank and Können, 2003; Klein Tank et al., 2006).

Increases in the severity of temperature extremes in Europe over the past century, with the warmest events occurring in the last few years (since the mid 1990s) are reported (Xoplaki et al., 2005). Superimposed within the gradual warming are episodic extreme events such as summer (June–August) 2003 (Schär et al., 2004; Beniston, 2004; Ferranti and Viterbo, 2006; Fischer et al., 2007), autumn (September–November) 2006 (Luterbacher et al., 2007; van Oldenborgh, 2007; Yiou et al., 2007) and winter (December–February) 2006/07 (Luterbacher et al., 2007; Yiou et al., 2007). The extent to which Autumn 2006 (hereafter SON06) was exceptionally warm has been documented (van Oldenborgh, 2007, hereafter GJvO07). After removing the effect of global warming in the temperature time series, GJvO07 showed that the lower bound of the 95% confidence interval of the return period corresponding to SON06 was 200 years in parts of Germany. In qualitative agreement with GJvO07, Luterbacher et al. (2007) used observed and reconstructed temperatures (from 1500) to show that SON06 was probably the warmest autumn in 500 years. The probability of warm extremes is likely to increase in the 21st century in Europe, particularly during summer months (Beniston et al., 2007; Sterl et al., 2008, among many others). In autumn, most climate models show a shift in the location of the probability density function (PDF). It is therefore crucial to investigate the mechanisms underlying an event such as SON06, and to what extent they are represented in current climate models. The extreme SON06 has recently been attributed to south-westerly atmospheric circulation anomalies that advected warm air from the eastern subtropical Atlantic Ocean (Luterbacher et al., 2007). GJv07 and Cattiaux et al. (2009) confirm that this anomaly was to a large extent forced by atmospheric circulation. Using a linear regression model, in which circulation was one of the predictors, GJvO07 was able to reproduce a large fraction of the observed near-surface temperature anomalies. Yiou et al. (2007) argue, however, that although atmospheric circulation was favourable for the warmer conditions during SON06, the intensity of the anomalies by far exceeded those previously recorded when similar flow regimes were prevalent. Of the 91 fall days,  $\sim 43$  (i.e. 47%) had a temperature anomaly

warmer than that of the same date during 10 previous analogue years in terms of atmospheric flow regimes (Yiou et al., 2007). In addition, a recent study by Cattiaux et al. (2009), using both a linear regression technique and a regional model, links  $\sim 50\%$  of the SON06 surface-temperature anomalies over the European continent to atmospheric dynamics, and 30% to eastern North-Atlantic sea-surface temperature anomalies.

Other factors may also be important: changes in solar irradiance, heat transported by the oceans affecting the surface heat fluxes, effects of clouds and other local feedback mechanisms, all factors that are important for the energy balance of the earth's atmosphere. The present study extends the work of GJvO07 by calculating the atmospheric energy budget for SON06 in Europe. This study is done on the premise that energy available to the European atmosphere during SON06 exceeded its long-term autumn average. It is assumed that the European Centre for Medium-Range Weather Forecasts (ECMWF) ERA-Interim represents fields of radiation and surface turbulent energy fluxes quite well. These fields are estimated as forecasts by the background model. By making a synthesis of all the energy-budget components and fluxes in the region of Europe that experienced the largest temperature anomalies, the underlying factors responsible for this extreme event are identified. These factors are linked to their possible forcings such as circulation, cloudiness and humidity. The analyses reveal energy sources and sinks, and provide a holistic view of the relative importance of the different forcing factors underlying the extreme SON06 temperatures.

## 2.2 Data description

The ERA-Interim (1989–2006) reanalysis and forecast fields form the major input for the present study. Six-hourly fields of analysed horizontal wind, temperature and specific humidity are obtained from the reanalysis data (Simmons et al., 2006; Uppala et al., 2008). The six-hourly resolution data are then converted into daily fields for each day ( $D$ ) through a weighted average which assigns 0.125, 0.25, 0.25, 0.25 and 0.125 to the  $00_D$ ,  $06_D$ ,  $12_D$ ,  $18_D$  and  $00_{D+1}$  data, respectively. These fields are used to compute the energy tendency and transport. In all cases, 3D fields are taken at model levels.

The surface and top-of-the-atmosphere (TOA) fluxes are obtained from forecast fields of short-wave and infrared radiation, and sensible and latent heat at the surface. Clear-sky radiative fluxes are used to estimate the effect of clouds. These fluxes are provided as accumulated quantities over the forecast period. Forecasts are initialized from the ERA-Interim analyses once every 12 hours (at 00 and 12 GMT). The sum of the fluxes over the first 12 hours of the two daily forecasts is used as the daily value. Results obtained using the 24 hour accumulations are very

similar.

Near-surface and 300-hPa temperature anomalies from the ERA-Interim analysis and NCEP/DOE Reanalysis II (Kanamitsu et al., 2002) are displayed in Fig. 2.1. The two analysis fields agree as regard the hot spot over Europe ( $10^{\circ}$  W– $20^{\circ}$  E,  $40^{\circ}$ – $60^{\circ}$  N; rectangular area in Fig. 2.1). Near the surface, the temperatures exceeded three standard deviations of September–November (SON) interannual variability in both datasets. The near-surface temperature anomalies shown here are consistent with GJv007 and Luterbacher et al. (2007), who also show absolute surface-air-temperature anomalies. In both datasets used here, the temperature anomalies in Europe have a barotropic structure extending throughout the troposphere (up to 300-hPa).

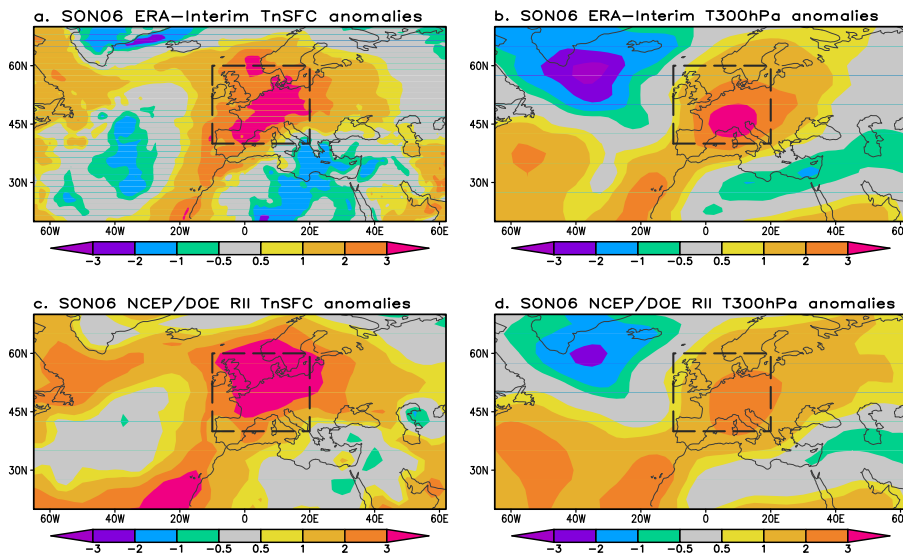


Fig. 2.1: SON06 near-surface (TnSFC) and 300-hPa (T300hPa) temperature anomalies for ERA-Interim (a, b) and NCEP/DOE Reanalysis II (c, d) data. Temperature anomalies are expressed in terms of SON interannual standard deviations ( $\sigma$ ) based on the 1989–2005 period. The area within Europe where the temperature anomalies have the largest amplitude in both datasets (i.e.  $10^{\circ}$  W –  $20^{\circ}$  E,  $40^{\circ}$  –  $60^{\circ}$  N) is enclosed with the dashed rectangular box.



### 2.3 Analysis methods

In this study, the atmospheric energy budget is analysed. An analysis of energy fluxes is also provided in order to reveal the sources and sinks of energy during SON06.

#### 2.3.1 Atmospheric energy budget

The energy budget can be expressed as the time rate of change of atmospheric energy ( $E_v$ ) due to (i) convergence of lateral energy transport by the horizontal wind ( $\mathbf{v}$ ), (ii) radiational fluxes at the top of the atmosphere (TOA), (iii) radiational fluxes at the surface (SFC), and (iv) surface turbulent fluxes:

$$\frac{\partial \langle E_v \rangle}{\partial t} = -\nabla \cdot \langle \vec{v} E_p \rangle + R_{TOA} + R_{SFC} + LH + SH. \quad (2.1)$$

Here, using  $\eta$ ,  $g$  and  $p(\eta)$  to denote model levels, gravitational acceleration and pressure, respectively. For a general variable  $X$ , the column integral is represented as

$$\langle X \rangle = \frac{1}{g} \int_0^1 X \frac{\partial p}{\partial \eta} d\eta. \quad (2.2)$$

$R_{TOA}$  and  $R_{SFC}$  correspond to the radiative fluxes at the top of the atmosphere and surface, respectively.  $LH$  and  $SH$  are the net upward turbulent fluxes of latent and sensible heat, respectively. Reanalysis data do not fully fulfill the budget in Eq. 2.1. An imbalance between the terms is introduced during the assimilation process where an analysis is obtained as a weighted average between observations and first-guess model estimates. This step does not necessarily conserve energy as well as mass.

The total atmospheric energy ( $E_v$ ) is calculated from the sum of the internal energy ( $c_v T$ ), potential energy ( $\Phi$ ), latent energy ( $L_v q$ ) and kinetic energy  $[(u^2 + v^2)/2]$  as

$$E_v = c_v T + \Phi + L_v q + \frac{1}{2}(u^2 + v^2). \quad (2.3)$$

Atmospheric energy is hence computed from the temperature ( $T$ ), geo-potential ( $\Phi = gz$ ), specific humidity ( $q$ ) and wind velocity ( $u, v$ ) fields. The quantities  $c_v$  and  $L_v$  correspond to the specific heat capacity of air at constant volume and the latent heat of vaporization, respectively.  $E_p$  in the first term on the right in Eq. 2.1 is calculated as  $E_v$  in Eq. 2.3 by substituting  $c_v$  with  $c_p$ , the specific heat capacity of air at constant pressure, in order to cater for the pressure-work term. Both  $c_v$  and  $c_p$  vary as a function of atmospheric moisture content.

Mass-flux inconsistencies have been encountered in a previous ECMWF reanalysis (Graversen et al., 2007). Such inconsistencies introduce errors in the fluxes of energy and its divergence (Trenberth et al., 2002). Therefore, a mass-flux correction has been performed following Trenberth (1991). Basically, a mass-flux correction involves a removal of a wind residual so that the continuity constraint of dry air is not violated. Graversen (2006) provides a brief description of the procedure used for the mass-flux correction in this study.

### 2.3.2 Atmospheric energy transport

The vertically integrated energy-transport vector ( $\mathbf{F}$ ) is given by

$$\mathbf{F} = \langle \vec{v} E_p \rangle. \quad (2.4)$$

The convergence of energy transport per unit area within the domain is obtained for each time step from the differences in the normal components of the energy-transport vector [ $\mathbf{F} = (F_\lambda, F_\phi)$ ] across the longitudinal and latitudinal walls encompassing the European study domain (i.e.  $\lambda_W = 10^\circ \text{ W}$ ;  $\lambda_E = 20^\circ \text{ E}$ ;  $\phi_S = 40^\circ \text{ N}$ ;  $\phi_N = 60^\circ \text{ N}$ ):

$$\begin{aligned} \frac{1}{A} \int_{\phi_S}^{\phi_N} \int_{\lambda_W}^{\lambda_E} (\nabla \cdot \mathbf{F}) R^2 \cos \phi d\lambda d\phi &= \frac{1}{A} \left[ \int_{\phi_S}^{\phi_N} (F_\lambda|_{\lambda=\lambda_W} - F_\lambda|_{\lambda=\lambda_E}) R d\phi \right. \\ &\quad \left. + \int_{\lambda_W}^{\lambda_E} (F_\phi|_{\phi=\phi_S} - F_\phi|_{\phi=\phi_N}) R \cos \phi d\lambda \right], \end{aligned} \quad (2.5)$$

where  $R$  is the earth's radius and

$$A = \int_{\phi_S}^{\phi_N} \int_{\lambda_E}^{\lambda_W} R^2 \cos \phi d\lambda d\phi \quad (2.6)$$

is the area enclosed by the study domain.

The seasonal mean convergence field ( $-\nabla \cdot \langle \vec{v} E_p \rangle$ ) is computed at each grid point followed by a nine-grid-point smoother. The energy-transport vector is then decomposed into its divergent and non-divergent components, which are derived from the potential ( $\chi$ ) and streamfunction ( $\psi$ ) fields, respectively. Energy transport divergence, which equals the Laplacian of the potential, balances the atmospheric energy sources and sinks. Since the objective of this study is to identify the sources of energy during SON06, only results for the divergent component of the energy-transport vector are shown.

## 2.4 SON06 energy balance and anomalies

In addition to the energy-budget terms shown in Eq. 2.1, another combination of radiation terms is more fruitful for this study. Instead of combining all fluxes at the surface (and at the top of the atmosphere), all long-wave fluxes are combined. This combination enables a derivation of an atmospheric net long-wave radiative feedback (AnLWRF). Following the same approach as Raval and Ramanathan (1989), the AnLWRF is defined as the emitted surface upward long-wave radiation (SuLWR) not escaping to space as top net long-wave radiation (TnLWR), i.e.,  $\text{AnLWRF} = \text{SuLWR} - \text{TnLWR}$ . Raval and Ramanathan (1989) refer to AnLWRF as the *greenhouse effect*. Using AnLWRF is preferred here to avoid confusion with the anthropogenic greenhouse effect, which is not directly estimated.

Downwelling long-wave radiation (DLWR) is the energy reaching the earth's surface from the atmosphere. It varies as a function of atmospheric temperature. This field is available on the ERA-Interim archive. As conventional, DLWR is related to the other surface infrared fluxes through  $\text{DLWR} = \text{SuLWR} - \text{SnLWR}$ .

The individual terms in the energy budget (Eq. 2.1) and the derived variables, averaged in space (over Europe) and time are presented in Table 2.1. The energy acronyms used in this paper are defined in this table. Also shown are the corresponding climatological values calculated over the 1989–2005 period, and the temporal correlation between the anomalies of the energy-budget terms, and those of the near-surface and vertically-averaged air temperature during SON06. Detailed discussions of these results are deferred to the next sections. The imbalance (error) in the budget adds up to  $+7.9 \text{ Wm}^{-2}$  ( $+11.5 \text{ Wm}^{-2}$ ) during SON06 (SON 1989–2005). In terms of absolute magnitude, the error is smaller than all terms except the energy tendency and surface sensible-heat flux.

SON06 anomalies (deviation from the 1989–2005 climatology) of energy-budget terms are shown schematically in Fig. 2.2. These anomalies, derived directly from Table 2.1 are spatially and temporally averaged. According to the sign convention adopted throughout this paper (except when otherwise noted), all fluxes are counted positive into the atmosphere. Using this convention, TOA fluxes are positive downward and surface fluxes are positive upward. An anomaly in TnSWR of  $\sim 3.4 \text{ Wm}^{-2}$  is approximately compensated by an anomaly ( $\sim 3.6 \text{ Wm}^{-2}$ ) in radiative loss by TnLWR.

Noteworthy, a large anomaly ( $\sim 16.5 \text{ Wm}^{-2}$ ) of horizontal energy-transport convergence is found. This result, which shows an excess energy transport across the lateral boundaries into Europe (i.e. a smaller than normal advective energy loss), is in qualitative agreement with previous findings (GJvO07; Luterbacher et al., 2007; Cattiaux et al., 2009). Associated with this anomaly in energy-transport convergence is anomalous DLWR, which is  $\sim 8.9 \text{ Wm}^{-2}$  above its long-term mean. Yiou et al. (2007) noted that energy transported by atmospheric circulation is not

Tab. 2.1: Summary of the budget terms over Europe.

Budget component	Notation	SON06 Mean <sup>¶</sup> (Wm <sup>-2</sup> )	SON Clim. <sup>§</sup> (Wm <sup>-2</sup> )	Corr <sup>ℓ</sup> <sub>[T2m]</sub> (%)	Corr <sup>ℓ</sup> <sub>[Ta]</sub> (%)
Energy tendency	$\frac{\partial E_v}{\partial t}$	-7.4	-12.1 (3.9)		
Energy transport divergence	$\nabla \cdot \vec{V} E_p$	<b>-49.8</b>	-33.3 (9.4)	<b>-24</b> <sup>†</sup>	<b>-21</b> <sup>†</sup>
Top net short-wave radiation	TnSWR	+137.7	+134.3 (2.6)	-06	+20
Top net long-wave radiation	TnLWR	-229.9	-226.3 (2.3)	-02	<b>-31</b> <sup>†</sup>
Surface net short-wave radiation	SnSWR	-84.8	-82.1 (2.7)	+15	-11
Surface net long-wave radiation	SnLWR	+56.0	+55.7 (1.7)	<b>-56</b> <sup>‡</sup>	<b>-35</b> <sup>‡</sup>
Surface latent-heat flux	LH	+51.3	+52.7 (2.1)	<b>-68</b> <sup>‡</sup>	<b>-71</b> <sup>‡</sup>
Surface sensible-heat flux	SH	<b>+4.6</b> <sup>†</sup>	+8.7 (1.3)	<b>-78</b> <sup>‡</sup>	<b>-68</b> <sup>‡</sup>
Error		+7.9	+11.5		
Downwelling long-wave radiation	DLWR	<b>+312.2</b> <sup>‡</sup>	+303.3 (2.3)	<b>+82</b> <sup>‡</sup>	<b>+57</b> <sup>‡</sup>
Atmospheric net long-wave radiation feedback	AnLWRF	<b>+138.3</b> <sup>†</sup>	+132.8 (2.2)	<b>+47</b> <sup>‡</sup>	+01

<sup>¶</sup> SON06 mean values falling outside the 90% confidence interval of the SON climatology ( $\bar{X}$ ) are printed in bold. Those that fall outside the 95% (99%) confidence interval are shown by † (‡).

<sup>§</sup> SON climatology ( $\bar{X}$ ) is defined using the 1989–2005 period. The standard deviation ( $\sigma$ ) of the individual SON means, computed over the climatological period is enclosed in parentheses. The 100(1 -  $\alpha$ )% confidence interval of  $\bar{X}$  is then  $\bar{X} \pm Z_{\alpha/2}\sigma$ , where  $Z_{\alpha/2}$  is the (1 -  $\alpha/2$ )% quantile of the standard Gaussian distribution and  $\alpha$  is the significance level.

<sup>ℓ</sup> Simultaneous correlations between each component, and 2m temperature (fifth column) and vertically-averaged air temperature (sixth column) are expressed as percentages. Significant correlations at the 5% (1%) level, obtained from a  $t$ -test, are shown by † (‡).

sufficient to explain the fact that the SON06 extreme event was unprecedented. Figure 2.2 indicates a large anomaly ( $\sim 5.5 \text{ Wm}^{-2}$ ) in AnLWRF. In Sec. 2.5.3, it is shown that the AnLWRF is linked to an anomalously large water-vapour content and the authors argue that it played a major role for the SON06 extreme event. At the earth's surface, most fluxes are negative indicating a downward anomaly. The spatial and temporal variations of the anomalies in energy-budget terms presented in Fig. 2.2 are discussed in Sec. 2.5 below.

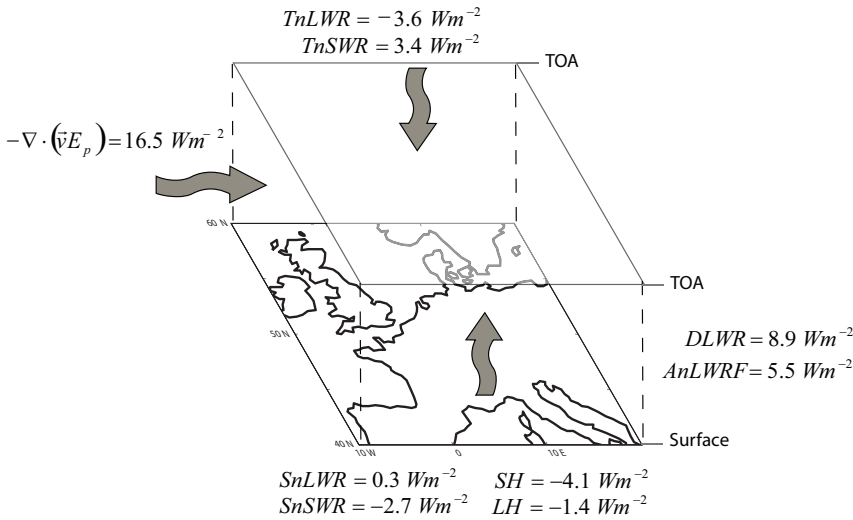


Fig. 2.2: SON06 atmospheric energy-budget anomalies over Europe. The arrows show energy-flux anomalies at the earth's surface (bottom arrow), within the atmosphere (left arrow) and at the TOA (top arrow). Acronyms are as defined in Table 2.1.

## 2.5 Temporal and spatial details of the anomalies

In Table 2.1 and Fig. 2.2, it has been shown that energy-transport convergence, and the AnLWRF deviated significantly from their long-term (1989–2005) ERA-Interim climatology during SON06. The authors argue that these are fundamental factors responsible for the SON06 extreme event. In this section, some evidence supporting this argument is presented. Before proceeding with a discussion of the energy terms, some relevant aspects of the SON06 season are shown.

### 2.5.1 SON06 air temperature time series

Daily fluctuations of SON06 air-temperature (at 2 metres and vertically averaged) anomalies are shown in Fig. 2.3b. In this plot, anomalies are defined relative to the first harmonic of the annual cycle (Fig. 2.3a). It is evident that the warm anomaly was roughly persistent, with only a few cold episodes during the first week of November. A cold spell was preceded by pronounced energy divergence within the domain (cf. Fig. 2.6a). Despite the large amplitude of this cold anomaly, the seasonal-mean anomaly was highly positive due to persistent warm-than-usual conditions during the rest of the season. The vertically averaged air-temperature anomalies vary in phase with the near-surface temperatures (correlation = 0.78). This confirms that the SON06 temperature anomalies had a quasi-barotropic structure over Europe.

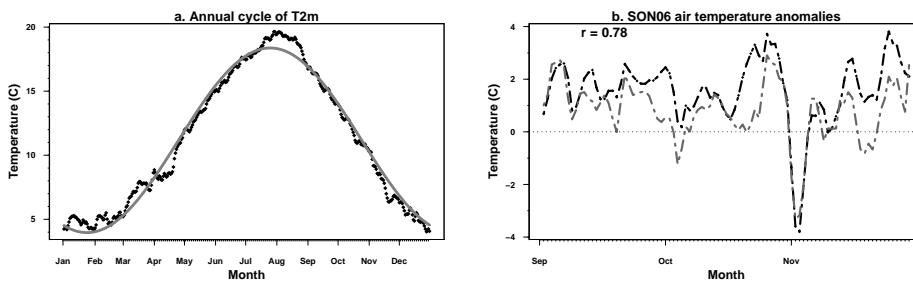


Fig. 2.3: a) Annual cycle of daily 2m temperature (T2m) over Europe (black dots) and the first harmonic (solid gray line). b) Anomalies of SON06 daily 2m temperature (black line) and vertically-averaged air temperature (gray line). The anomalies in b) are departures from the first harmonic of the mean annual cycle, which captures  $\sim 98\%$  ( $\sim 97\%$ ) of the 2m temperature (vertically-averaged air temperature) variance. The correlation between the two series in b) is 0.78 (displayed).

### 2.5.2 Sea-surface temperatures and wind

Owing to their importance in determining net energy exchange at the surface, North-Atlantic sea-surface-temperature (SST) anomalies and near-surface (10m) wind anomalies are shown in Fig. 2.4. Figure 2.4a shows warmer SSTs in the eastern North-Atlantic boundary, the Mediterranean, and the high latitude Atlantic seas between New Foundland and Norway. The anomalies exceed  $1^\circ\text{C}$  over the seas bordering Africa, Europe and eastern Canada. The eastern North-Atlantic-boundary SST anomalies have been estimated to explain  $\sim 30\%$  of the SON06 warming by Cattiaux et al. (2009).

A near-surface cyclonic anomaly, centred south of Iceland, is found above the North-Atlantic Ocean (Fig 2.4b). This anomaly has an equivalent barotropic structure (not shown) and is generally similar to the zonal regime mentioned by Yiou et al. (2007) at 500-hPa, which occurred most frequently ( $\sim 38\%$ ) during the extended period September–February 2006/07. Winds are anomalously strong over the North-Atlantic north of  $\sim 40^\circ$  N but weaker than normal close to the African coast.

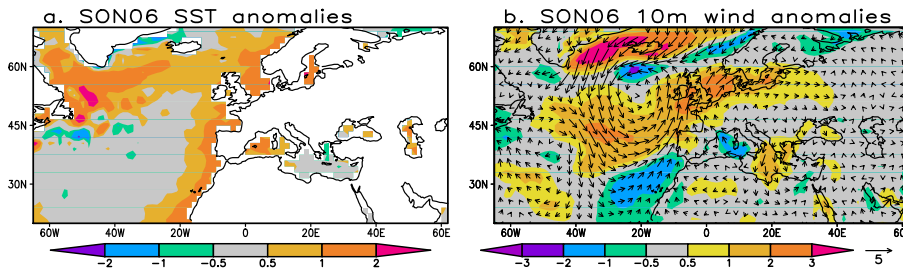


Fig. 2.4: SON06 a) North-Atlantic-Ocean SST anomalies ( $^\circ\text{C}$ ) and b) 10m wind anomalies. Arrows in b) display the direction of the anomalous winds whereas the shading indicates their speed ( $\text{ms}^{-1}$ ).

### 2.5.3 Energy budget terms

The anomalies for the energy components are placed in a large scale context by examining geographical distributions of time-averaged quantities. The main goal is to show sources and sinks of energy. In order to allow for a visualization of the temporal distribution of the temperature and energy components in time, the SON06 un-smoothed daily time series are also presented. The time-series presented in this section are spatially averaged over the Europe study area. Both temperature and energy-budget terms undergo an annual cycle which is taken to be the first harmonic of the 1989–2005 ERA-Interim climatology. Departures from this annual cycle form the basis of the time-series results presented in ensuing subsections.

#### *Energy transport*

The total energy-flux anomalies have been decomposed into a dry-static and a latent part in order to allow for a visual comparison of their relative importance. Flux-divergence anomalies for these two energy components are shown in Fig. 2.5.

Superimposed on the divergence anomalies is the divergent component of the energy transport vector.

Anomalous dry-static energy-flux convergence is found over Europe with minima  $\leq -40 \text{ Wm}^{-2}$  located to the southeast closer to the Mediterranean Sea (Fig. 2.5a). Strong flux-divergence anomalies are found in the North-Atlantic Ocean north of  $\sim 35^\circ \text{ N}$ . The divergent energy-transport vectors show that the energy gained by the atmosphere over the North Atlantic flows into Europe. Along the eastern boundary ( $20^\circ \text{ E}$ ), eastward transport of energy is smaller than usual. A continental source of dry-static energy is centred around the Caucasus ( $\sim 45^\circ \text{ E}$ ,  $43^\circ \text{ N}$ ). Overall, the North-Atlantic Ocean was a source of dry-static energy during SON06, while Europe was a sink.

The North-Atlantic Ocean area, lying between  $50^\circ \text{ W}$  and  $30^\circ \text{ W}$ , acted as a source of latent energy during SON06. This is contrary to earlier speculations that the warmer ocean surface close to the African coast (Fig. 2.4a) provided the excess moist-static energy for the atmosphere over Europe (GJv007). As indicated by the divergent latent-energy-transport vectors, the energy sink is located along the eastern Atlantic region extending into the United Kingdom and its neighbouring sea areas. Latent-energy-transport diverges in the southeastern parts close to the Adriatic Sea (Fig. 2.5b). This latent-energy-divergence exceeding  $20 \text{ Wm}^{-2}$  in this region is associated with a local drying. Drier air (and clear skies) over this region is associated with increased long-wave radiative cooling (not shown), which offsets the gain by dry-static-energy convergence. Within Europe, the divergence maxima found in the southeast are almost completely canceled by the convergence in the west and north, leading to only a small ( $\sim 0.31 \text{ Wm}^{-2}$ ) area-average latent-energy divergence.

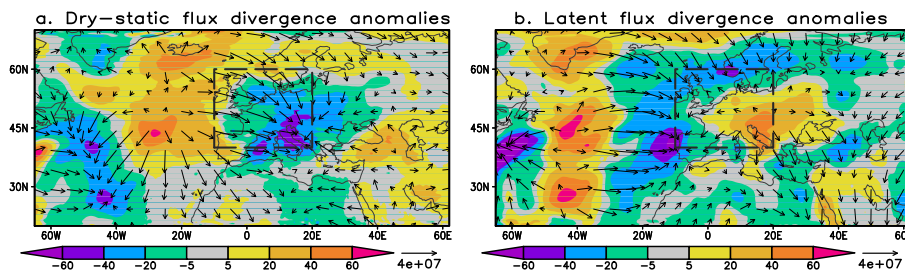


Fig. 2.5: SON06 a) dry-static energy and b) latent energy-divergence anomalies ( $\text{Wm}^{-2}$ ). Positive (negative) shading correspond to areas of anomalous energy-flux divergence (convergence). The divergent component of energy-transport vectors are shown (Units:  $\text{Wm}^{-1}$ ). The area enclosed by the dashed rectangle is that defined in Fig. 2.1.



In SON06, net lateral energy influx acted as a precursor to temperature anomalies: The anti-correlations between total energy-transport divergence and temperature time-series, with the near-surface (vertically-averaged) temperature lagging behind, are 0.24 (0.21), 0.50 (0.57), 0.54 (0.54) and 0.42 (0.47) at lag zero, one, two, and three days, respectively. Hence, convergence (divergence) of energy transport leads to a temperature rise (fall), with a lag of one to three days. Moreover, energy-transport divergence induces radiative responses such as anomalies of downwelling long-wave radiation, which correlate strongly with those of near-surface temperature (Fig. 2.6b). Thus the authors conclude that, averaged over the box, there was a large anomalous flux from the atmosphere to the surface.

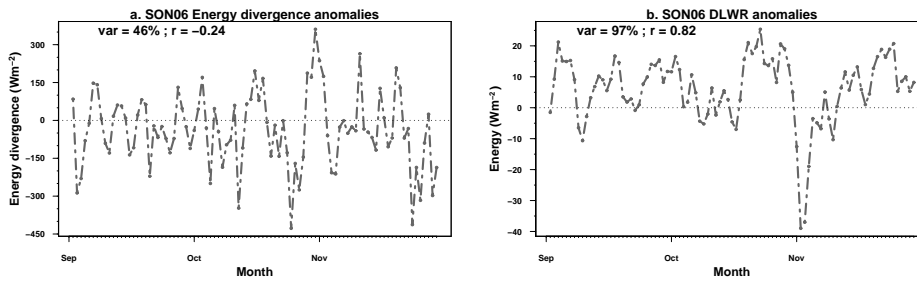


Fig. 2.6: SON06 anomalies of a) energy-transport divergence and b) downwelling long-wave radiation at the surface. Units are  $\text{Wm}^{-2}$ . The annual cycle of energy-transport convergence (downwelling long-wave radiation) captures  $\sim 46\%$  ( $\sim 97\%$ ) of the total variance and the correlation with near-surface temperature anomalies is  $-0.24$  ( $0.82$ ). These numbers are displayed in the plots.

### Turbulent surface fluxes

Anomalous latent heat release into the atmosphere exceeding  $10 \text{ Wm}^{-2}$  is found upstream of the study area in the central North-Atlantic Ocean (Fig. 2.7a). Noteworthy, the region of highest evaporation anomalies roughly correspond to the pattern of the latent energy-divergence shown in Fig. 2.5b. Surface latent-heat flux is dependent on the wind speed ( $|\mathbf{v}|$ ) and the vertical gradient of specific humidity ( $\Delta q/\Delta z$ ) between the earth's surface and the overlying air (*i.e.*  $\text{LH} \propto |\mathbf{v}|\Delta q/\Delta z$ ). The anomalies are hence related to a combination of warmer SSTs and stronger low-level (10 m) wind speeds (Fig. 2.4). In the mid-latitudes, the predominantly zonal (westerly) flow became more northerly (Fig. 2.4b), thus advecting dry high-latitude air further enhancing evaporation over the central Atlantic. A combination of anomalously high specific humidity near the surface and anomalously

weak winds result in less evaporation off the north African coast. A quick glance at Fig. 2.4a may suggest that the warm SSTs off the north African coast provided a source of upstream moist-static energy. Figure 2.7 provide compelling evidence that this was not the case. Negative specific humidity gradient anomalies near the surface (not shown but can be inferred from Fig. 2.10a) result in weak evaporation despite the stronger winds and warmer SSTs close to the European coast. The small positive anomalies of surface latent heat flux ( $\leq 5\text{Wm}^{-2}$ ) found in continental Europe (Fig. 2.7a) are cancelled by the stronger anomalies over the ocean area leading to a negative area-averaged anomaly as presented in Fig. 2.2.

The anomalously weak turbulent flux of sensible heat found in Europe and over the eastern Atlantic boundary (Fig. 2.7b) is consistent with a simple flux–gradient relationship (*i.e.*  $\text{SH} \propto |\mathbf{v}|\Delta T/\Delta z$ ). Even though the eastern Atlantic boundary was anomalously warm (cf. Fig. 2.4a), the air-sea temperature differences ( $\Delta T/\Delta z$ ) were anomalously low (not shown). Using a similar argument (flux–gradient relationship), it is not surprising that anomalous upward sensible flux is found in the central North-Atlantic ocean. In this area, which acted as the major source of energy for the atmosphere during SON06, a northerly anomaly of the low-level flow advected cold air over the warmer ocean.

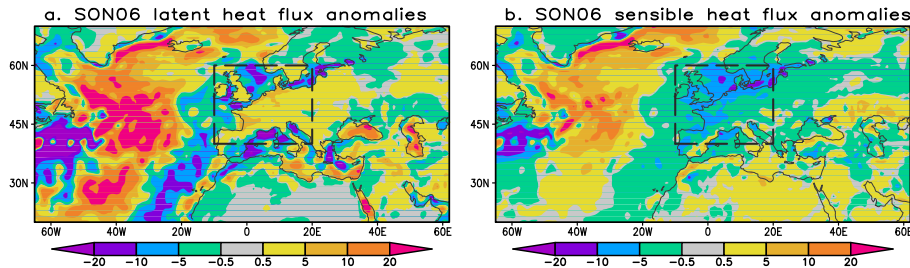


Fig. 2.7: SON06 surface a) latent and b) sensible turbulent heat flux anomalies ( $\text{Wm}^{-2}$ ). The area enclosed by the dashed rectangle is as defined in Fig. 2.1.

Upward transfer of latent heat is anomalously low during the first two months of SON06 (Fig. 2.8a). The first week of November was characterised by anomalously high latent heat release ( $\text{max} \geq 60\text{Wm}^{-2}$ ), which partly compensated for the energy deficit in the atmosphere associated with the energy-transport divergence (cf. Fig. 2.6a). SON06 latent heat release is highly anti-correlated with near-surface temperature. Sensible heat flux from the surface is likewise anomalously low for much of the season except early in November—the air heated the surface during most of SON06 (see Table 2.1 and Fig. 2.2). It appears that the surface turbulent-flux anomalies are a consequence of the atmospheric thermodynamical state: they are part of a surface response rather than a key driver of the SON06

extreme event.

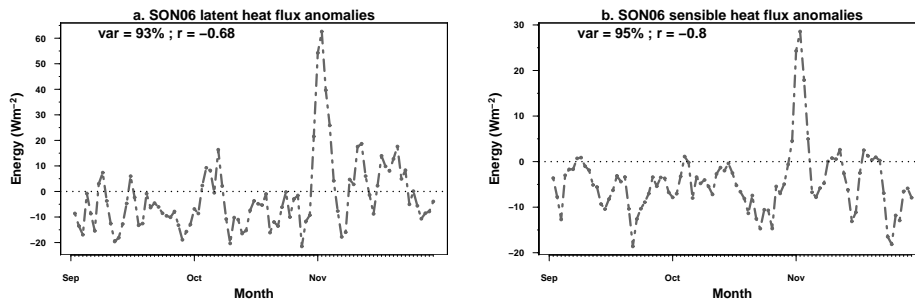


Fig. 2.8: SON06 anomalies of a) surface latent heat flux and b) surface sensible heat flux. Units are  $\text{Wm}^{-2}$ . The anomalies are computed by subtracting the first harmonic of the annual cycle, which captures the inserted percentage of the variance (i.e. 93% and 95% for latent and sensible heat flux, respectively). The correlation ( $r$ ) between each time series with near-surface temperature (black line in Fig. 2.3b) is also inserted in each panel.

#### *Atmospheric net long-wave radiative feedback*

Surface upward long-wave radiation (SuLWR) anomalies are displayed in Fig. 2.9a. Consistent with Stefan Boltzmann's law, the maxima of SuLWR occur over the area of highest near-surface temperature anomalies (cf. Fig. 2.1). However, the increases in the back-radiation from the atmosphere to the surface are larger, leading to the net negative correlation with the temperature shown in Table 2.1.

The bulk of the SuLWR was intercepted by the atmosphere and re-radiated back to the surface as shown in Fig. 2.9b. The similarity in the areal extent and structure of the AnLWRF anomalies with those of the near-surface temperatures is striking. This suggests that the AnLWRF played a vital role in enhancing the SON06 temperature to the extreme values found in Europe.

Figure 2.10a shows that the atmospheric column contained anomalously high amounts of precipitable water during SON06 in the area extending from the eastern Atlantic Ocean across Europe. This figure provides the reason why the AnLWRF was anomalously strong. Only precipitable water anomalies are shown here because, in the absence of clouds (Fig. 2.10b), water vapour is the most significant atmospheric greenhouse gas, contributing about 60% to the natural greenhouse effect (Kiehl and Trenberth, 1997). Although an upward trend in Autumn  $\text{CO}_2$  concentration in response to a decline in carbon uptake by northern ecosystems has been found (Piao et al., 2008), water vapour exhibits the highest interannual

variance of all greenhouse gases. Therefore, it follows from Fig. 2.10a, that the enhanced SON06 greenhouse effect was a direct response to abundant water vapour within the atmosphere. The similarity with the spatial extent and structure of horizontal moisture- (or latent heat-) transport convergence presented in Fig. 2.5b provides some insight into the source of the high amounts of water vapour found here. The higher temperatures increased the water holding capacity of the air, preventing the water-vapour loss by condensation and precipitation.

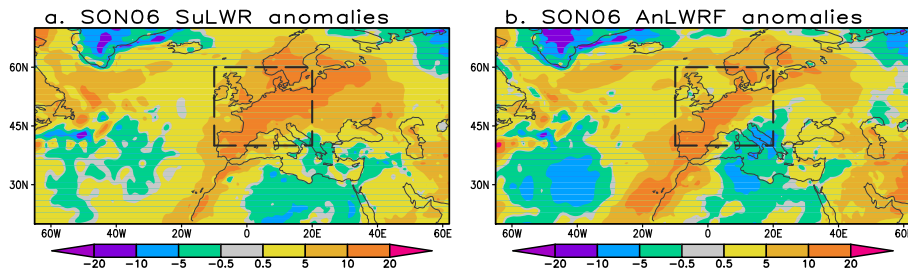


Fig. 2.9: SON06 a) surface upward long-wave radiation (SuLWR) and b) atmospheric net long-wave radiative forcing (AnLWRF;  $\text{Wm}^{-2}$ ). The area enclosed by the dashed rectangle is that defined in Fig. 2.1.

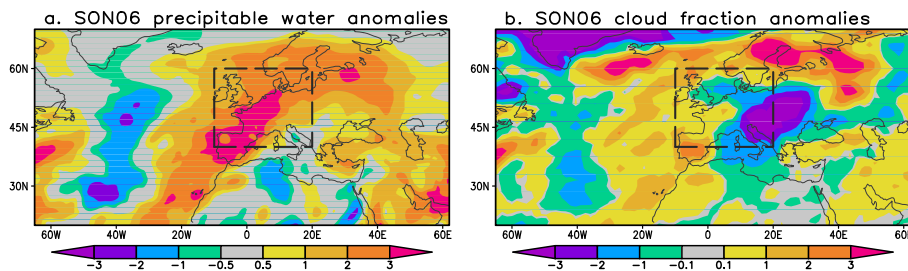


Fig. 2.10: SON06 a) total column precipitable water ( $\text{kgm}^{-2}$ ) and b) cloud fraction anomalies (%). The area enclosed by the dashed rectangle is that defined in Fig. 2.1.

The time series of SuLWR and AnLWRF are shown in Fig. 2.11. As expected, of these two, SuLWR anomalies have the strongest temporal correlation with those of near-surface-air temperature (Fig. 2.11a). Figure 2.11b indicates that the atmosphere over Europe was anomalously opaque to outgoing infrared radiation during much of SON06.

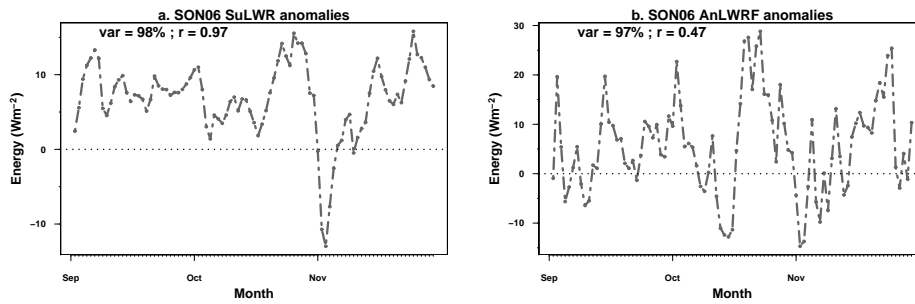


Fig. 2.11: Same as Fig. 2.8 but for a) SuLWR and b) AnLWRF.

#### 2.5.4 Cloud radiative effect

Clouds have two effects. Firstly, clouds absorb and emit infrared radiation. The back-radiation from clouds warms the earth's surface. Cloud greenhouse effect, also referred to as cloud warming effect here, is estimated from the difference between clear- and cloudy-sky net thermal radiation at TOA. Secondly, clouds increase the planetary albedo and thus cool the earth's surface. This cloud cooling effect is here estimated as the difference between net surface solar radiation for cloudy- and clear-sky conditions.

The long-wave effects of clouds were large-than-usual in the second half of October and in November, when above-normal cloud cover caused some warming near the surface (Fig. 2.12a). However, the net effect is very modest, at  $0.9 \pm 0.1 \text{ Wm}^{-2}$ . The cloud cooling (i.e. short-wave) effects were smallest in early September (Fig. 2.12b), when sunny conditions prevailed. This was compensated by the cooling effect of above-average cloud cover later in the season. Averaged over the whole season, the cloud cooling anomaly is even weaker ( $0.2 \pm 1.0 \text{ Wm}^{-2}$ ). Noteworthy, the time series of these two opposing effects are generally out of phase (c.f. Figs. 2.12a,b). On the time mean, the two opposing cloud effects on short-wave and long-wave radiation almost cancel each other out.

An increase of cloudiness accounted for roughly 50% of the AnLWRF anomaly, which is evident from a comparison of Figs. 2.11b and 2.12a. The net effect of clouds is however small due to the compensating effects of changes in short- and long-wave radiation.

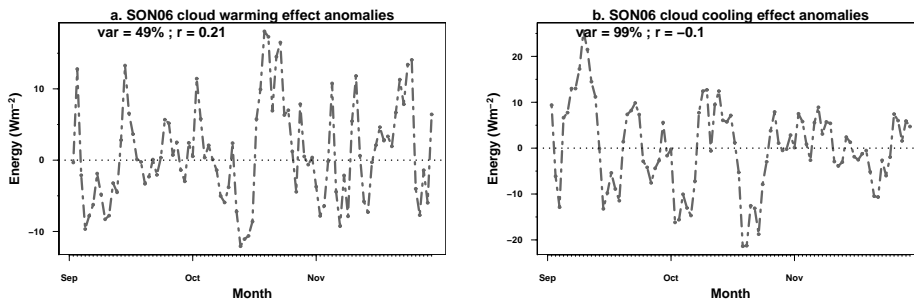


Fig. 2.12: Same as Fig. 2.8 but for a) cloud warming effect, and b) cloud cooling effect ( $\text{Wm}^{-2}$ ).

## 2.6 Discussion and conclusions

This study is an extension to that of GJvO07 who used a simple linear model to show that circulation anomalies accounted for about half of the extreme SON06 temperature anomalies. While it is true that advection of warm tropical air or warm maritime air plays a crucial role, it is also necessary to take into account other competing or reinforcing factors. The aim of this paper is to give a more comprehensive analysis based on reanalysis data in an endeavour to diagnose the factors underlying the SON06 event.

Global warming has become a topical issue in recent years. GJvO07 shows that global warming explains part of the SON06 surface-temperature anomalies while a large part is unaccounted for by this long-term change. The slow increase of global temperature has been attributed to an anthropogenic increase in atmospheric greenhouse gases (IPCC, 2007). At a regional spatial scale and at a seasonal time scale, it has been shown here that the total atmospheric greenhouse effect (referred to here as AnLWRF) contributed strongly to the anomaly. In combination with favourable atmospheric thermodynamics it forced the extreme SON06 in Europe. The results show that latent heat and short-wave radiation fluxes, which were at first suspected to play a major role (GJvO07), did not contribute significantly to the anomaly. The heat was mainly advected as dry-static energy from the North-Atlantic Ocean. The anomaly was strongly enhanced by the water-vapour feedback.

Anomalous divergence of dry-static energy over the North-Atlantic Ocean and a westerly transport vector suggests that this is a major source of energy input into the European atmosphere during SON06. Diabatic heating over the Atlantic Ocean is further enhanced by conversion of latent energy into dry-static energy over the eastern North Atlantic. This excess of energy was transported the mid-latitude

atmospheric flow into Europe where convergence of dry-static energy is found. Maximum dry-static energy convergence occurred in the south-east of the domain. Over the same area, anomalous divergence of latent energy is found. The weaker correspondence in space between the maxima of anomalous dry-static energy convergence and temperature suggests that other physical mechanisms were in play. This notion is in qualitative agreement with Yiou et al. (2007).

A local feedback loop involving infrared radiative forcing has been revealed. A positive anomaly of precipitable water, which increased the atmospheric opacity to outgoing infrared radiation, is found. This induced a positive anomaly in atmospheric back radiation, which warmed the earth's surface. The anomalous warming at the surface results in higher outgoing terrestrial infrared radiation, which is partly absorbed by the atmosphere, hereby increasing the air temperature. The warmer atmosphere has a higher water-vapour holding capacity. This, in turn, create favourable conditions for more precipitable water. This water-vapour feedback has been found to play an important role in climate change (Soden and Held, 2006; Hallegatte et al., 2006). The main conclusion from this study is that this mechanism also played a vital role in forcing the SON06 extreme event. Atmospheric circulation sustained the water-vapour feedback by advecting heat into Europe. The negative anomaly in cloud fraction over land implied lower precipitation, which in turn led to a longer residence time of atmospheric water vapour due to higher temperatures. The relative humidity was close to normal.

Local exchange of sensible and latent heat between the earth's surface and the atmosphere through boundary-layer processes can contribute to a warm anomaly such as SON06. Intuitively, heat flux into the atmosphere causes warming within and immediately downwind of the source of diabatic heating (after condensation in the case of latent energy). However, surface fluxes are sensitive to conditions prevailing in the overlying air. Of the necessary conditions, the air-sea (or air-land) vertical gradients of either temperature or water vapour are of primary importance in determining their relative contributions to the atmospheric energy budget. It has been shown here that in response to weak vertical temperature gradients, the upward sensible heat flux is suppressed over Europe and the eastern Atlantic Coast where the ocean surface is anomalously warm. The findings that diabatic heating of the atmosphere, induced by warm SST anomalies within the domain is weak seem to contradict those of Cattiaux et al. (2009), who argue that warmer SSTs were responsible for  $\sim 30\%$  of the SON06 European surface temperature anomalies. A more detailed explanation of these seemingly contradictory results, which is outside the scope of this paper, would certainly be desirable. Weak positive anomalies of latent-heat flux have been found in Europe. Over these areas, latent heat release by condensation was however anomalously low. Since the surface turbulent fluxes are small, the authors conclude that local feedback processes in-

volving atmospheric vertical mass redistribution such as convection and turbulent mixing mainly respond to the atmospheric thermodynamic state rather than being a fundamental cause of the SON06 extreme event.

GJvO07 shows that climate models used in the IPCC fourth assessment report (AR4) do not show a clear increase in the frequency of the SON06 kind of extremes in the future climate. These models have reliable water-vapour feedbacks. The absence of a clear trend in the frequency of autumn extremes certainly deserves research attention.



### 3. PREDICTABILITY OF COLD SPRING SEASONS IN EUROPE

The seasonal predictability of cold spring seasons (March-May) in Europe from hindcasts/forecasts of three operational coupled general circulation models (CGCMs) is investigated. The models used in the investigation are the Met Office Global Seasonal Forecast System (GloSea), the ECMWF System-2 (S2), and the NCEP Climate Forecast System (CFS). Using the relative operating characteristic score and the Brier skill score the long-term prediction skill for spring 2-m temperature in the lower quintile (20%) is assessed. Over much of central and eastern Europe the predictive skill is found to be high. The skill of the Met Office GloSea and ECMWF S2 models significantly surpasses that of damped persistence over much of Europe but the NCEP CFS model outperforms this reference forecast only over a small area. The higher potential predictability of cold spring seasons in eastern Europe relative to southwestern Europe can be attributed to snow effects as areas of high skill closely correspond with the climatological snow line, and snow is shown in this paper to be linked to cold spring 2-m temperatures in eastern Europe. The ability of the models to represent snow cover during the melt season is also investigated. The Met Office GloSea and the ECMWF S2 models are able to accurately mimic the observed pattern of monthly snow-cover interannual variability, but the NCEP CFS model predicts too short a snow season. Improvements in the snow analysis and land surface parameterizations could increase the skill of seasonal forecasts for cold spring temperatures.

#### 3.1 Introduction

The seasonal prediction of near-surface temperatures over many parts of the globe has received considerable attention. In fact, together with precipitation, seasonal prediction of 2-m temperature has a wide application. Considerable effort has gone into predictions of mean temperatures over many parts of the globe including Europe (e.g. Barnston and Smith, 1996). However, it is extreme temperatures

---

This chapter is based on the article "Predictability of Cold Spring Seasons in Europe" by Mxolisi E. Shongwe, Christopher A. T. Ferro, Caio A. S. Coelho, and Geert Jan van Oldenborgh, 2007, published in *Monthly Weather Review*, **135**, 4185–4201.

such as heat waves and cold outbreaks that have a larger effect on human society. Despite the worldwide notion of global warming and its impacts, the absence of a clear trend toward fewer extreme cold events in Europe (Klein Tank et al., 2002) has prompted an investigation of their potential predictability in this study. These extreme events typically occur in winter and spring possibly due to snow effects, and have huge impacts on transportation systems, energy supply, ecology, agriculture, winter tourism, the clothing industry, etc.

The predictable component of atmospheric variability at seasonal to interannual time scales is that forced by changes in boundary conditions (e.g. Barnston et al., 2005). Walsh et al. (2001) related extreme winter and spring cold outbreaks to negative North Atlantic Oscillation (NAO) signatures consistent with a "blocking" of westerly airflow into Europe. However, at smaller spatial scales the influence of large-scale circulation anomalies such as those related to SST variability is modulated by interactions and feedbacks between the atmosphere and the land surface. Among other land surface processes, observational and modeling studies have revealed that snow impacts near-surface temperature variability in the Northern Hemisphere extra-tropics during the cold season (Walsh et al., 1982, 1985; Yang et al., 2001; Kumar and Yang, 2003).

In Europe near-surface temperature variability has been attributed to three main factors: large-scale flow, which determines the origin and tracks of air masses (e.g. van Oldenborgh and van Ulden, 2003), radiation balance (as determined by cloudiness amongst other factors; Lenderink et al., 2006), and local lower boundary conditions (Ferranti and Viterbo, 2006). Palmer et al. (2004) have shown that seasonal predictability of large-scale flow in Europe is low. The effect of cloudiness offers some limited predictability. Skill from SST persistence has been shown to be confined mainly along coastal areas (van den Dool and Nap, 1985).

This paper aims to investigate the predictability of cold spring seasons in Europe. We investigate the hypothesis of snow accumulated during the preceding winter being a source of skill in predicting cold spring seasons in Europe. Snow increases the surface albedo, thereby altering the terrestrial heat balance and providing a positive feedback mechanism that modulates atmospheric variability. In the first part of the paper, we assess the coupled general circulation models (CGCMs) below-median, lower-, and upper-quintile (i.e., coldest and warmest 20% of the climatological records) 2-m temperature seasonal predictive skill over Europe in spring [March-May (MAM)]. Near-surface temperature forecasts obtained from damped persistence of low temperatures from the previous winter and early February snow depth are used as a baseline to judge the performance of the CGCMs. We then relate the 2-m temperature to snow water equivalent (SWE) and snow cover to explain the physical basis of the model skill.

## 3.2 Data and Methods

### 3.2.1 CGCM predictions

The CGCMs used in this study are the Met Office Global Seasonal Forecast System (GloSea), the European Centre for Medium-Range Weather Forecasts System-2 (ECMWF S2), and the National Centers for Environmental Prediction Climate Forecast System (NCEP CFS). For more details on these models see Table 3.1. The model data are accessible through the Royal Netherlands Meteorological Institute (KNMI) Climate Explorer (*see online at [climexp.knmi.nl](http://climexp.knmi.nl)*; van Oldenborgh and Burgers, 2005). The ECMWF S2 consists of five members in each ensemble for the hindcast period (1987-2001) and 40 members thereafter. Only five members in the forecast period have been used to match the hindcast period. The NCEP CFS and GloSea models have 15 ensemble members each in hindcast mode, which are used in this study. However, since 2004, the NCEP CFS model produces twice-daily operational forecasts resulting in about 60 ensemble members. GloSea produces 40 ensemble members for the operational forecasts since 2004. The February-start hindcasts/forecasts have been verified against MAM 2-m temperature, implying a 1-month lead time (but half-month from dissemination time, usually the 15th of each month). An extreme event is defined whenever 2-m temperatures fall within the lower quintile of the climatological records, otherwise it is a nonevent. Events were defined for model predictions and observations independently (i.e., based on their own model predictions and observed distributions). When using this approach model biases are inherently corrected. Model ensemble predictions are converted into probabilistic forecasts by expressing, as a percentage, the fraction of the ensemble predicting the extreme event. For instance if 9 members out of 15 are fall into the lowest quintile, and the rest fall outside this category, then the probability for the event occurring (not occurring) is 60% (40%).

### 3.2.2 Observations

The snow-depth data (expressed as SWE) used in this study are a combination of data from the 40-yr ECMWF Re-Analysis (ERA-40) project (Uppala et al., 2005) up to 2002, and the ECMWF snow analysis (White, 2003) from 2003 to present. Weekly snow-cover data spanning the 1972-2006 period, obtained from National Oceanic and Atmospheric Administration/National Environmental Satellite Data and Information Service (NOAA/NESDIS) datasets (Robinson et al., 1993), are also used. The weekly snow cover has been averaged into monthly data. To compare these two datasets, snow extent has been generated for each grid by assigning a one if the ECMWF SWE on a given day is at least 3 mm, and 0 otherwise. The 3-mm SWE threshold yielded the best agreement with the NOAA/NESDIS

dataset. Monthly averages are generated based on these derived variables. Given that the effect of the extent of snow cover on 2-m temperature is felt during and after its existence (e.g. Groisman et al., 1994) and because the atmosphere adjusts rapidly in response to anomalous land surface forcing, only short (1 month) lead-lag relationships are considered whereby February-April (FMA) mean snow is related to MAM mean 2-m temperature. The 2-m temperature data have been obtained from the recently developed high-resolution ( $0.5^\circ \times 0.5^\circ$  latitude-longitude grid) gridded monthly dataset of Fan and van den Dool (2008), which combines the Global Historical Climatology Network (GHCN), version 2, and the Climate Anomaly Monitoring System (CAMS) datasets.

Pointwise correlations between FMA NOAA/NESDIS and ERA-40-derived FMA mean snow cover calculated over the period 1972-2005 are shown in Fig. 3.1. Statistical significance at the 5% (1%) level (as obtained from a one-sided two-sample *t*-test with 32 degrees of freedom) corresponds to a correlation coefficient of 0.34 (0.44). The high correspondence between the two datasets is evident over a wide area extending eastward from  $10^\circ$  E. Areas with zero standard deviation during FMA (e.g., northern Scandinavia and Africa in or close to the Sahara Desert) are masked out in the plot. Biases in remotely sensed data such as NOAA/NESDIS satellite data exist (Robinson et al., 1993; Foster et al., 1996). The ERA-40 snow-depth analysis assimilates some observations, otherwise it relies completely on the model snow precipitation and melt parameterizations, which are known to have biases. These limitations notwithstanding, the high correlation between the remotely sensed and reanalysis data over Europe is encouraging. Because it is quite unlikely that both datasets would have the same biases, both snow datasets should be reliable enough for our purposes.

### 3.2.3 Forecast verification

Skill measures used to assess the CGCMs probabilistic temperature forecasts are the relative operating characteristic (ROC) score and the Brier skill score (BSS). These metrics and other forecast verification measures are computed by the KNMI Climate Explorer using statistical software developed by the R Software for Climate Analysis (RCLIM) initiative (see online at <http://www1.secam.ex.ac.uk/?nav=696>). The ROC score measures the ability of the forecast system to correctly detect events or non-events. The reference ROC score of 0.5 implies no skill in the forecasts, and the score increases to a maximum of 1.0 for perfect forecasts. Scores less than 0.5 are indicative of negative skill (i.e., worse than chance). The numerical formulation and comprehensive discussion of the ROC score can be found in Mason and Graham (1999, 2002). For a set of  $n$  forecasts, if  $n_1(n_2)$  is the number of cases in which the event occurs (does not occur), Mason and Graham (2002) define the ROC score for probabilistic forecasts from an ensemble of size  $m$  as

Tab. 3.1: Coupled GCMs used in this study<sup>a</sup>

Model	Atmospheric Resolution	Initialization	Hindcasts from, #/mon	Forecasts from, #/mon	References
ECMWF S2	T95L40	ERA15	1987 5	2001 40	Anderson et al. (2003) van Oldenborgh et al. (2005a,b)
NCEP CFS	T62L64	NCEP	1981 15	2004 60	Saha et al. (2006)
UKMO GloSea	3.75° × 2.5° L19	ERA40	1987 15	2004 40	Graham et al. (2005)

<sup>a</sup>Model resolution is given as T (wavenumber of spectral truncation) and L (number of vertical layers). The UKMO GloSea model horizontal resolution is given as lon x lat grid.

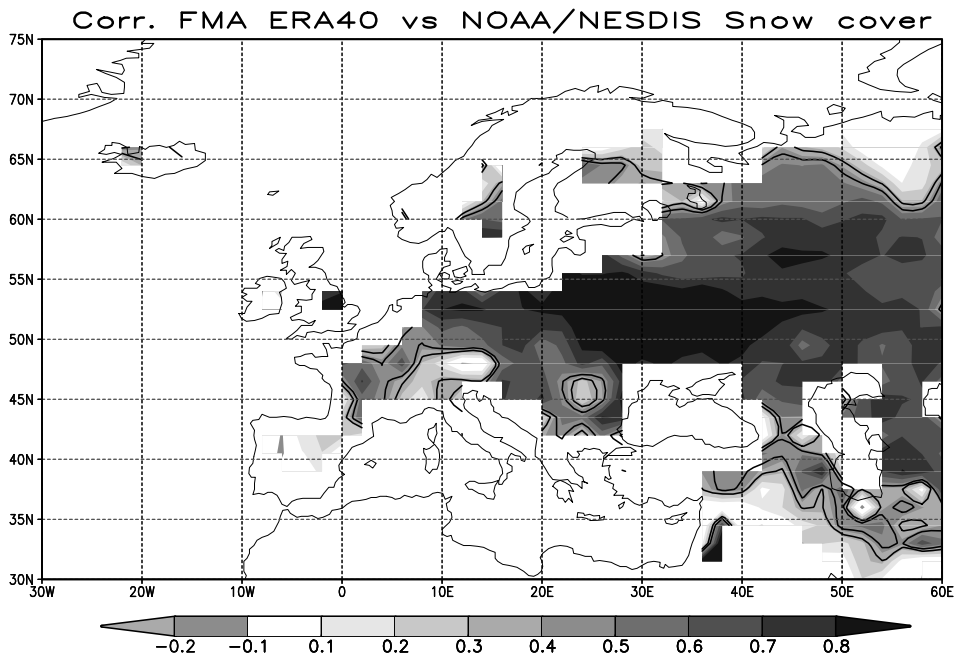


*Fig. 3.1:* Correlation plot between FMA NOAA/NESDIS and ERA40-derived snow cover. A correlation of 0.34 (0.44) is found to be statistically significant at the 5% (1%) level, and the corresponding contours are plotted.

$$A_{m,n} = 1 - \frac{1}{n_1 n_2} \sum_{\substack{1 \leq i \leq n_1 \\ 1 \leq j \leq n_2}} I(P_{1i} < P_{2j}) - \frac{1}{2n_1 n_2} \sum_{\substack{1 \leq i \leq n_1 \\ 1 \leq j \leq n_2}} I(P_{1i} = P_{2j}), \quad (3.1)$$

where  $P_{1i}(P_{2j})$  are the forecasts issued prior to an event (nonevent), and  $I(B) = 1$  if condition B holds, 0 otherwise. Suppose a subset  $K_{1i}(K_{2j})$  of the ensemble predict the event (nonevent). Given an ensemble of size  $m$ , C. A. T. Ferro (2007, unpublished manuscript) has shown that an unbiased estimator for the expected ROC score that would be obtained by an ensemble of size  $M \leq m$  is

$$\begin{aligned} \hat{A}_{M,n} = 1 - \frac{1}{n_1 n_2} \sum_{\substack{1 \leq i \leq n_1 \\ 1 \leq j \leq n_2}} \left\{ \sum_{(k,l) \in L_{ij}} \binom{K_{1i}}{l} \binom{m - K_{1i}}{M - l} \binom{K_{2j}}{k} \binom{m - K_{2j}}{M - k} \right. \\ \left. + \frac{1}{2} \sum_{k \in \kappa_{ij}} \binom{K_{1i}}{k} \binom{m - K_{1i}}{M - k} \binom{K_{2j}}{k} \binom{m - K_{2j}}{M - k} \right\} / \binom{m}{M}^2 \quad (3.2) \end{aligned}$$

where  $L_{ij}$  is the subset of  $\{(k, l) : 0 \leq l < k \leq M\}$ , such that the combinations in the first summation exist, and  $\kappa_{ij}$  is the subset of  $\{0, \dots, M\}$  such that the combinations in the second summation exist.

Aware of the effect of ensemble size on ROC scores across the three CGCMs used in this research, the expected ROC scores have been estimated for each model for 50% (for below-median 2-m temperature predictions) and 20% (lower quintile) thresholds using  $M = 5$  corresponding to the ECMWF S2 ensemble size before 2002 (see Table 3.1). This gives us confidence that the intermodel-ROC-score differences shown below reflect true CGGMs' individual strengths and weaknesses. Critical values are calculated from a normal approximation to the distribution of the ROC score under a null hypothesis of random forecasts, with issued probabilities distributed uniformly on  $M + 1$  distinct values. Differences in the ROC scores have been computed and their statistical significance tested using the method discussed by C. A. T. Ferro (2007, unpublished manuscript).

The relative improvement of numerical model predictions of cold seasons over an empirical approach is assessed using Brier skill scores with reference to forecasts from a simple statistical model. The BSS measures the forecast system's improvement over a reference forecast strategy (Wilks, 1995).

The reference empirical model for spring temperature ( $T'_{\text{MAM}}$ ) is a linear model based on three predictors: global warming, temperature persistence from winter into spring ( $T'_{\text{NDJ}}$ ), and snow depth at analysis time ( $H_{1\text{Feb}}$ ):

$$T'_{\text{MAM}}(y) = \alpha(y)T'_{\text{NDJ}}(y-1) + \beta(y)H_{\text{1Feb}}(y) + \eta(y), \quad (3.3)$$

$$T'_s(y) = T_s(y) - \frac{1}{10} \sum_{y'=y-11}^{y-1} T_s(y'), \quad (3.4)$$

with  $y$  the year being forecast. Global warming is taken into account as a running mean of the local observed temperature 10 yr prior to the forecast time as shown in Eq. 3.4 for a given season. In many areas this "optimal normal correction" gives most skill to seasonal forecasts (Huang et al., 1996). The persistence predictor is the November-January-averaged temperature anomaly relative to this climatology. Temperature persistence from winter into spring is known to be significant in Europe. The third predictor is the ERA-40 snow-depth analysis at analysis time, 1 February. The coefficients  $\alpha(y)$  and  $\beta(y)$  are determined by linear regression of all years except the ones being forecast (jackknife). Winter temperature and snow depth are correlated ( $r \approx 0.5$  in eastern Europe) as a thick snow layer in eastern Europe on 1 February is often produced by a cold winter preceding it. Because of this, statistical forecast models based on persistence only ( $\beta = 0$ ), snow depth only ( $\alpha = 0$ ), and a combination of the two have very similar skill in forecasting the spring temperature.

To compute probabilistic skill scores for the empirical forecast model, an ensemble of forecasts is required. This ensemble, of equal size  $N$  as the CGCM ensemble, is generated by sampling the distribution of the residuals  $\eta(y)$  at the quantiles  $i/(N+1)$ , ( $i = 1 \dots N$ ).

#### 3.2.4 Near-surface temperature – snow relationships

Scatter diagrams are plotted to show relationships between spatial averages of observed FMA mean snow and MAM mean 2-m temperature over the 1972-2005 period. Canonical correlation analysis (CCA) is then used to diagnose the spatial extent of the linear relationship between the two fields. CCA is a multivariate statistical technique that seeks to identify a sequence of pairs of patterns in the data whose time evolution is optimally correlated. This technique has been widely applied in seasonal climate prediction studies (e.g. Landman and Mason, 2001; Shongwe et al., 2006), and its procedure in the context of climate data analysis can be found in Wilks (1995) and von Storch and Zwiers (1999). Prior to the CCA, the spatial degrees of freedom were reduced by projecting original data onto their empirical orthogonal functions (EOFs; Barnett and Preisendorfer, 1987). Performing the CCA on the EOF space minimizes large sampling errors (Bretherton et al., 1992) at the expense of possible losses of useful information in the original data



from EOF truncation. The EOF space is truncated at 70% of the average characteristic root, which is the *Guttman–Kaiser* criterion (Jackson, 1991) modified after Jolliffe (1972). The length of the sequence of successive pairs of canonical variates (CCA modes) is limited to be the minimum of the number of principal components (EOF modes) retained in the EOF analysis. The optimal combination of EOF and CCA modes producing the best fit are then determined from cross-validated sensitivity tests.

### 3.3 Skill of MAM 2-m temperature forecasts

#### 3.3.1 Model ROC scores

Maps of ROC scores calculated for CGCM probabilistic predictions of MAM 2-m temperatures over the region  $30^{\circ}$ – $75^{\circ}$  N,  $30^{\circ}$  W– $60^{\circ}$  E are shown in Figs. 3.2–3.3. Figure 3.2 compares the ROC scores for the GloSea model for median (3.2a) and lower-quintile (3.2b) 2-m temperature. Differences between scores for model predictions of cold springs and below-median temperatures (representing normal seasons) are shown in Fig. 3.2c. Areas where the null hypothesis of no difference in ROC scores for the different thresholds (here, 20% and 50%) could be rejected at the 10% error level are shaded in Fig. 3.2c. Corresponding comparisons are made for the ECMWF S2 (Fig. 3.2d–f) and NCEP CFS (Figs. 3.2g–i) systems.

ROC scores in excess of 0.6 for below-median 2-m temperature are confined to the area around the Baltic Sea extending from Poland northward into Scandinavia in GloSea (Fig. 3.2a) and ECMWF S2 (Fig. 3.2d) systems. At the 10% significance level, the critical ROC scores for rejection of the null hypothesis of unskillful forecasts are 0.7 for GloSea and ECMWF S2, and 0.68 for the NCEP CFS models. For below-median forecasts the models' ROC scores are not statistically significant over much of Europe. The NCEP CFS forecasts show little or no skill (Fig. 3.2g). ECMWF S2 and GloSea models show elevated ROC scores ( $> 0.7$ ) for predictions of 2-m temperature in the lowest quintile. This is particularly the case over eastern Europe east of  $10^{\circ}$  E. GloSea and ECMWF S2 attain ROC scores in excess of 0.8 for the cold extremes (Figs. 3.2b,e). Widespread positive differences between scores for the 20% and 50% thresholds are evident over much of Europe except the southwest, although only statistically significant differences are shaded in the figures. Remarkably, for GloSea and ECMWF S2 systems, statistically significant differences at the 10% level are found over a wide area extending from the North Sea through central toward eastern Europe (Figs. 3.2c,f). The CGCMs show either no skill or negative skill over southwestern Europe. Albeit least skillful overall, the NCEP CFS model also can provide skilful forecasts over eastern Scandinavia and western Russia.

The high ROC scores and differences for below-median and lower-quintile 2-m temperature over much of central and eastern Europe warrants an investigation of their physical basis. Interestingly, the lowest-quintile 2-m temperature forecasts are more skillful than those of the upper quintile ( $\geq 80\%$  of the distribution), notably in the ECMWF S2 model (Fig. 3). We hypothesize that elevated ROC scores could be due to a successful representation of snow persisting in spring and influencing near-surface temperatures (Cohen and Rind, 1991). This mechanism naturally gives rise to higher skill for cold extreme forecasts than below-median or upper-quintile 2-m temperature forecasts.

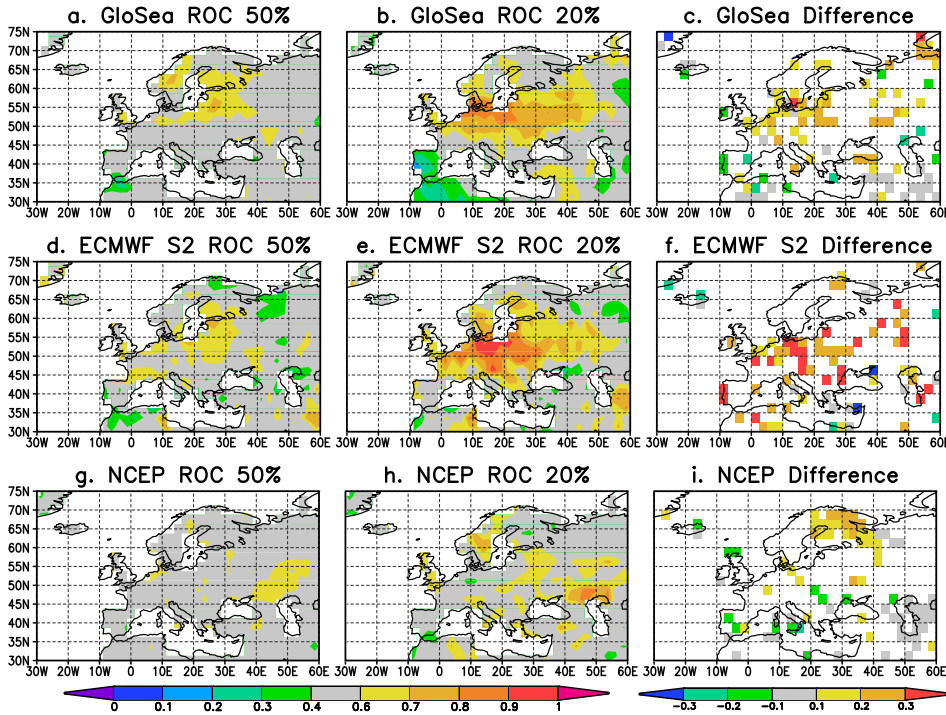


Fig. 3.2: Geographical distribution of ROC scores for GloSea predictions of MAM 2-m temperature. ROC scores are for (a) below-median and (b) lower-quintile 2-m temperature predictions. ROC scores in excess of 0.7 are statistically significant at the 10% level. (c) Differences in the ROC scores (i.e.  $ROC_{20} - ROC_{50}$ ). Areas where the differences are statistically significant at the 10% level are colored. (d), (e), (f) Same as in (a), (b), (c), but for ECMWF S2. (g), (h), (i) Same as in (a), (b), (c), but for NCEP CFS. ROC scores greater than 0.68 are statistically significant at the 10% level.

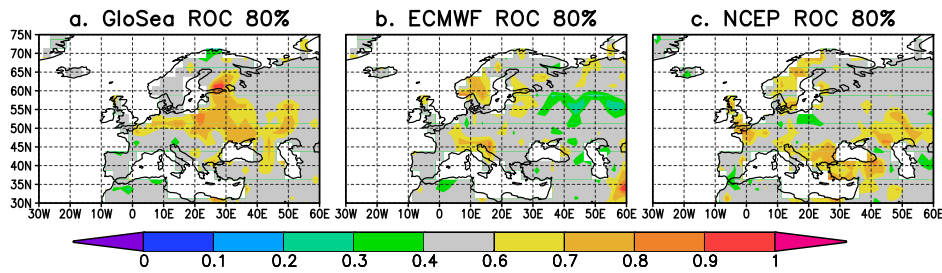


Fig. 3.3: Geographical distribution of ROC scores for CGCMs predictions of MAM 2-m temperatures in the upper quintile: (a) GloSea , (b) ECMWF S2, and (c) NCEP CFS.

### 3.3.2 Model Brier skill scores

The CGCMs advantage over a statistical model assessed using BSS are shown in Fig. 3.4. For below-median 2-m temperature predictions GloSea outcores the statistical model forecasts over much of Europe west of 40° E (Fig. 3.4a). The ECMWF S2 and NCEP models perform slightly better than damped persistence forecasts only over patchy areas in Europe, otherwise the models attain skill equal to or less than that of the reference forecast over a wide area in Europe (Figs. 3.4b,c).

For lower-quintile 2-m temperature forecasts, GloSea and ECMWF S2 models surpass damped persistence over a wide area extending from the North and Baltic Seas through central Europe toward the Mediterranean area. Negative skill scores are confined to a narrow area from about 15°–20° E in GloSea. The BSS provide further evidence that there is more potential for forecasting cold spring seasons than below-median seasons; this is particularly noticeable in the case of ECMWF S2, which attains more widespread positive skill scores in Europe (Fig. 3.4e). However, in southwestern Europe, the models perform worse than damped persistence. The NCEP CFS outperforms the reference forecasts over isolated areas (Fig. 3.4f). At the short lead time considered in this paper, Brier skill scores show that statistical models provide competitive predictions of lower-quintile 2-m temperatures over certain regions (e.g., southwestern Europe and western Russia).

### 3.3.3 Ensemble 2-m temperature predictions in eastern Europe

Bias-corrected ensemble model predictions for March and spring 2-m temperature, spatially averaged over eastern Europe (45°–55° N, 20°–30° E) for the period 1987–2005 (common to all models) are shown in Fig. 3.5. The number of members in each model ensemble are as shown in Table 3.1. The spatial averages are

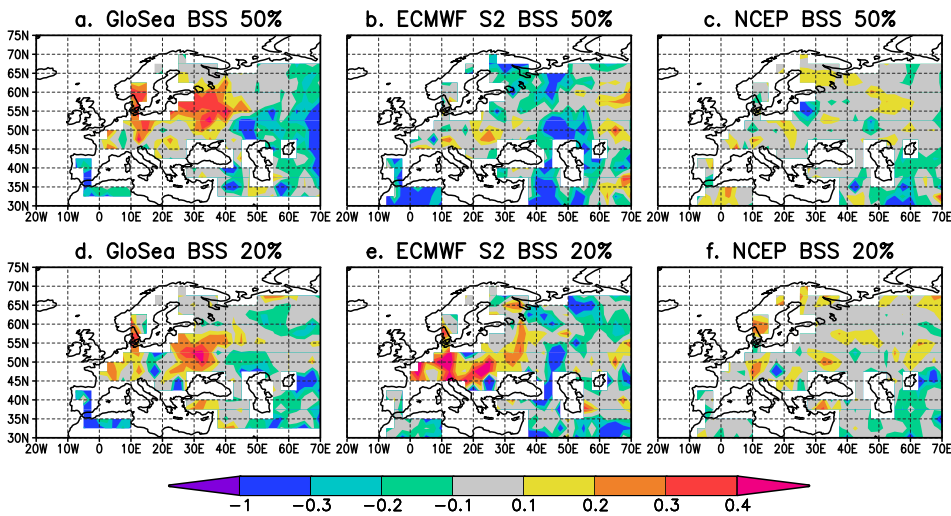


Fig. 3.4: Evaluation of the CGCM MAM 2-m temperature forecasts' BSS with reference to damped persistence. Skill scores for (a), (b), (c) below-median 2-m temperature forecasts and (d), (e), (f) lower-quintile scores. Skill scores are for (a), (d) GloSea; (b), (e) ECMWF S2; and (c), (f) NCEP CFS.

taken over the area characterized by high skill for lowest-quintile 2-m temperature forecasts in spring (as shown in Figs. 3.2 and 3.4). Prior to the area averaging, the CGCM predictions were bias corrected for the mean in a cross-validation mode. Anomalies are defined as departures from the 1971–2000 climatology. Observed 2-m temperature anomalies for the month and season in a given year are denoted by squares. The climatological lower-quintile category is shown by the gray shaded region. SWE anomalies for February, March, and April averaged over the same area are plotted in Fig. 3.6.

In Fig. 3.5b, years characterized by cold spring 2-m temperatures common to all models are 1987, 1996, 2005, and 1997, although in some cases not all 3 months in each season fell in the lowest quintile. Noting that March exhibits the highest skill of all spring months (mainly from snow signal; map not shown), attention is placed on the distribution of the ensemble members during March of each cold spring (leaving out the warmer March 1997; Fig. 3.5a). As shown in Fig. 3.6, a thick snowpack occurred from February to March preceding each coldest event, an exception being 1997.

In the prediction for March 1987, GloSea had 12 ensemble members (80%) falling within the lowest quintile, while 9 NCEP CFS model members (60%) predicted the extreme event. The ECMWF S2 model predicted the event with 40% probability

(two members). In 1996, GloSea had seven of its members (~47%) correctly predicting the event. ECMWF S2 anticipated the event with 40% probability, while the NCEP CFS model indicated about 27% (four members) chance. March 2005 cold event was predicted with 60% probability (nine members) by GloSea, NCEP CFS with about 27% while the ECMWF S2 system indicated only a 5% chance of 2-m temperatures falling within the lowest quintile.

Considering all spring months (MAM), the 1987 cold event was predicted very well by the GloSea and ECMWF S2 systems with each indicating at least 80% probability (12 and 4 members, respectively) of lowest-quintile 2-m temperatures. The NCEP CFS model predicted this event with about 53% probability. The ECMWF S2 system predicted the 1996 cold event with high probability (60%), with GloSea and NCEP CFS models indicating a 47% and 27% likelihood, respectively. The 1997 and 2005 events were least skillfully predicted with all models predicting the 1997 cold spring with 20% probability, equivalent to the lower-quintile prior probability or climatological forecasts. The 2005 event was predicted with low probability of about 33% and 20% by GloSea and NCEP CFS models, respectively, while the ECMWF S2 model almost completely missed (~3% probability) the 2005 cold spring season in eastern Europe. As shown in Fig. 3.6, the 1997 cold event was preceded by negative SWE anomalies from February to March. It is therefore not surprising that this "atypical" event was either underforecast or completely missed by the CGCMs.

### 3.4 Snow influence

Snow-cover variability for FMA expressed as standard deviations of the extent of snow cover on the ground is shown in Fig. 3.7. The figure shows that areas in central and eastern Europe are characterized by the greatest interannual fluctuations of early spring snow cover. The other neighboring regions (e.g., southwest Europe and parts of Scandinavia) have a high frequency of either 0% or 100% snow cover during early spring months. There is a close correspondence in geographical area between the regions where this land surface condition is most variable from year to year, and where ROC scores for cold springs are highest (in GloSea and ECMWF S2 models; Fig. 3.2).

#### 3.4.1 2-m temperature – snow relationships in observations

##### *Snow and near-surface temperature relationships in eastern Europe*

To illustrate the influence of changes in local land surface forcing associated with snow on near-surface temperature, spatial averages of SWE, snow cover, and 2-m temperature were calculated for a rectangular area (45°–55° N, 20°–30° E) and

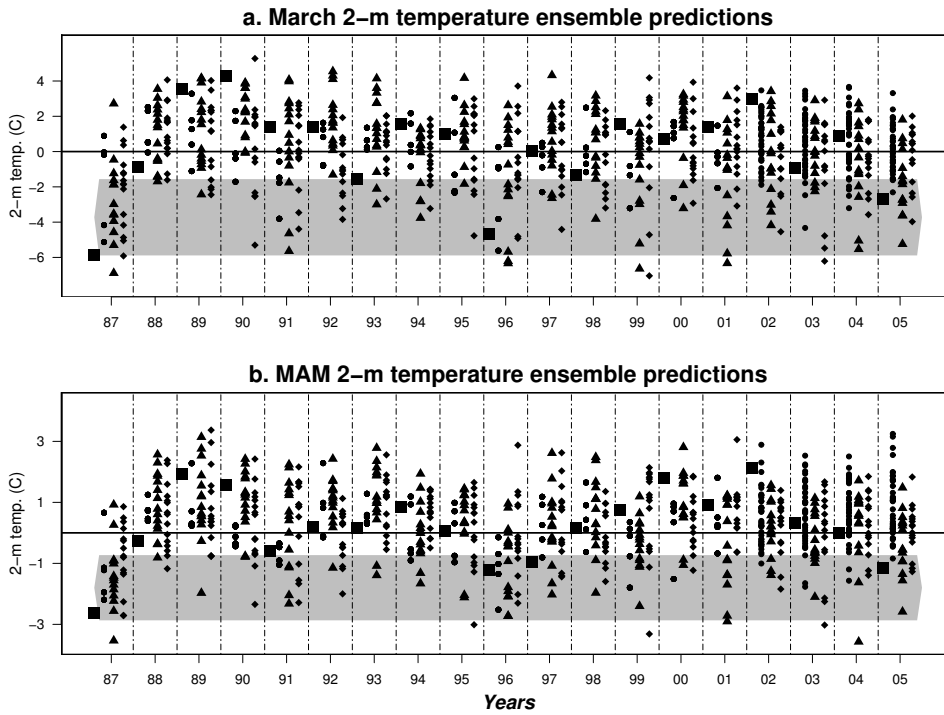


Fig. 3.5: CGCM ensemble predictions for (a) March and (b) spring. In both (a) and (b) and for a given year (left) the squares show the observed anomalies, (middle left) the circles show the ECMWF S2 ensemble predictions, (middle right) the triangles show the GloSea ensemble predictions, and (right) the diamonds show the NCEP CFS ensemble predictions. The observations/predictions have been averaged over eastern Europe ( $45^{\circ}$ – $55^{\circ}$  N,  $20^{\circ}$ – $30^{\circ}$  E). The gray shaded region shows the lower quintile category defined from the 1971–2000 climatology.

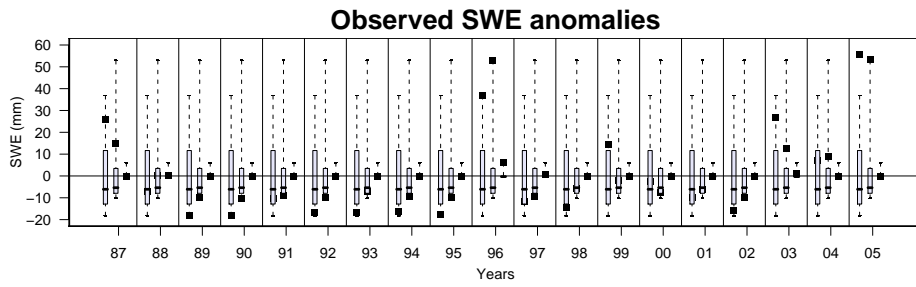


Fig. 3.6: Area-averaged FMA SWE in eastern Europe (same geographical area as in Fig. 3.5). Boxplots show the climatological range based on the 1971-2000 period, while the black squares indicate the observed SWE in a given month. For each year, the first series shows February SWE, the second series shows March, and the third series shows April SWE.

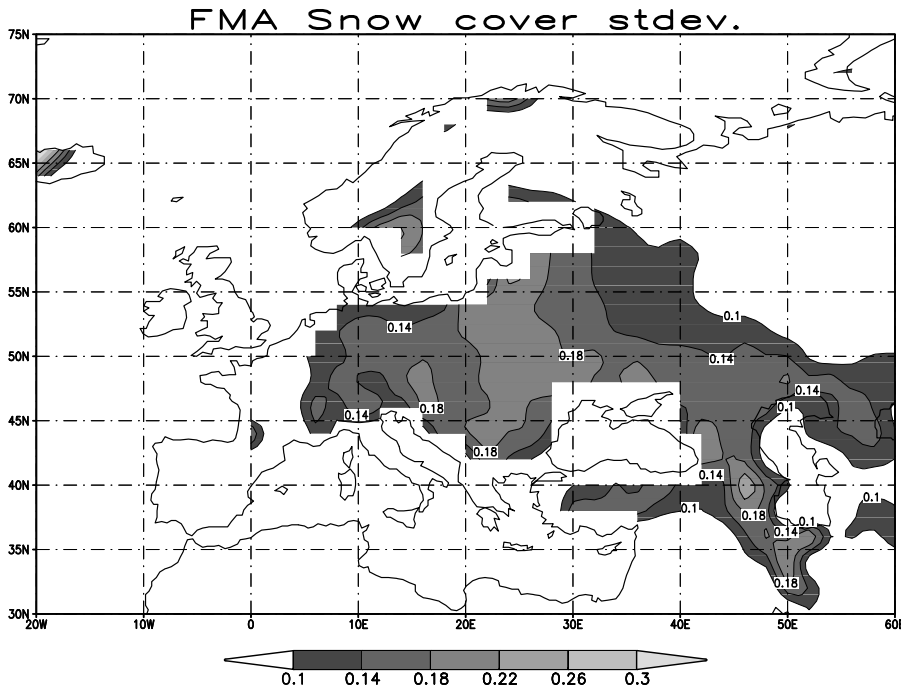


Fig. 3.7: FMA snow-cover variability in Europe expressed as standard deviations of the extent of snow on the ground.

plotted in Fig. 3.8. As shown in Fig. 3.7, the area averages are taken over a region with highest interannual snow-cover variability in FMA and highest skill for cold spring forecasts (Fig. 3.2). In Fig. 3.8a, MAM 2-m temperature is plotted against February SWE. The plot shows that very cold temperatures occurred often following high SWE at the beginning of February, and vice versa for the warm extreme. The correlation is 0.57 (statistical significance at the 1% level). The plot for MAM 2-m temperature against FMA snow-cover extent (Fig. 3.8b) is consistent with the results from SWE (obtained from ERA-40), despite the fact that the snow datasets are obtained from independent sources. The plot shows that the coldest MAMs over eastern Europe have occurred following extensive snow cover from February to April (correlation = -0.63). The plots make physical sense. Snow influences near-surface temperatures through its high reflectivity to incident radiation, low thermal conductivity, which inhibits sensible heat flux from the ground into the overlying air, and by acting as a latent heat sink during the melting process. Even after melting, the resulting soil moisture influence near-surface air temperature through its effect on the surface heat balance in the form of alterations in partition of latent and sensible heat fluxes. These results are in qualitative agreement with Groisman et al. (1994), who classified eastern Europe as a temperature-sensitive zone from December to March. The scatterplot for FMA fractional snow extent against February SWE is presented in Fig. 3.8c. The strong correlation of 0.74 indicates that a thick snowpack on 1 February on average translates into longer lingering snow in spring, despite the well-known observations that a snowpack can be melted in surprisingly short times by, for example, heavy precipitation at high temperatures.

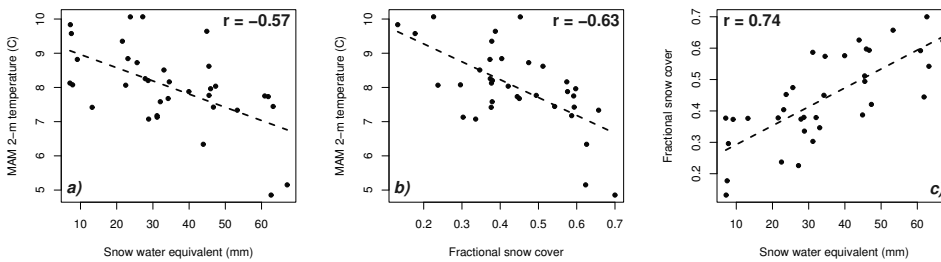


Fig. 3.8: Scatterplots of spatially averaged (i.e., averaged from  $45^{\circ}$ – $55^{\circ}$  N,  $20^{\circ}$ – $30^{\circ}$  E) (a) MAM 2-m temperature ( $^{\circ}$  C) vs 1 February SWE (mm), (b) MAM 2-m temperature ( $^{\circ}$  C) vs FMA fractional snow cover, and (c) FMA fractional snow cover vs 1 February SWE (mm).



*CCA diagnostics*

To the extent that there exists some linear relationship between snow cover and 2-m temperature as suggested by the scatterplots, the use of a linear statistical technique such as CCA to diagnose the spatial patterns of covariability between the two fields is justified. Cross-validated sensitivity tests suggested that a subspace consisting of 11 observed snow-cover EOFs (70% cumulative variance) and six 2-m temperature EOFs (72% cumulative variance) could optimally be used in conjunction with four CCA modes (successive pairs of canonical variates). The spatial patterns for the first canonical mode (whose canonical correlation is highest) and the corresponding time series are shown in Fig. 3.9. In Fig. 3.9a, the first canonical eigenvectors of the snow-cover field leading spring 2-m temperature by 1 month are plotted. The corresponding canonical eigenvectors for spring 2-m temperature are presented in Fig. 3.9b. The magnitude of the loadings (elements of the canonical eigenvectors) indicate the relative contribution of each grid to the corresponding canonical pattern. The time series for this pattern is shown in Fig. 3.9c.

The first canonical mode represents a pattern of covariability that is located in eastern Europe and western Russia. The snow cover and 2-m temperature patterns for this mode explain about 15% and 24% of the total variance of each field, respectively. This mode shows that years with excessive (deficient) snow cover over eastern Europe from February to March are those with anomalously cold (warm) spring 2-m temperature over the area stretching from about 15° E in eastern Europe, western Russia, and parts of Scandinavia. Indeed there is close correspondence between the geographical area of anomalous land surface forcing from snow (highest loadings in Fig. 3.9a) on the lowest atmosphere as suggested by this CCA mode and the area exhibiting highest FMA snow-cover interannual variability (Fig. 3.7). In addition to providing some empirical evidence in support of snow-radiation (e.g., increasing ground reflectance) and snow-hydrological (e.g., energy used for melting snow and evaporating the resulting water) effects on 2-m temperature, the maps also show the spatial extent of the snow influence. The results show that the impact of anomalous snow-cover forcing could occur through local feedback mechanisms and possible changes in atmospheric circulation. The effect of snow-albedo-temperature feedbacks is more localized (e.g., Dewey, 1977), which explains the eastern Europe case. The impact of snow on atmospheric circulation can extend much deeper into the middle or even the upper troposphere (e.g., Zhang et al., 2004) thus exerting a remote influence on the weather/short-term climate.

The canonical component time series for this mode whose correlation is 0.91 show that this pattern of anomalously extensive snow cover and the associated colder 2-m temperatures in eastern Europe occurred more frequently from the 1970s to

the late 1980s (Fig. 3.9c). The frequency declined since the 1990s. Possible mechanisms forcing this pattern of temporal variation have not been investigated in this paper. A statistically significant reduction in western Eurasia ( $40^{\circ}$ – $60^{\circ}$  N,  $20^{\circ}$ – $90^{\circ}$  E) spring (particularly April) snow-cover extent (SCE) has been shown elsewhere (Brown, 2000) using reconstructed snow-cover data. Superimposed to the significant downward SCE trend shown in Brown (2000) are decadal-multidecadal fluctuations. Consistent with our findings, the decade from the late 1970s to the late 1980s fell above the trend line (Brown's Fig. 14) with a more rapid decline in the early 1990s. A link between snow cover and concurrent NAO cannot be ruled out. The correlation between the snow-cover canonical time series for this mode and the FMA-averaged NAO-Gibraltar index (Jones et al., 1997) is 0.34 (statistical significance at the 5% level).

### 3.4.2 Model snow predictions

#### *Forecast – observed snow correlation*

To determine the performance of the CGCMs in terms of snow extent predictions, the FMA model snow predictions are validated against NOAA/NESDIS snow data using correlation analysis. The FMA CGCMs snow predictions issued in February are considered, implying zero lead time. Snow extent is defined as the area covered by at least 3-mm thickness of SWE for the model data, which have been interpolated to a  $2^{\circ} \times 2^{\circ}$  latitude-longitude grid consistent with the validation dataset. The spatial pattern of correlation between model FMA snow conditions and observed snow cover is shown in Fig. 3.10. At the 5% (1%) level, a correlation coefficient of 0.44 (0.54) is found to be statistically significant. Remarkably, in agreement with results from 2-m temperature forecast verification, statistically significant correlations are found over much of central and eastern Europe in GloSea and ECMWF S2 systems (Figs. 3.10a,b). For the NCEP CFS system, statistically significant correlations are only confined to a limited area in eastern Europe and around the Caucasus (Fig. 3.10c).

#### *Model representation of monthly snow variation*

To assess the discrepancies that exist between modeled and observed SWE interannual variations, a normalized standard deviation is calculated for February to April based on the 1987–2005 period and shown in Fig. 3.11. Assessing the models' ability to capture the snow migration at monthly time scales reveal more information than would have been obtained from the seasonal (FMA) patterns considered in foregoing sections. The dimensionless coefficient used to make the assessment is the ratio of the standard deviation to the monthly mean SWE. In the figure, each

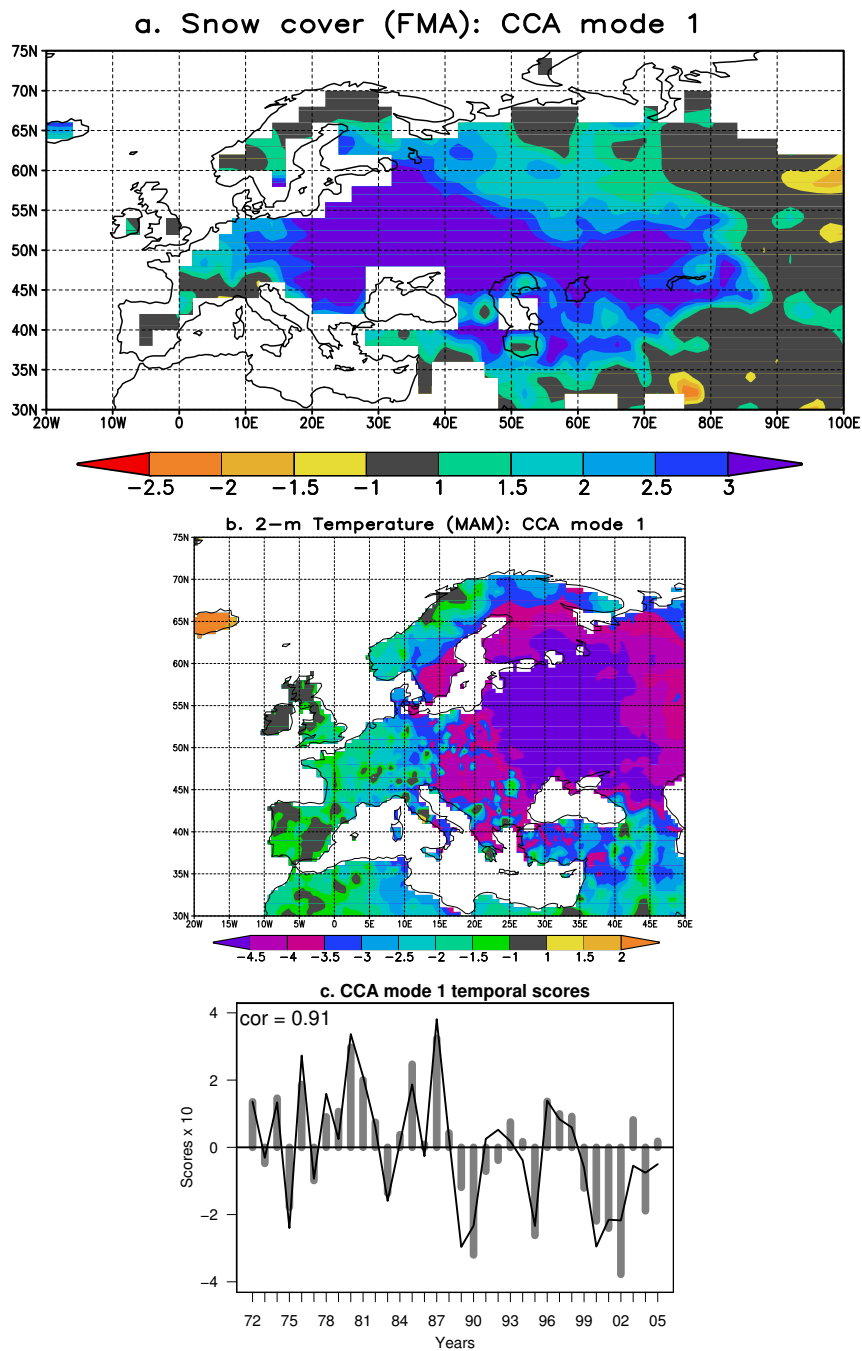


*Fig. 3.9:* CCA diagnostics: (a) FMA snow-cover CCA loadings for mode 1, (b) the corresponding CCA loadings for MAM 2-m temperature, and (c) the canonical component time series for snow (gray bars) and 2-m temperature (line).

column shows the spatial distribution of the statistic in the same month. These plots allow a visual comparison of the ability of the models to capture the year-to-year monthly snow variations expressed as a proportion of average monthly snow depletion. The monthly snow line can be inferred from the plots.

In February, the observed snow line stretches from the Alps in southeastern France (about 5° E) southward into Bulgaria and northward through Germany toward Scandinavia (Fig. 3.11a). The year-to-year February SWE variation is highest in eastern Europe where the standard deviation either equals or exceeds the mean. All the models satisfactorily capture the broad pattern of February SWE variability. GloSea and ECMWF S2 also capture the mean SWE amounts adequately (map not shown). The NCEP CFS model, while locating the snow boundary close to the observed, underestimates the thickness of the snowpack over eastern Europe. Such an underestimate in snow depth would result in a subsequent underestimate of snow properties such as its albedo, which is one factor that influences the short-term climate, particularly near-surface temperatures.

By March the snow line in the observations does not retreat significantly with the westmost boundary still located over the French and Swiss Alps (Fig. 3.11b). Remarkably, year-to-year SWE in eastern Europe exhibits the highest variation during this month. In this snow-transient region, interannual standard deviations as high as twice the monthly mean are found. Indeed, the thickness and area extent of the snowpack during this month has a direct impact on spring near-surface temperature in the lowest quintile. The observed magnitude of March SWE variability in eastern Europe is adequately represented in the GloSea and ECMWF S2 models (Figs. 3.11e,h). This accuracy shows that in years when snow occurred in eastern Europe in March, GloSea and ECMWF S2 hindcasted/predicted the thickness of the snowpack successfully. As noted in Slater et al. (2001), snow albedo changes in models' snow-albedo schemes as a function of its age and depth (up to a certain limit after which it becomes constant). In their discussion, most models attain a maximum albedo of about 85% for the visible, and about 65% for the near-infrared portions of the spectrum at SWE values less than 50 mm. Climate models that predict snow thickness at these "crucial" levels with some skill should commensurately represent the magnitude of the land surface forcing on the lower atmosphere reasonably well, thereby predicting cold spring seasons with some degree of accuracy. As shown in Fig. 3.11k, the NCEP CFS system hardly predicts any snow in eastern Europe in March. In this model the snow boundary migrates too rapidly so it is situated much farther east (western Russia) than the climatological snow line. This serves as a clear illustration of differences in model snow simulation during the melt season. Discrepancies in model snow simulations during transition seasons have been noted elsewhere (e.g., Foster et al., 1996) and are in part attributable to differences in parameterization of snow processes in the

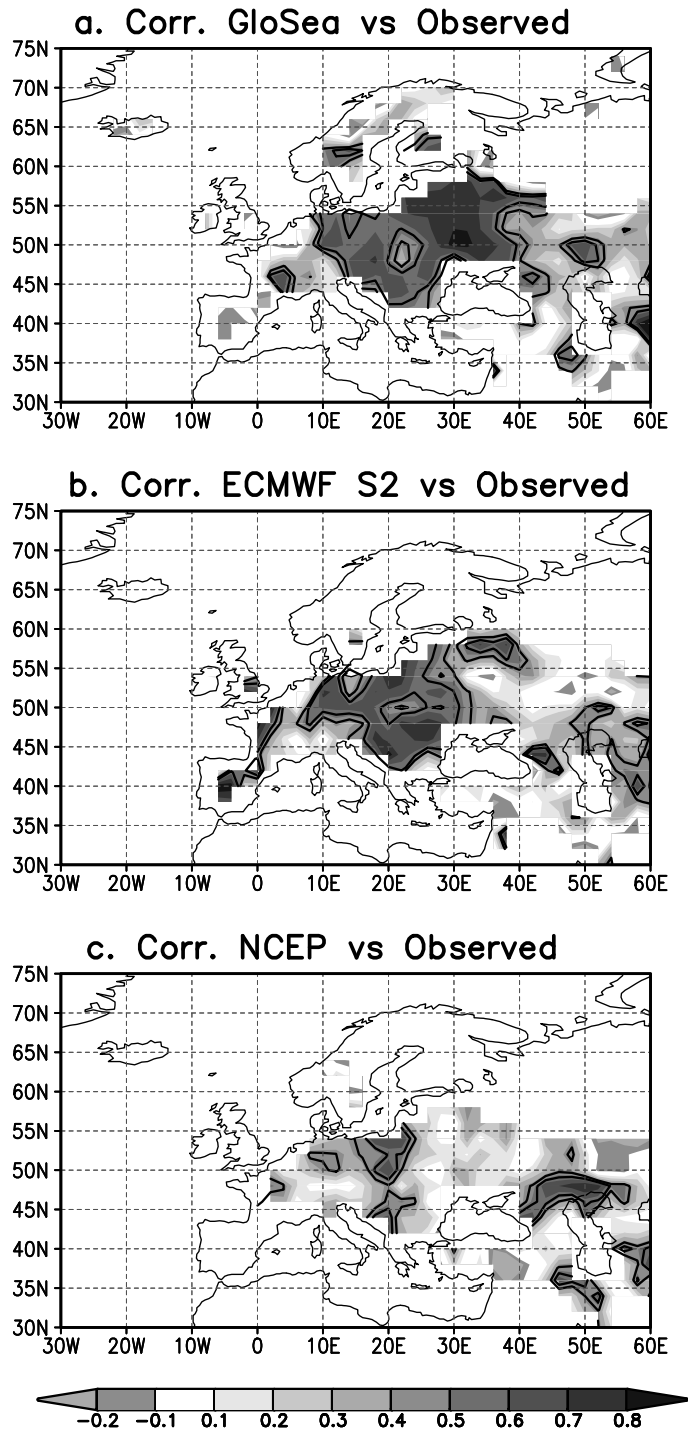


*Fig. 3.10:* Spatial pattern of correlation between modelled FMA snow cover and NOAA/NESDIS observations: the correlation for the (a) for the GloSea model, (b) ECMWF S2, and (c) NCEP CFS. The critical values for statistical significance at the 5% (1%) error level are 0.44 (0.54), and are shown by contours in the figure.

models' land surface schemes (Slater et al., 2001).

Except for patches of snow over the Swiss Alps and the Caucasus, there is no observed or modeled snow over Europe in April (Figs. 3.11c,f,i,l). This is in response to the seasonal increase in available solar energy that forces a rapid migration of the climatological snow line. The snow patches in the Swiss Alps and the Caucasus are well predicted in the ECMWF S2 and GloSea models. In extreme cases (e.g., April 1996) some remnants of seasonal snow still survive during this month over much of eastern Europe and western Russia resulting in a delayed onset of seasonal warming. During this extreme case, the GloSea model accurately captured the delayed migration of the seasonal snow line (map not shown). The ECMWF S2 and NCEP CFS models on the other hand located the snow boundary much farther east along the western Russian border.

### 3.5 Discussion and conclusions

Predicting land temperatures more than 14 days ahead is a difficult task. One of the few extratropical areas with high skill scores in the current generation of operational seasonal forecast models is central and eastern Europe in spring. Forecasts started on 1 February show some skill as evidenced by ROC scores for the below-median MAM-averaged temperature exceeding 0.6. The skill for forecasting cold extremes is even higher (reaching 0.8) and statistically significant. The models' skill surpasses that of damped persistence forecasts.

Comparisons of skill measures for below-median and colder spring (2-m temperature in the lower quintile) for each CGCM suggests that there could be more predictive potential for cold extremes than "normal" seasons at the short lead time considered here. This is indeed the case over snow transient regions in central and eastern Europe. A notable difference in the skill of the CGCMs used in this research is evident. The GloSea and ECMWF S2 models attain the highest overall skill in predicting spring cold extremes during the verification period. The NCEP CFS model on the other hand performs the least well.

Noting that cold spring forecasts have higher skill than below-median seasons prompted a further investigation of the physical basis of the higher skill in predicting 2-m temperatures in the lowest quintile. The correspondence in geographical area between the high-skill area and the climatological snow line hinted at land surface processes as a possible source. Both remotely sensed and model-generated snow fields have been used to test our hypothesis. Both datasets inherently have their own biases. However, the close agreement between the two datasets over the study area suggested that they could reliably be used for the purpose of this paper.

Correlation analysis has shown a statistically significant relationship between mod-

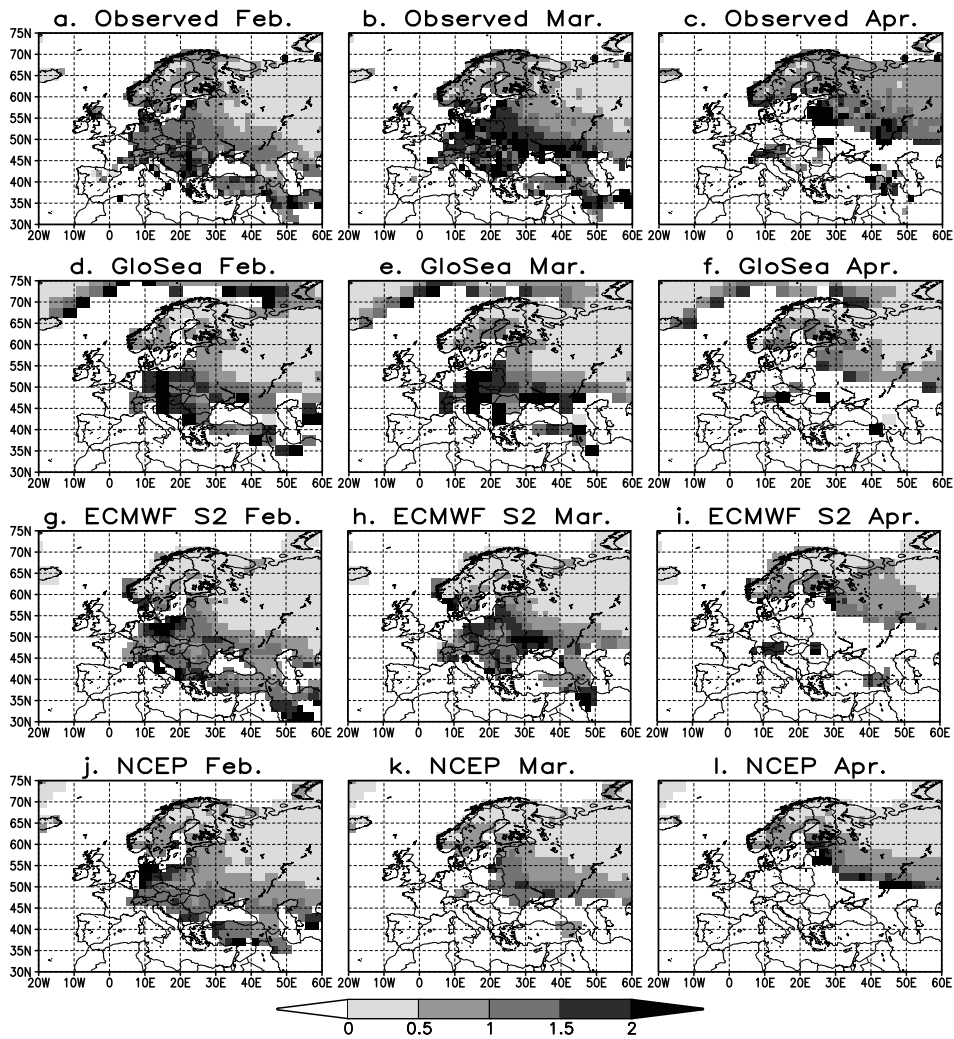


Fig. 3.11: Snow-depth-normalized standard deviation (coefficient of variation) over Europe from February to March: (a), (b), (c) the observed SWE variation; (d), (e), (f) GloSea; (g), (h), (i) ECMWF S2; and (j), (k), (l) NCEP CFS. Coefficients are shown for (a), (d), (g), (j) February; (b), (e), (h), (k) March; and (c), (f), (i), (l) April.

eled snow cover and the NOAA/NESDIS datasets over eastern Europe. The highest correlations ( $> 0.5$ ) were obtained for the GloSea system. Albeit of a lesser magnitude, correlations attained by the ECMWF S2 model were statistically significant over a large area. The NCEP CFS model had the lowest overall correlations. It is remarkable that the snow predictions from GloSea and ECMWF S2 are in closer agreement with observations and that the same models show higher skill in predicting cold spring seasons. This consistency provides evidence that the CGCMs' different ability to accurately model snow cover is a physical basis for the skill differences shown in the previous sections.

The abilities of the models to mimic the monthly migration of the climatological snow line and interannual variability of monthly SWE during the melt season further substantiates the snow-being-the-source hypothesis. Notable discrepancies in the models' ability to accurately locate the monthly climatological snow boundary and the year-to-year variations in monthly snow thickness have been shown. Again, the monthly snow line and the interannual variations of snow thickness in the GloSea and ECMWF S2 CGCMs models are very close to what is observed. In February, the NCEP CFS system predicts an almost realistic snow boundary but underestimates the thickness of the snowpack in eastern Europe. As snow albedo varies with snow depth (up to a certain limit) and age, underestimating the SWE in February would imply lower-than-observed albedo, and higher surface heat fluxes and hence warmer temperatures. In March, snow-depth variability is highest in eastern Europe. The NCEP CFS model misses the pattern of the interannual variability in March because the snow line migrates too rapidly in this model. In April all models faithfully represent the observed snow distribution.

The ability of GloSea and ECMWF S2 models to capture the observed pattern of interannual variability of February-April snow thickness suggests that these models adequately represent snow processes during the melt season. The NCEP CFS model on the other hand simulates a shorter snow season in eastern Europe, thus underestimating the amount of snow on the ground in February and March. The overall poorer performance shown by the NCEP CFS model in predicting cold springs in Europe could be attributable to the earlier melting of snow.

Patterns of covariability between FMA snow cover and MAM 2-m temperature have shown a link between snow cover in eastern Europe and western Russia and 2-m temperature, with temperature lagging a month behind. The patterns show that extensive snow cover from February to March has often preceded cold temperatures in spring. The underlying physics has been discussed extensively in the literature. Snow alters surface radiant energy fluxes through its high albedo and low thermal conductivity. Energy is extracted from the air during the melting process. Soil moisture from melted snow leads to a release of surface latent heat flux from the wet ground.



The initial snow conditions are important for cold spring season forecasts over Europe except over the western areas where temperatures are modulated by nearby oceans. High snow depth in eastern Europe and western Russia at the beginning of February (model initialization), persisting into early spring is closely related to cold springs in eastern Europe. Strong correlation shows that a thick snowpack early in February generally precedes lingering snow in spring. However, the dependence of snowpack duration on the ground on several factors complicates modeling of the snow fields during late winter and/or early spring. Over and above the seasonal increase in solar radiation, the frequency and strength of ablation events determines the snow durability. For instance, a large (or a sequence of) rainstorm(s) would provide large amounts of energy for melting the snowpack. Such rapid snowmelt would diminish the chances of an extremely cold spring. Therefore snow initial conditions would lead to skillful cold spring seasons' forecast if the CGCMs temperature and precipitation schemes were more realistic. The skill of the Development of a European Multimodel Ensemble System for Seasonal-to-Interannual Prediction (DEMETER) versions of the ECMWF S2 and GloSea models (Palmer et al., 2004) in predicting lowest-quintile spring 2-m temperatures over 1958/59–2001 has also been assessed. The Met Office model attains higher ROC scores over a wide area in eastern Europe extending into Scandinavia (map not shown). No attempt has been made to investigate the strengths and weaknesses of the individual land parameterization schemes used in the model. In a models' land surface schemes intercomparison study (Slater et al., 2001), it was noted that specific snow properties such as its albedo and thermal conductivity vary from model to model. Also the ablation rates were found to differ, which apparently is the case in the models used here as evidenced by the differing lengths of the snow season. It is clear that the predictive skill of spring cold spells in numerical models is tied to their accuracy in predicting snow fields.

#### 4. PROJECTED CHANGES IN MEAN AND EXTREME PRECIPITATION IN AFRICA UNDER GLOBAL WARMING. PART I: SOUTHERN AFRICA

This study investigates likely changes in mean and extreme precipitation over southern Africa in response to changes in radiative forcing using an ensemble of global climate models prepared for the Intergovernmental Panel on Climate Change (IPCC) Fourth Assessment Report (AR4). Extreme seasonal precipitation is defined in terms of 10-yr return levels obtained by inverting a generalized Pareto distribution fitted to excesses above a predefined high threshold. Both present (control) and future climate precipitation extremes are estimated. The future-to-control climate ratio of 10-yr return levels is then used as an indicator for the likely changes in extreme seasonal precipitation.

A Bayesian approach to multimodel ensembling is adopted. The relative weights assigned to each of the model simulations is determined from bias, convergence, and correlation. Using this method, the probable limits of the changes in mean and extreme precipitation are estimated from their posterior distribution.

Over the western parts of southern Africa, an increase in the severity of dry extremes parallels a statistically significant decrease in mean precipitation during austral summer months. A notable delay in the onset of the rainy season is found in almost the entire region. An early cessation is found in many parts. This implies a statistically significant shortening of the rainy season.

A substantial reduction in moisture influx from the southwestern Indian Ocean during austral spring is projected. This and the pre-austral spring moisture deficits are possible mechanisms delaying the rainfall onset in southern Africa. A possible offshore (northeasterly) shift of the tropical–temperate cloud band is consistent with more severe droughts in the southwest of southern Africa and enhanced precipitation farther north in Zambia, Malawi, and northern Mozambique.

This study shows that changes in the mean vary on relatively small spatial scales in southern Africa and differ between seasons. Changes in extremes often, but not

---

This chapter is based on the article “Projected changes in mean and extreme precipitation in Africa under global warming. Part 1: Southern Africa” by Mxolisi E. Shongwe, Geert Jan van Oldenborgh, Bart J. J. M. van den Hurk, Bas de Boer, Caio A. S. Coelho, and Maarten K. van Aalst, 2009, published in *Journal of Climate*, **22**, 38195–3837.

always, parallel changes in the mean precipitation.

#### 4.1 Introduction

Changes in the mean state of the earth's climate system due to anthropogenic modifications in the chemical composition of the earth's atmosphere have become a topical issue in recent years (Houghton et al., 2001; IPCC, 2007). Direct consequences of positive radiative forcing resulting from an enhanced greenhouse effect are changes in global surface and atmospheric temperatures, precipitation patterns, and other climate variables (IPCC, 2007).

Owing to their great impact on human activity and wide application, potential future changes in precipitation deserve much attention. A number of studies have sought the possible changes in long-term mean precipitation in many parts of the globe (Giorgi and Mearns, 2002, 2003; Trenberth et al., 2003; Tebaldi et al., 2004). Less attention has been paid to changes in extreme precipitation. Pronounced increases in heavy precipitation events might be expected to occur where mean total seasonal or annual precipitation increases. On the other hand, dry extremes might be expected to become severe where mean precipitation decreases. However, in cases where the interannual rainfall variance increases, it is possible that changes in the probability of extreme precipitation events may not parallel that of mean seasonal or annual precipitation. For instance, the severity of heavy precipitation events may increase in regions where the total precipitation decreases or remains constant. Since precipitation extremes often have bigger impacts on society than small changes in average precipitation, an investigation of extremes' behavior under changing climatic conditions is warranted.

Several studies have investigated the likely changes in mean and extreme precipitation in many parts of the globe, including Africa (Kharin and Zwiers, 2000; Groisman et al., 2005; Meehl et al., 2005; Kharin et al., 2007). Most of these studies have focused on likely patterns of change over large regions of Africa despite the high degree of spatial variability exhibited by precipitation. Regionally specific studies have been carried out in other parts of the globe (e.g., van Ulden and van Oldenborgh, 2006; van den Hurk et al., 2006), but few for Africa and even fewer for southern Africa.

Hulme et al. (2001) reviewed previous African climate change studies and report on observed (twentieth century) and likely future (twenty-first century) mean annual temperature and precipitation patterns in Africa. Using seven global climate models (GCMs), significant decreases in mean December–February (DJF) precipitation were found in the interior southern Africa south of about 10° S (most of South Africa, Botswana, and Namibia) in the A2-high scenario. These projected decreases are substantial after 2050 (their Fig. 10). Sources of uncertainty in

African climate change scenario studies are also discussed (Hulme et al., 2001). Previous southern African climate change studies investigating extreme events (e.g., Joubert et al., 1996; Mason et al., 1999) used either simulations by a single climate model or earlier version(s) of a few climate models. Using an earlier version of the Commonwealth Scientific and Industrial Research Organisation (CSIRO) coupled general circulation model (CGCM), Joubert et al. (1996) found an increase in the probability of dry years over the southwestern parts of southern Africa and southern Mozambique under 2 x CO<sub>2</sub> experiments. However, southern African mean annual precipitation was not found to change significantly. Mason et al. (1999) found an increase in the frequency of extremely wet daily events. Consistent with Joubert et al. (1996), no significant trend in mean annual precipitation was reported. Here, we conduct a detailed regional analysis by combining results from an ensemble of objectively selected state-of-the-art climate models to investigate likely long-term (up to 2200) changes in mean and extreme precipitation.

Over the past decades, climate-related extremes have been the dominant trigger of natural disasters in southern Africa (here defined as Botswana, Lesotho, Malawi, Mozambique, Namibia, South Africa, Swaziland, Zambia, and Zimbabwe). New et al. (2006) identified significant trends in southern Africa temperature extremes and some precipitation indices. In particular, a spatially coherent increase in consecutive dry days was found over much of southern Africa in the last decades of the twentieth century. Upward trends in intense precipitation were found to the southeast with trends of the opposite sign in northern Namibia, Botswana, and Zambia.

Concurrently, the number of disasters is on the rise. According to the International Emergency Disasters Database (EM-DAT; <http://www.em-dat.net/>), the average annual number of reported natural disasters in the region has risen from about 5 reported disasters a year in the 1980s to over 18 a year from 2000 to 2006. Hydrometeorological disasters make up the bulk of those (the others are mostly epidemics such as malaria, cholera, and meningitis, which are also affected by climatic conditions). Reported drought-related disasters have risen from an average of about 1.5 per year in the 1980s to about 2 per year since 2000, while those related to floods have risen from 1.2 a year to almost 7 per year since 2000 (the rest of the reported increase is mainly due to wind storms). In the past years, these events have affected the lives and livelihoods of over six million people annually and had severe impacts on economic performance and poverty alleviation (e.g., Hellmuth et al., 2007). While part of the trend is due to better reporting, it also reflects a rising vulnerability to natural hazards, and potentially an underlying trend in climate variability and extremes. Operational disaster managers, for instance from the Red Cross and Red Crescent, also report an increasing pressure

on humanitarian assistance and express concern that trends in weather extremes due to climate change increasingly affect their work (e.g., van Aalst et al., 2007). Among others, they are looking for better analyses on how extreme weather events may be changing so as to enhance disaster preparedness among poor rural communities and help integrate climate risk management into development planning. These concerns and questions have provided the motivation for the present study. Of particular interest is examining likely changes from the present to the late twenty-first and twenty-second centuries (i.e., the 2051–2200 period) in the severity of droughts and floods in specific regions of Africa and a comparison with changes in mean precipitation. With the vulnerable local communities and high spatial variation of rainfall in mind, this study probes into simulated precipitation changes at spatial scales smaller than the commonly used Giorgi regions (Giorgi and Francisco, 2000). Here, we show that averaging over large areas can conceal notable spatial variations in the modeled rainfall response to an enhanced greenhouse effect. Likely changes in large-scale atmospheric hydrodynamics are assessed and related to changes in precipitation patterns. Results obtained for southern Africa are presented in this chapter. Chapter 5 presents the results for East Africa. In spite of the associated uncertainties (e.g., Hulme et al., 2001), the results presented below can inform adaptation strategies for governments, the private sector, and communities in the regions covered in this study.

## 4.2 Data and Methods

### 4.2.1 Model simulations and observations

This study uses the World Climate Research Programme (WCRP) Coupled Model Intercomparison Project phase 3 (CMIP3) multimodel dataset. The model dataset formed input to the Intergovernmental Panel on Climate Change (IPCC) Fourth Assessment Report (AR4) (IPCC, 2007). Correlation between modeled and Climate Research Unit (CRU) monthly precipitation and the rms error (RMSE) is used to assess the degree of realism with which models available on the Program for Climate Model Diagnosis and Intercomparison (PCMDI) archive simulate the observed twentieth century precipitation (the 20c3m runs). With this first low-threshold selection, 12 models were selected and are listed in Table 4.1. For details of each model formulation, the reader is referred to the references cited in the table. The model spatial resolutions differ considerably. As the focus of this study is on relatively small spatial scales, for ease of comparison, the model simulations are linearly interpolated to a common T95 ( $1.25^\circ \times \sim 1.24^\circ$  latitude–longitude) grid.

The availability of long integrations from the Special Report on Emissions Scenar-

ios (SRES) A1B forced runs enable the assessment of possible long term climate change signals. In this scenario, CO<sub>2</sub> concentration doubles by 2100 and remains constant thereafter. These SRESA1b model data are subdivided into two subsamples: the 1901–2000 and the 2051–2200 periods, defining the control and future climate, respectively. Considering the 2051–2200 period is sensible because, in most cases, changes in model predictions before and after 2100 (CO<sub>2</sub> doubling) are smaller than the internal variability. For climate models with multiple integrations (n20c3m and nSRESA1b; Table 4.1), each ensemble member is considered an independent realization. The ensemble members are then concatenated to form a larger sample for each model from which further analyses (see section 4.2.3) are carried out.

To identify the atmospheric anomalies and/or moisture attributes associated with precipitation changes, other fields (e.g., wind and specific humidity) from the model simulations are also used. The computation of moisture transport, for example, requires data on finer temporal resolution than the monthly simulations used to estimate precipitation changes. Daily simulations from the same CGCMs listed in Table 4.1 are used, except for the third climate configuration of the Met Office Unified Model (HadCM3) and Hadley Centre Global Environmental Model version 1 (HadGEM1), whose data are not available on the PCMDI archive. The PCMDI archive contains only daily data for shorter time slices (e.g., 1961–2000, 2046–65, and 2081–2100) and, therefore, the analysis of these quantities will be based on these shorter periods.

Observed twentieth-century precipitation data used in this study comprise station observations obtained from the Global Historical Climatology Network (GHCN) (Peterson et al., 1997) and gridded data from the Climate Research Unit (CRU TS2.1) (New et al. 2000) datasets. The former is only used to define homogeneous rainfall regions (see section 4.2.2). The latter is used in all analyses described in sections 4.2.3 and 4.2.4. The biases inherent in these datasets notwithstanding, their quality is sufficient for the present study.

Prior to the analysis of precipitation changes, the data have been screened for possible trends. Except for clear patterns of low-frequency precipitation variability in some regions, significant twentieth-century precipitation trends are not discernible. Detrending the series prior to the analysis is therefore deemed unnecessary. The mean seasonal precipitation rates used here are separated by 12 months. Clusters of extremes may only reflect interdecadal variability rather than serial dependence. For this reason, declustering the time series has also been deemed unnecessary.

Because of its geographical diversity, Africa is divided into four subregions: southern Africa, East Africa, northeast Africa, and West Africa. As aforementioned, this paper present results obtained for southern Africa (defined here as the area ly-

Tab. 4.1: Global coupled climate models used in this study. Model resolution is given as T (wavenumber of spectral truncation) and L (number of vertical layers). The number of ensemble integrations by each model in the twentieth century and future climate (2051–2200) are shown in the columns with headings n20c3m and nSRESA1b, respectively.

Contributing Centre	Model	Atmospheric Resolution	n20c3m	nSRESA1b	References
Canadian Centre for Climate Modelling and Analysis (CCCMA)	General Circulation Model version 3.1 (GCM3.1)(T47)	T47L31	5	5	Flato (2005)
Météo-France	CNRM-CM3	T42L45	1	1	Salas-Méla et al. (2005)
CSIRO	CSIRO Mark version 3.0 (Mk3.0)	T63L18	3	1	Gordon et al. (2002)
Max Planck Institute (MPI)	ECHAM5/MPI Ocean Model (OM)	T63L31	3	3	Roeckner et al. (2003)
Meteorological Institute of the University of Bonn (MIUB)	ECHO-G	T30L19	3	3	Min et al. (2005)
GFDL	GFDL CM2.0	2° × 2.5° L24	3	1	Delworth et al. (2006)
GFDL	GFDL CM2.1	2° × 2.5° L24	3	1	Delworth et al. (2006)
L'Institut Pierre-Simon Laplace (IPSL)	IPSL Coupled Model version 4 (CM4)	2.5° × 3.75° L30	1	1	Le Clainche et al. (2001)
Center for Climate System Research/National Institute for Environmental Studies/Frontier Research Center for Global Change (CCSR/NIES/FRCGC)	Model for Interdisciplinary Research on Climate 3.2, medium resolution version [MIROC3.2 (medres)]	T42L20	3	1	Hasumi et al. (2004)
MRI	MRI-CGCM2.3.2	T42L30	5	1	Yukimoto and Noda (2001)
Met-Office (UKMO)	UKMO-HadCM3	2.5° × 3.75° L19	2	1	Gordon et al. (2000)
UKMO	UKMO-HadGEM1	1.25° × 1.875° L38	2	1	Johns et al. (2004)

ing between  $\sim 35^\circ$  and  $10^\circ$  S,  $20^\circ$ – $42^\circ$  E; Fig. 4.1). Results for other regions are presented online at [http://www.knmi.nl/africa\\_scenarios/](http://www.knmi.nl/africa_scenarios/). Because of sparsity of reliable observations in certain parts of southern Africa (e.g., Angola and Democratic Republic of Congo), these areas have been omitted from the analysis.

Much of southern Africa has a well-defined rainy season during austral summer months and is characterized by distinct atmospheric dynamics (Tyson and Preston-Whyte, 2000). In this study, future patterns of southern Africa mean precipitation change in austral spring [September–November (SON)], summer [December–February (DJF)], autumn [March–May (MAM)], and winter [June–August (JJA)] are investigated. Extreme precipitation change analysis is only carried out for the peak of summer (DJF), when most precipitation and extreme events typically occur (Tyson and Preston-Whyte, 2000). Monthly CRU and CMIP3 precipitation is accumulated into seasonal (3 month) totals from which mean precipitation rates ( $\text{mm day}^{-1}$ ) are calculated by dividing by the number of days in that season. The climatologically wettest seasons have the highest mean precipitation rates—from either a few very intense rainfall events or prolonged wet spells within that season. On the other hand, the driest seasons (drought events) have the lowest mean precipitation rates.

#### 4.2.2 Clustering stations

Mean precipitation and return levels (section 4.2.3) exhibit pronounced spatial variabilities. This is largely in response to inhomogeneities in land surface features (e.g., topography and land-sea-lake contrasts). Such localized forcing features are expected to modulate the precipitation response to changes in radiative forcing. For this reason, using the GHCN data, homogeneous rainfall regions are identified within southern Africa using cluster analysis (Mimmack et al., 2001). Rainfall homogeneity is defined on the basis of the spatial coherence of interannual rainfall variations.

Prior to the clustering, annual precipitation totals are first calculated using the July–June year. The annual totals are then clustered using single linkage, average linkage, complete linkage, and Ward’s agglomerative hierarchical algorithms (Johnson and Wichern, 2002). Each hierarchical procedure is based on Euclidean distances between station rainfall data, standardized by removing the mean and dividing by the mean absolute deviations.

Of the clustering methods used, the Ward minimum error sum of squares procedure yielded the most sensible results. The results from average linkage and complete linkage methods are broadly similar to those from Ward’s method. Poorly separated clusters representing less distinct regions are merged if the regions are contiguous. In addition, transitions between regions have been smoothed and straight lines used to delineate region boundaries. For these reasons, the resulting



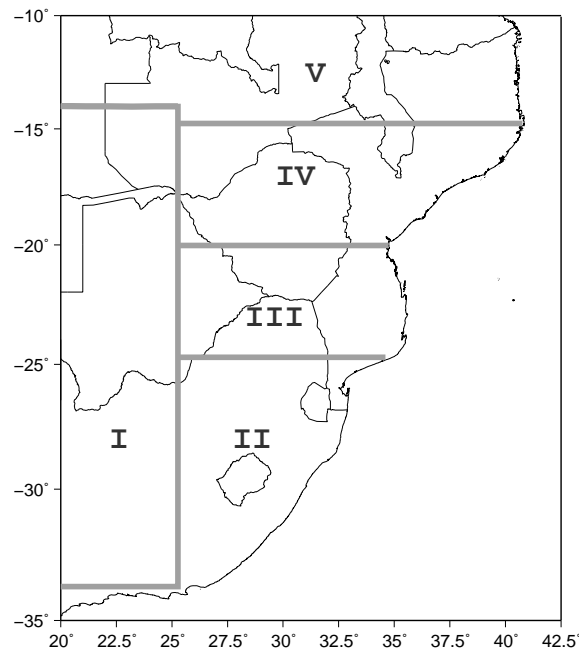


Fig. 4.1: Location map of southern Africa climatic zones identified using Ward's minimum variance clustering method.

climate regions shown in Fig. 4.1 differ from those identified by Shongwe et al. (2006). Here we used 212 stations spanning the period 1941–97 in contrast to the 255 stations and shorter period (1961–2000) used previously (Shongwe et al., 2006). Furthermore, in Shongwe et al. (2006), the clustering was based on Euclidean distances calculated from unstandardized principal component scores of individual monthly rainfall data, as recommended by Mimmack et al. (2001). Observed seasonal precipitation for each homogeneous zone is calculated from the CRU datasets by averaging grid points that fall within it. Gridded CRU precipitation data, which is based on the GHCN station data and automatically gives equal weight to equal areas, is preferred for further analysis (see sections 4.2.3 and 4.2.4 below). CGCM grids falling within each climatic zone were similarly averaged. In this way, the spatial noise inherent in precipitation has been filtered out.

#### 4.2.3 *Extreme value analysis*

The analysis of changes of extreme precipitation events is based on the peak-over-threshold method or generalized Pareto distribution (GPD). In contrast to using the raw (model) data, fitting a GPD allows interpolation, extrapolation, and intermodel comparison. A comprehensive introduction to GPD and its applications can be found in Coles (2001). Details of the extreme value model applied here are presented in appendix A.

Conventionally, most extreme value studies in climate science (e.g., Kharin and Zwiers, 2000; Meehl et al., 2005; Kharin et al., 2007) evaluate return levels or quantiles of a GPD. In this study, 10-, 20-, 50-, and 100-yr return levels have been estimated. However, given the small sample size of threshold excesses, only the 10-yr return levels are shown. These estimates are interpolated from the data, rather than extrapolated, and hence are least biased. Results for longer return levels are available online at [http://www.knmi.nl/africa\\_scenarios/](http://www.knmi.nl/africa_scenarios/). Ten-year return levels ( $\text{mm day}^{-1}$ ) are computed in both control and future climate. These levels express the average intensity of precipitation in an extremely wet or dry season that occurs on average once every 10 years (corresponding to 10% probability that a given season is wetter or drier than this).

Anderson-Darling goodness-of-fit tests (Laio, 2004) have been used to assess the suitability of the GPD as a model of excesses above the predefined threshold. The mathematical formulation of this test is shown in appendix B. The test statistics and critical values are determined from the National Institute of Standards and Technology software available online at <http://www.itl.nist.gov/div898/software/dataplot.html>.

#### 4.2.4 *Multi-model ensembling*

Uncertainties in long-term climate model simulations can be classified as those due to natural climate variability, model different responses to a given forcing (such as increases in greenhouse gas concentration), model imperfections under the control forcing, and those associated with the emission scenarios used to force the climate models. For these reasons, no single model is considered accurate. Many climate studies utilize results from a range of climate models (e.g., Kharin et al., 2007).

Considerable research is devoted to methods for combining simulations from climate models (e.g., Giorgi and Mearns, 2002, 2003; Tebaldi et al., 2004, 2005). This paper adopts the Bayesian method defined by Tebaldi et al. (2005). The inherent advantage of this method is that uncertainties of the measures of interest can be inferred from their posterior distributions, which combines simulation information from all climate models. This method uses model bias, convergence be-

tween model projections, and correlation to determine the relative weights given to each member in the multimodel ensemble. Model bias is defined with respect to the twentieth-century climate, whereas convergence measures the distance of the individual model projection from the location of the multimodel ensemble. Models that simulate the observed climate with some skill and agree with the rest in their future projections receive more weight. On the other hand, outliers, which show large biases with respect to the observed climate, are weighted least. Correlation between the individual model's deviations from the multimodel ensemble mean in the present and future climate is also incorporated in the weighting criteria. In this way, models with systematic biases are further downweighted. The bias and convergence criteria for determining weights assigned to each member in the ensemble has been applied previously (Giorgi and Mearns, 2002, 2003). No specific criteria for assigning weights to model predictions can be considered optimal. For instance, it is quite possible that several models that exhibit similar performance in simulating the observed twentieth-century climate still produce quite different projections for the future climate. The risk of discounting the best model when it is an outlier with respect to the rest is inevitable from the convergence criterion. Notwithstanding, these weighting criteria bear enough theoretical and statistical basis to justify their use.

Fuller details of the statistical treatment of the problem may be found in Tebaldi et al. (2005). Here, adopting their notation, it suffices to show the measure of percentage precipitation change as

$$\Delta P = 100\left(\frac{\nu}{\mu} - 1\right), \quad (4.1)$$

where  $\nu$  and  $\mu$  are used to designate the mean of the multimodel ensemble in the future and control climate, respectively. For mean precipitation rates and 10-yr wettest events,  $\Delta P > 0$  is indicative of an increase in their intensity, while an increase in the severity of 10-yr driest events is indicated by  $\Delta P < 0$ .

### 4.3 Projected precipitation changes

Mean precipitation in each month computed from the twentieth-century (1901–2000) CRU gridded data, spatially averaged over each zone, is shown in Fig. 4.2. Almost everywhere in the region, seasonal rainfall commences around austral spring months (SON) and ceases around autumn months (MAM). DJF is the peak of the rainfall season, while JJA is typically dry (less than  $1 \text{ mm day}^{-1}$ ). This section begins by presenting likely changes in mean precipitation during transition seasons. We then discuss the projected changes in mean and extreme precipitation during the peak summer months (DJF). Projected changes in winter

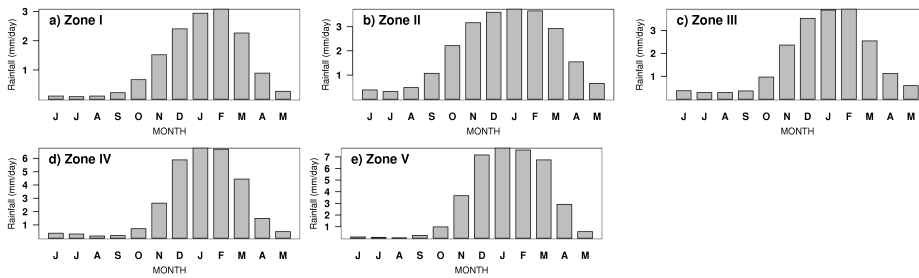


Fig. 4.2: Annual cycle of southern Africa precipitation derived from the 1901–2000 CRU gridded data. Zone labels are as indicated in Fig. 4.1.

precipitation, which are of little social and economical significance, are shown in section 4.4.1.

To allow a concise visual interpretation, we present the results for the percentage change in precipitation [ $\Delta P$ ; Eq. 4.1] for each climatic zone (Fig. 4.1) as the mean change with the corresponding 95% confidence interval derived from the Bayesian method. In each case, statistical significance at the 5% level (i.e.,  $p < 0.05$ ) is found whenever the 95% confidence region excludes zero (i.e., the null hypothesis of no change). Significance at the 1% level ( $p < 0.01$ ) is also tested. Whenever statistical significance in the projected changes is achieved, the number of CGCMs (out of the 12) projecting a change of the same sign as the mean change is shown. This is to demonstrate that the Bayesian weighting procedure is not doing anything weird.

#### 4.3.1 Changes in transition season mean precipitation

A spatially coherent and significant reduction ( $p < 0.05$ ) in austral spring (SON) mean precipitation is found everywhere in southern Africa (Fig. 4.3a). Reductions in SON precipitation have implications for seasonal rainfall onset in southern Africa. To the west (zone I) and over Zimbabwe and central Mozambique, a reduction exceeding 20% is simulated with the lower bound of the 95% posterior interval of  $\Delta P < -35\%$ . Almost everywhere in the region, the entire range of percentage reduction in SON precipitation excludes zero, indicative of a considerable consensus across the models. This, together with spatial coherence of this pattern of change, strengthens the belief that this is a consistently modeled climate change signal. Tadross et al. (2005) present the climatology of rainfall onset in southern Africa. Areas to the south experience an earlier rainfall onset from extratropical circulation systems such as frontal depressions and cold-core cutoff lows

(Tyson and Preston-Whyte, 2000). Albeit relatively small ( $\sim 10\%$ ), the simulated SON precipitation decrease over eastern South Africa (zone II) is significant. To the north and west, where precipitation is predominantly of tropical origin (Tyson and Preston-Whyte, 2000), reduction in spring precipitation attains significance at the 1% level.

Projected changes in mean autumn (MAM) precipitation rates are displayed in Fig. 4.3b. Over zones I and III (much of Botswana and southern Zimbabwe), the simulated mean reduction of  $\sim 15\%$  attains statistical significance at the 1% level. In zone IV (northern Zimbabwe and central Mozambique), the mean reduction ( $\sim 10\%$ ) is barely significant at the 5% level. Considering that a notable delay in rainfall onset is simulated in these areas, projections for an early cessation of seasonal rains suggest a contraction of the rainfall season. Farther north, in zone V (northern Mozambique, Zambia, and Malawi), MAM precipitation is expected to increase by  $\sim 10\%$ . A shift in the rainfall season to later months is implied. Little or no change in MAM precipitation is projected in eastern South Africa, which implies a shortening of the rainy season.

#### 4.3.2 Changes in mean and extreme summer precipitation rates

Figure 4.4 displays probable changes in summer (DJF) precipitation rates. There is evidence for a dipole pattern of change in mean precipitation rates (Fig. 4.4a). The negative pole is found to the western parts featuring the arid Kalahari and its boundaries (zone I). Here, the projected reduction in DJF mean precipitation rates ( $\sim 11\%$ ) is significant at the 1% level. Farther north, in the positive pole (zone V), the simulated changes, albeit subtle ( $\sim 4\%$ ), are significant at the 5% level. Separating the dipole is a large area to the east (zones II, III, and IV) with no significant changes in mean DJF precipitation rates. The presence of a dipole precipitation response to large-scale forcing (e.g., El Niño; Ropelewski and Halpert, 1987) has been found at interannual time scales. Its appearance here suggests that the climate change signal propagates into the southern Africa precipitation field through similar pathways (e.g., the tropical Indian Ocean SST pathway; Goddard and Graham, 1999; Washington and Preston, 2006).

Over the western parts of the subregion, 10-yr driest seasons are projected to increase their severity by more than 10% (Fig. 4.4b). These projections are significant at the 5% level. More severe droughts are also projected to the south of Zimbabwe and Mozambique. Albeit high in magnitude (averaging  $\sim 20\%$ ), these projections are not statistically significant. Elsewhere in the region, the models give little or no indications for a possible change in 10-yr driest events. Anomalous westerly circulations over the southeast Atlantic Ocean have been blamed for past droughts in much of southwestern Africa (Mulenga et al., 2003). The anomalous circulation patterns are related to the structure of the tropical-temperate cloud

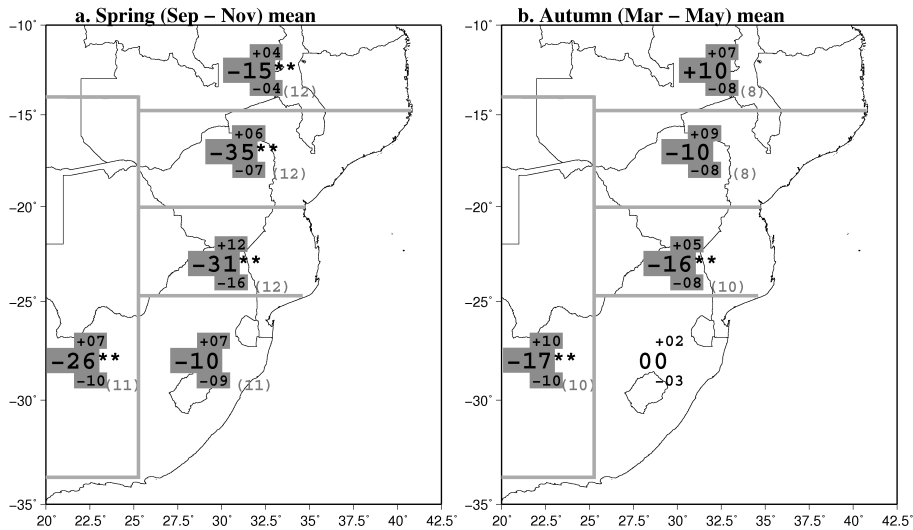


Fig. 4.3: Projected changes (%) in austral (a) Spring (Sep–Nov) and (b) Autumn (March–May) mean precipitation rates in each climatic zone. In each case, three values are plotted. The middle number gives the mean projected change preceded by its sign (+ve for increase and -ve for decrease). The number above (below) the mean change, preceded by a +ve (-ve) sign gives the distance to the upper (lower) critical value at the 5% level of significance. Projected changes significant at the 5% (1%) level are shaded in gray (shown by two asterisks). For statistically significant changes, the number of CGCMs (out of 12) projecting a change of the same sign as the mean change is enclosed in parenthesis.

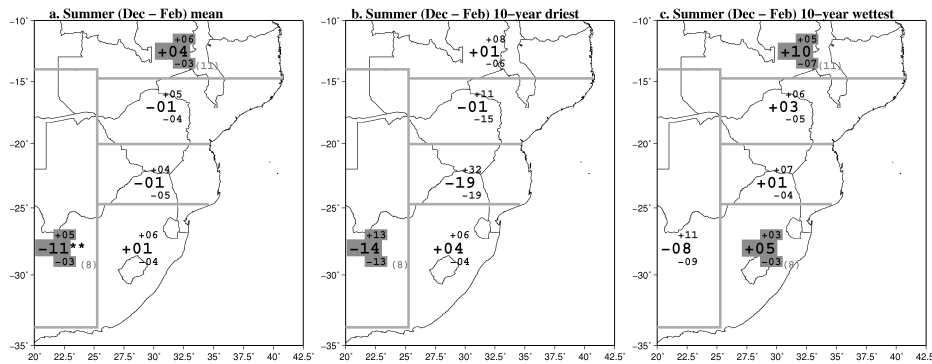


Fig. 4.4: Same as Fig. 4.3 but for austral summer (Dec–Feb): (a) mean precipitation rates, (b) 10-yr driest events, and (c) 10-yr wettest events.

bands (Todd and Washington, 1999). We postulate that these mechanisms might be present with similar consequences in the future climate. We shall return to this point in section 4.4.2.

Subtle but generally significant increases in 10-yr wettest events are found in eastern South Africa and farther north in northern Zambia, Malawi, and Mozambique (Fig. 4.4c). In the north, the magnitude of these changes average  $\sim 10\%$ . A slight and insignificant decrease in the intensity of 10-yr wettest events is projected in the western parts of southern Africa (Botswana and western South Africa: zone I). Elsewhere in the east (zones III and IV), subtle and insignificant increases are found. In the southern and eastern parts of the study area, flooding has often occurred from short-duration meso-scale events such as depressions (e.g., Rouault et al., 2002) and cutoff lows and by landfalling west Indian Ocean tropical cyclones (e.g., Reason and Keibel, 2004; Reason, 2007). While there are indications of possible changes in the intensity of the 10-yr wettest events, poor representation of small-scale systems (e.g., tropical cyclone activity) in CGCMs limit the confidence we have in these projected changes. The northern areas (zone V) are least affected by west Indian Ocean tropical storms. In these regions, wettest seasons are associated with prolonged sequences of wet days, which are dependent on the mean location and strength of large-scale convection. The projected changes in these regions are therefore more reliable.

The observed (1901–2000) and simulated (1901–2100) DJF precipitation time series for each zone are displayed in Fig. 4.5. In these plots, high frequency variability has been filtered out using a 10-yr running mean. Without exception, low frequency modes of variability have dominated southern African rainfall during

the last century. Such low-frequency rainfall fluctuations characterized by  $\sim 18$  yr cycle have long been noted in southern African climate variability (Tyson et al., 1975). Decadal variability is seen to continue in the future although the spread in the model projections increases. Unlike here, where the models are equally weighted, the outliers [e.g., the GCM3.1 (T47) and Centre National de Recherches Meteorologiques Coupled Global Climate Model, version 3 (CNRM-CM3) models for DJF] causing the observed large spread are downweighted by the Bayesian method in Figs. 4.3, 4.4 and 4.7. In most cases, the Bayesian weighting reduces the spread by more than a factor 2. Notwithstanding the large spread, some future patterns emerge. A notable upward trend is projected by a large fraction of the multimodel ensemble over northern Zambia, Mozambique, and Malawi (Fig. 4.5e). This upward trend is steeper after 2050. A similar albeit weaker trend is simulated in eastern South Africa (Fig. 4.5b). On the other hand, a tendency for drier seasons is projected in western Botswana and South Africa (Fig. 4.5a), particularly toward the end of the present century. In this subregion, the drying is stronger in the twenty-second century (not shown).

Apart from the late onset and early cessation signals (Fig. 4.3), internal decadal variability of rainfall in southern Africa remains large and is likely to mask any systematic changes in the total rainfall up to at least 2050.

#### 4.4 *Projected changes in atmospheric large-scale features*

Given the statistical significance of the projected precipitation changes presented in foregoing sections, an important question is whether associated atmospheric anomalies can be identified. Previous studies have reported on atmospheric (Mulenga et al., 2003) and oceanic anomalies (e.g., Rocha and Simmonds, 1997a) associated with southern African precipitation anomalies. Motivated by these findings, we expect that atmospheric adjustments to perturbed radiative forcing will set up anomalous circulation, hence precipitation, patterns.

In a vast majority of studies, sea surface temperature (SST) anomalies in the tropical oceans (remote and adjacent) have been blamed for southern African seasonal rainfall anomalies by generally locking atmospheric flow patterns into particular regimes (Rocha and Simmonds, 1997b; Cook, 2000a). SST anomalies in the subtropical oceans are also very important for southern Africa (Reason and Mulenga, 1999; Behera and Yamagata, 2001; Reason, 2002). However, the correlation of African rainfall with SST is less than 0.4 almost everywhere, implying that a large percentage of rainfall variance is due to other sources. There is growing evidence that the land surface can also exert an influence (opposing or reinforcing), mainly through feedback mechanisms (Douville et al., 2000; Douville, 2000a; Cook et al., 2006).



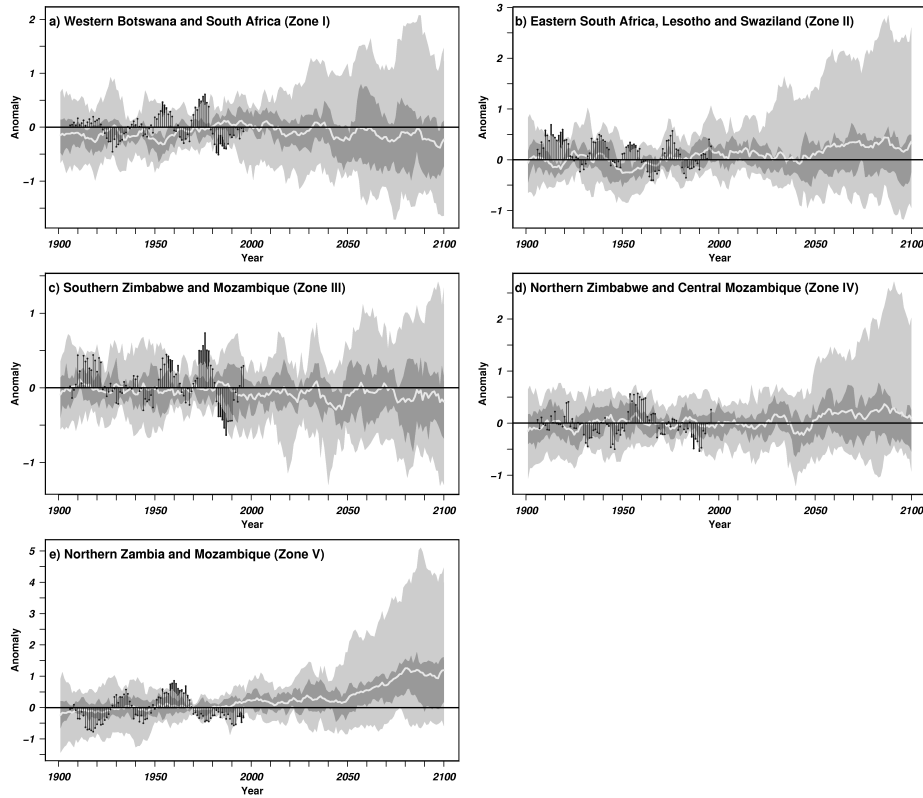


Fig. 4.5: Southern Africa 10-yr running mean filtered DJF precipitation anomalies (standard deviations;  $\sigma$ ), based on the 1961–1990 observed and individual model climatologies. The series spans the 1901–2100 period. Vertical lines terminated by circles show the observed twentieth-century anomalies calculated from CRU datasets. The white line shows the multimodel ensemble mean simulation, with the darker and lighter grey shadings indicating 50% ( $[q_{0.25}, q_{0.75}]$ ) and 95% ( $[q_{0.025}, q_{0.975}]$ ) of the distribution, respectively.

We postulate that the climate change signal will be communicated to the precipitation field through other components of the climate system (e.g., the ocean or land surface) and/or through an alteration in spatial structure and strength of atmospheric circulation regimes. These would in turn influence atmospheric moisture characteristics. Our hypothesis therefore is that future climate shifts will resemble interannual and decadal variability. On these premises, model results of flow patterns that would potentially influence rainfall anomalies in southern Africa are discussed. Smaller samples than in the foregoing sections are dictated by availability and/or quality of reanalysis fields used to make comparisons with model output. For daily model output, only shorter time slices (of about 20 years) are available on the PCMDI archive.

#### 4.4.1 Future moisture characteristics in spring

The reduction in spring precipitation is indicative of a delay in the rainfall onset over almost the entire southern African region. A trend toward a later onset has been found in the late twentieth century over parts of southern Africa (Tadross et al., 2005). Our results show that these decreases are likely to continue in the future climate (2051–2200). We have shown here that an early cessation is likely in many parts of the study region. Motivated by the spatial coherence in the simulated changes, and by similar reasons as Tadross et al. (2005), the focus will be placed only on the SON season.

SON lower-tropospheric (below 500-mb pressure level) horizontal moisture flux anomalies,  $\mathbf{Q}'$ , across southern Africa and the adjacent oceans have been calculated using daily CGCM simulations of specific humidity and the wind vector. This quantity is defined as

$$\mathbf{Q}' = \frac{1}{g} \int_{p_t}^{p_b} \langle q\mathbf{V} \rangle_f - \langle q\mathbf{V} \rangle_c dp, \quad (4.2)$$

where  $g$  is acceleration due to gravity,  $q$  is specific humidity, and  $\mathbf{V}$  the wind vector. The integral is taken from the 1000-mb ( $p_b$ ) to the 500-mb ( $p_t$ ) pressure level. Angle brackets denote the time mean for future ( $f$ ) and current ( $c$ ) climate, here defined as the 1961–80 period. Positive SON precipitation anomalies (implying an early onset) occur more frequently around the latter years of the 1961–80 period, consistent with Tadross et al. (2005). Using this reference period should give an insight on the likely change in water vapor transport across southern Africa. We also compute anomalous moisture divergence, that is,  $\nabla \cdot \mathbf{Q}'$ .

Composite moisture transport fields for the driest minus wettest SON seasons are computed for each CGCM 1961–2000 simulation and displayed in the first column of Fig. 4.6. A dry (wet) season is defined whenever the amplitude of the first prin-

cipal component standardized time score is less than (exceeds) one standard deviation. The composites are compared with the future (2046–65 and 2081–2100) moisture flux anomalies (second and third column of Fig. 4.6, respectively).

Evident in the composites are strong anomalous fluxes whereby moisture transported along the trades from the west Indian Ocean (north of  $\sim 20^\circ$  S) is diverted north toward East Africa or is divergent (gray shading). To the south, the climatological onshore moisture transport is weakened or reversed. The CGCM dry anomalies are broadly similar with those computed from National Centers for Environmental Prediction-National Center for Atmospheric Research (NCEP-NCAR) reanalysis fields (not shown).

A selection of projected moisture flux anomalies is displayed in the last two columns of Fig. 4.6. The results from other models are broadly similar. A pattern of anomalous moisture divergence is found over a large part of the study region in most models. Furthermore, the anomaly patterns are characterized by well-organized anticyclonic anomalies over much of southeastern Africa. Strong anomalous northwesterly moisture fluxes are found over the southwestern flank of the subtropical Indian Ocean anticyclone. This is indicative of a substantial weakening of moisture advection from the Indian Ocean into the subcontinent along the southeastern coast in future austral spring seasons, consistent with reduced precipitation. Westerlies from the southeast Atlantic are known to be cold and dry (due to cold waters and less evaporation; Mulenga et al., 2003). These are similar to the ones in the first column, showing that, indeed, the patterns of climate change resemble those of interannual and decadal variability in this respect.

It is quite likely that lower-tropospheric westerly anomalies along the southern latitudes in the models are dynamically coupled to a significant strengthening and equatorward expansion of the climatological upper-tropospheric westerlies associated with the Southern Hemisphere subtropical jet (SHSTJ). A striking similarity in the pattern of change in strength and latitudinal extent of the spring SHSTJ across the models used here has been found (not shown). Our results show that the boundary of the climatological westerly flux is likely to shift equatorward in future springs. In the western Indian Ocean north of  $\sim 10^\circ$  S, the easterly monsoonal circulation carrying moisture gains a southerly component that diverts moisture into East Africa close to the equator. These are similar to the ones in the first column, showing that climate change patterns resemble those of interannual and decadal variability. From this one may draw two conclusions: First, dry spring seasons in the models (and in observations) are unambiguously generated by weaker lower-tropospheric moisture transport inland. Second, large-scale circulation changes, whereby moisture influx into southern Africa is substantially reduced (i.e., a decrease in moisture flux convergence), are a possible cause for the late rainfall onset in the future.

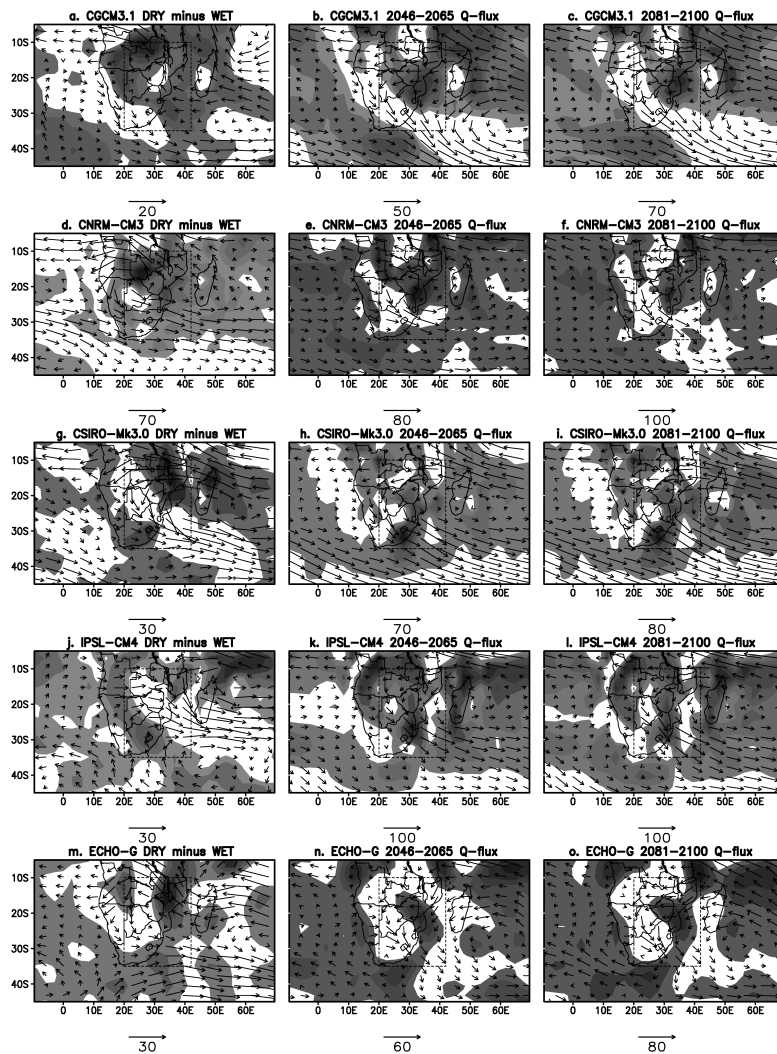


Fig. 4.6: SON lower-tropospheric horizontal moisture flux anomalies ( $\text{kg m}^{-1} \text{s}^{-1}$ ). For each model (name given in the title), the first column displays composites of the driest minus wettest SON seasons during the 1961–2000 period. The middle and right columns show the 2046–2065 and 2081–2100 moisture flux anomalies with respect to the 1961–1980 period. Areas of anomalous moisture divergence are shaded gray. Southern Africa (Fig. 4.1) is the land area in the dashed rectangular box.

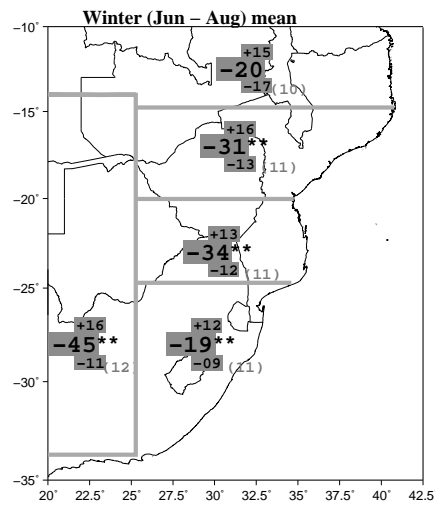


Fig. 4.7: Same as Fig. 4.3 but for austral winter (Jun–Aug) mean precipitation rates.

Surface and boundary layer processes would be another potential forcing mechanism for delayed rainfall onset. Evidence in support of drier winters in southern Africa in the future climate is presented in Fig. 4.7, consistent with previous findings (IPCC, 2007). Everywhere in the southern African domain, a statistically significant (at the 1% level everywhere but 5% level to the north) reduction in winter precipitation is simulated. The mean reduction in winter precipitation ranges from just under 20% to ~45%. Based on these projections, the delay in rainfall onset could in part be attributable to a drier land surface from the previous winter. Preseason anomalously wet soils have been identified to be a precursor to early seasonal rainfall onset (Reason et al., 2005). Reduced local evaporation and weaker lower-tropospheric moisture advection would possibly work in concert to delay the rainfall onset in southern Africa. However, moisture advection is a more significant source over most of southern Africa in spring as recycling ratios have been found to be low (Trenberth, 1999). We note that a negative feedback mechanism whereby wetter soils would result in a concurrent net reduction in summer precipitation over southern Africa has been presented (Cook et al., 2006). A similar argument (negative feedback) whereby reduced local moisture recycling led to enhanced moisture advection and precipitation in some parts of southern Africa has been presented for the summer (November–February) 1998/99 season (New et al., 2003).

#### 4.4.2 *The tropical-temperate trough (TTT) system*

A seasonal northwest-southeast-oriented cloud band across southern Africa, stretching from the southeast Atlantic to the southwest Indian Ocean, has been identified as the major rainfall-bearing system during austral summer months (Kuhnel, 1989). This feature, associated with a tropical-temperate trough (TTT) coupling system (Washington and Todd, 1999), links tropical convection to midlatitude transient eddies and provides a mechanism for energy and moisture transport across the southern African middle troposphere (Todd et al., 2004). Owing to the important implications for southern Africa summer precipitation, using the daily model precipitation simulations for the 2046–65 and 2081–2100 time slices, the likely behavior of this system is investigated.

The principal spatial mode of southern African DJF precipitation variability in the model simulations is identified from their empirical orthogonal functions (EOFs) (van den Dool, 2007). The correlation matrix forms input into the EOF analysis. Consistent with Washington and Todd (1999), the spatial modes, while broadly similar in each summer month, are not identical. In the interest of brevity, we present the results for the leading January (center of the principal rainy season) unrotated EOFs and for a selection of models. Varimax-rotated EOFs have also been calculated. However, contrary to what one would expect from Buel patterns, the unrotated EOFs do not show uniform centered loadings of the same sign.

The first EOF loadings, expressed as the correlation ( $\times 100$ ) between their coefficient time series and the CGCM time series for each grid, are shown in Fig. 4.8. The EOF spatial fields are characterized by a northwest-southeast orientated dipole or tripole pattern. Evident in the spatial fields are loadings of opposite signs between locations south of the latitudinal band about  $15^\circ \text{S}$ – $20^\circ \text{S}$ , and those farther north and the southwest Indian Ocean. As expected, intermodel differences in the spatial extent and magnitudes of the EOF weights exist. Notwithstanding, the spatial patterns of simulated rainfall variability are broadly similar to those found in observations and coincide with preferred locations of the TTT (Washington and Todd, 1999). The location of TTT, related to the south Indian Ocean convergence zone (SICZ), has been found to respond to ENSO-related SST anomalies (Cook, 2000b), particularly to west Indian Ocean SST forcing (Goddard and Graham, 1999). The presence of this pattern of rainfall variability in the CGCM simulations suggests that the climate change signal might propagate into southern African precipitation through similar pathways as those communicating the interannual variability forcing.

Having realized that the models adequately capture the major rain-bearing system across southern Africa, the most relevant question for the present study is how frequent and persistent would the TTT be over the band of preferred locations? This would attempt to explain the dipole response in mean and extreme DJF precipi-

tation (cf. Fig. 4.4) between the southwestern and northern areas of the domain (zones I and V, respectively). We endeavor to answer this question using the first EOF temporal coefficients displayed in Fig. 4.9. Positive standardized scores are indicative of periods when the TTT relocates northeastward (positive EOF weights in Fig. 4.8), and vice versa for negative scores (i.e., south-westward relocation). In a majority of cases, within each given January, the TTT propagates from the western pole northeastward into the southwest Indian Ocean. In a number of cases, the tropical-temperate rainband maintains its eastern locations throughout the month and in consecutive years. The presence of low frequency variability notwithstanding, there are indications for a higher frequency of positive scores in the Meteorological Research Institute (MRI) Coupled General Circulation Model, version 2.3.2 (CGCM2.3.2a) and Geophysical Fluid Dynamics Laboratory (GFDL) Climate Model version 2.1 (CM2.1) CGCMs (histograms not shown). However, the absence of a notably higher frequency in the other models inhibits us from drawing firm conclusions from our analysis.

#### 4.5 Discussion and conclusions

The present study uses monthly data from the CMIP3 multimodel dataset to estimate likely changes in southern Africa precipitation. We have chosen model projections driven by the intermediate SRES A1b scenario, a standard emission scenario in which no drastic reduction of CO<sub>2</sub> emissions up to 2100 exists, after which the levels stay constant. This scenario has been chosen because it is realistic and offers 100 or 200 years of integrations with constant greenhouse gas levels at twice the preindustrial values. Based on the model projections, we have been able to estimate the likely change in intensity of mean and extreme precipitation at much smaller spatial scales than in previous studies. Within southern Africa, spatial inhomogeneities in the projected changes exist. The inhomogeneities are explained by the highly variable local forcing, modulating the large-scale signal. This is despite the fact that accurate representation of land surface features in the low-resolution models used here has not been achieved yet.

The uncertainty associated with these projections has been presented. Regions where and periods during which the modeled changes in precipitation show notable similarities between the GCMs have been identified, as well as regions where (and seasons when) marked differences are found. The similarity and spatial coherence of the modeled response to enhanced greenhouse gas forcing suggest a realistic and robust climate change signal. On the other hand, uncertainties characterize those regions where divergences in the modeled precipitation response are found as well as where systematic biases in the modeled twentieth-century climate exist. Such cases manifest in the form of a wide range of the projected

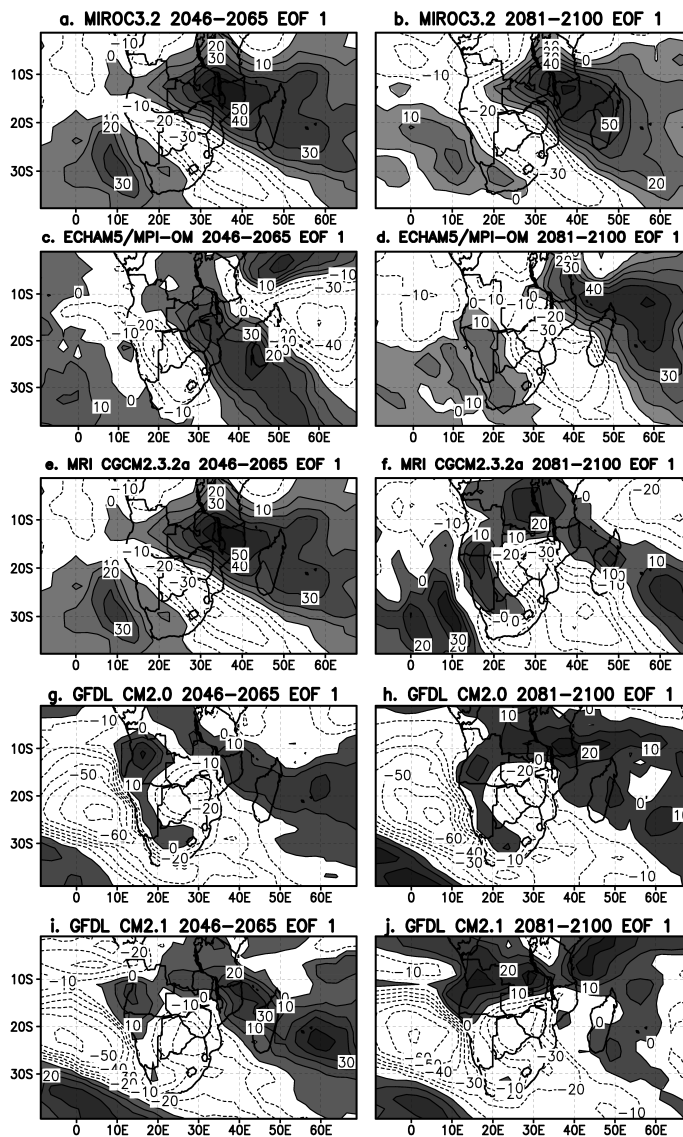


Fig. 4.8: January CGCM simulated precipitation EOF weights for the leading mode. For each model (name given in the title), the EOF weights for the 2046–2065 and 2081–2100 January precipitation are given in the first and second columns, respectively.



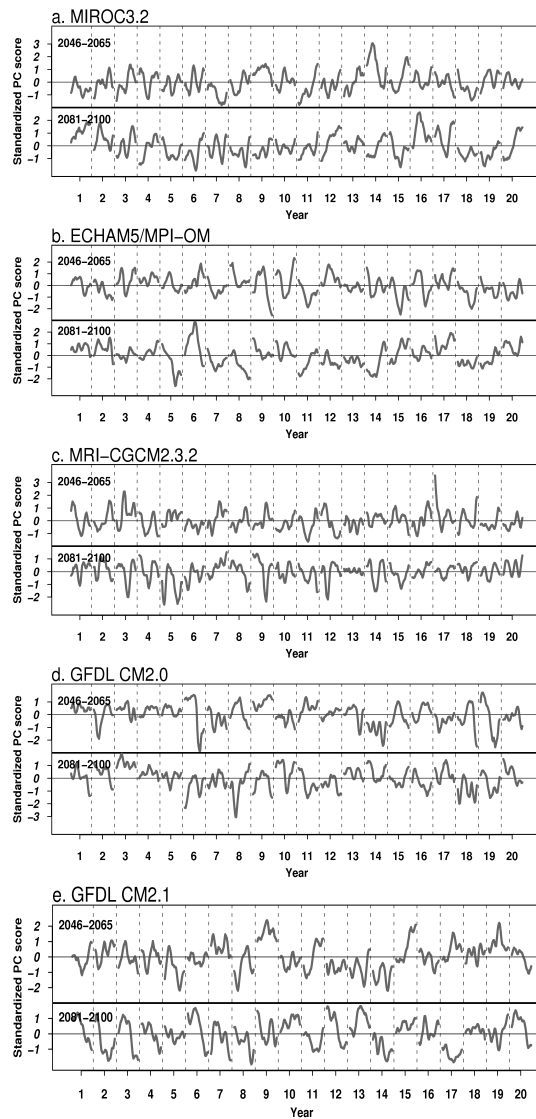


Fig. 4.9: Standardized principal component scores for each model simulated January daily precipitation. Each figure displays the 5-day running mean filtered scores for the 2046–2065 (top row) and 2081–2100 (bottom row) time slice.

changes.

A delay in rainy season onset has been found in southern Africa. We have identified two factors that are likely to contribute to this: First, a reduction in moisture influx into southern Africa. We have shown here that projected patterns of moisture transport are anomalously divergent over much of southern Africa. To the north flank of the south Indian Ocean anticyclone moisture is transported northwestward into East Africa. Over the southeastern parts, a reduction in moisture flux from the southwest Indian Ocean is found. Climate features forcing the large-scale circulation, and hence water vapor transport changes, deserve further research attention. Second, pre-season soil moisture deficits resulting in reduced local evaporation. Despite the low spring moisture recycling found in observations and modeling results showing a negative feedback from the land surface (soil moisture anomalies) in summer, drier soils would potentially reinforce lack of moisture for precipitation in future austral spring seasons.

In many parts of southern Africa, an early cessation of the rainy season is found. Possible causes of the earlier withdrawal of seasonal rains have not been investigated in this paper. This is a subject for future research. Our results point to a possible contraction in the rainfall season in locations south of about 15° S. To the north, the rainy season is projected to shift to later months (i.e., a late start and a delayed cessation).

Mean summer precipitation rates are projected to decrease near the hyperarid and semiarid areas of southern Africa (zone I). Over these areas, the severity of future droughts is projected to increase. North of about 15° S, mean summer precipitation is projected to increase. Although no causal relationship is implied, more frequent west Indian Ocean positioned tropical-temperate cloud bands are consistent with a reduction in summer precipitation rates and more severe droughts to the southwest.

Wet events are projected to become more intense to the north and southeast. To the north, this is consistent with more prolonged wet spells from persistent convective activity related to the TTT. The increase in the intensity of wettest events to the southeast is in qualitative agreement with Hewitson and Crane (2006). These increases in wet extremes may exacerbate the rise in reported flood disasters in the region. We note, however, that future projections of wettest events are less trustworthy owing to the inability to accurately simulate small-scale disturbances such as west Indian Ocean tropical cyclone activity in most models.

In general, the pattern of summer precipitation change, in particular coupled with increasing temperatures, may result in an eastward extension of desert areas in southern Africa, water scarcity, reduced agricultural productivity, and increased risks of food insecurity and famine. Not only is desertification a potential impact of global warming in southern Africa, but shorter growing seasons are possible

consequences in a large area.

## 5. PROJECTED CHANGES IN MEAN AND EXTREME PRECIPITATION IN AFRICA UNDER GLOBAL WARMING. PART II: EAST AFRICA

Probable changes in mean and extreme precipitation in East Africa are estimated from global climate models (GCMs) prepared for the IPCC Fourth Assessment Report (AR4). Bayesian statistics are used to derive the relative weights assigned to each member in the multi-model ensemble. There is substantial evidence in support of a positive shift of the whole rainfall distribution in East Africa during the wet seasons. The models give indications for an increase in mean precipitation rates and intensity of high rainfall events, but less severe droughts. Upward precipitation trends are projected from early this (twenty-first) century.

As in the observations, a statistically significant link between sea-surface temperature (SST) gradients in the tropical Indian Ocean and short-rains (October–December) in East Africa is simulated in the GCMs. Furthermore, most models project a differential warming of the Indian Ocean during boreal autumn. This is favourable for an increase in the probability of positive Indian Ocean zonal mode (IOZM) events, which have been associated with anomalously strong short-rains in East Africa.

On top of the general increase in rainfall in the tropics due to thermodynamic effects, a change in the structure of the Eastern Hemisphere Walker circulation is consistent with an increase in East Africa precipitation relative to other regions within the same latitudinal belt. A notable feature of this change is a weakening of the climatological subsidence over eastern Kenya.

East Africa is shown to be a region in which a coherent projection of future precipitation change can be made, supported by physical arguments. Although the rate of change is still uncertain, almost all results point to a wetter climate with more intense wet seasons and less severe droughts.

---

This chapter is based on the article “Projected changes in mean and extreme precipitation in Africa under global warming. Part II: East Africa” by Mxolisi E. Shongwe, Geert Jan van Oldenborgh, Bart J. J. M. van den Hurk, and Maarten K. van Aalst, 2008, submitted to *Journal of Climate*.

## 5.1 Introduction

The chemical composition of the atmosphere is changing due to human activities, triggering numerous studies aimed at understanding the sensitivity of the climate system to rising greenhouse gas concentrations (Houghton et al., 2001; IPCC, 2007, and references therein). Although the increase in greenhouse gases is relatively uniform around the globe, the response in a myriad of climate variables inevitably exhibits spatial inhomogeneities. For this reason, many studies have focused on possible impacts of climate change on selected climate variables in specific regions of the globe, especially those variables considered economically and socially significant (e.g., Gillett et al., 2004a; Karoly and Braganza, 2005; Hegerl et al., 2006; van Ulden and van Oldenborgh, 2006; van den Hurk et al., 2006; Beniston et al., 2007).

Considerable effort has been devoted to investigating possible changes in mean climate, and increasingly also to changes in variability and extremes, in the Northern Hemisphere continental areas. This is related to the availability of expertise and reliable data in these areas. By comparison, many of the least developed countries, especially in Africa, suffer from both a lack of high-quality data and lack of research attention and capacity. Hence, there are far fewer climate analyses for these regions, especially in relation to variability and extremes. Impact analyses show that such variability and extremes disproportionately affect the poorest countries and the poorest people (e.g. African Development Bank (AfDB) et al., 2003). Trying to address that gap, Chapter 4 (hereafter SHO09) presents an analysis of projected precipitation changes for southern Africa. In this paper, a similar approach is applied to East Africa, defined as the area lying between  $10^{\circ}$  S– $4^{\circ}$  N,  $28^{\circ}$ – $42^{\circ}$  E. The region experiences a semi-annual rainfall cycle with two major rainfall peaks in boreal spring [March–May (MAM); also known as long-rains] and autumn [September–December (SOND); also known as the short-rains]. During the latter season (short-rains), atmospheric dynamics in the first month (September) differ from the rest of the season (October–December). Also, teleconnections with large-scale features such as the El-Niño/Southern-Oscillation (ENSO) are different between September and OND (Mutai and Ward, 2000). It is common practice therefore to omit September when referring to the short-rains in East Africa (e.g. Clark et al., 2003; Anyah and Semazzi, 2007). We adopt the same convention in this paper. Some portion of the selected area has one rainfall maximum during boreal winter–spring months (November–April).

Traditionally, climate change studies in which Africa features have tended to focus on likely precipitation changes during boreal summer and winter (IPCC, 2007). Much less is known about the transition seasons (i.e. boreal autumn and spring), which are the rainy seasons in East Africa. Furthermore, there has been a tendency to focus at large regions within Africa or in some cases on the Giorgi regions

(Giorgi and Francisco, 2000). While this approach is useful in diagnosing the climate change signal on rainfall as a first step, it tends to overlook the effect of local features such as East Africa's varied topography (e.g. mountain ranges and rift valleys) and large water bodies (e.g. Lake Victoria) on the large scale signal. Although most of these local controls are not yet adequately represented in low-resolution climate models such as those used here, the homogenous subregions identified by Indeje et al. (2000) are used to show that rainfall response to global warming is not uniform across the region.

In recent years, East Africa has suffered frequent episodes of both excessive (e.g. Webster et al., 1999; Latif et al., 1999) and deficient rainfall (e.g. Hastenrath et al., 2007). In particular, the frequency of anomalously strong rainfall causing floods has increased. Our analysis of data from the International Disaster Database EM-DAT (<http://www.em-dat.net/>), reveals that there has also been an increase in the number of reported hydrometeorological disasters in the region, from an average of less than 3 events/year in the 1980s, to over 7 events/year in the 1990s, and almost 10 events/year from 2000 to 2006, with a particular increase in floods: from an average of less than 1 event/year in the 1980s to 7 events/year between 2000 and 2006. In the period 2000–2006, these hydrometeorological disasters affected on average almost two million people per year. In addition, they have severe impacts on economic performance and poverty alleviation (e.g., Hellmuth et al., 2007).

Furthermore, we note that many of the region's epidemics, which dominate the remainder of the reported disasters in the EM-DAT database, are also affected by climatic conditions. While part of the trend is due to better reporting, it also reflects a rising vulnerability to natural hazards, and potentially an underlying trend in climate variability and extremes. These rising risks are receiving increasing attention from policy makers, for example, in the Decision and Declaration on Climate Change and Development adopted by the African Union Head of State Summit in January 2007, and in new efforts by East African governments to better manage climate risks. In Kenya for instance, the Kenya Adaptation to Climate Change in Arid Lands (KACCAL) project aims to address the increasing risk of both floods and droughts (World Bank, 2006).

In this context, there is an obvious need for better analyses of the likely response of extreme climate events in this region to global warming, to inform disaster preparedness and development planning. Such demands provided the motivation for the present study. The primary aim is to assess how the intensity of seasonal precipitation extremes is likely to change in the region, against the backdrop of probable changes in mean precipitation. A secondary aim is to assess the spatial inhomogeneities in the model projections. We also present physical mechanisms that may explain the simulated changes in the precipitation probability distribu-

tion.

## 5.2 Data and Methods

### 5.2.1 Model simulations and observations

A brief description of the datasets used and the analysis methods applied are given below. Further details can be found in SHO09. The models used in the Intergovernmental Panel on Climate Change (IPCC) Fourth Assessment Report (AR4; IPCC, 2007) form the major input to the analysis of changes in precipitation patterns. From these models, the output of which has been made available as part of the World Climate Research Program (WCRP) Coupled Model Intercomparison Project Phase 3 (CMIP3) datasets, a subset consisting of 12 coupled general circulation model (CGCM) simulations has been selected. We have chosen model projections driven by the intermediate SRES A1B scenario, a standard emission scenario currently roughly corresponding to observed CO<sub>2</sub> concentrations. In this scenario, there is no drastic reduction of CO<sub>2</sub> emissions up to 2100, when concentrations reach twice their pre-industrial levels. After 2100, experiments have been continued with constant CO<sub>2</sub> concentrations at this level.

Compared to the Climate Research Unit (CRU TS2.1; New et al., 2000) gridded precipitation, the 12 selected CGCMs had the highest correlation and smallest root-mean-squared-error (RMSE) over much of sub-Saharan Africa. Results from the CGCM selection process are relevant for this larger domain (sub-Saharan Africa). For this reason, they are not included in this study, which focuses on a smaller sub-domain. The selected CGCMs, their spatial resolutions, ensemble sizes and references are given in Table 1 of SHO09. The model simulations are linearly interpolated to a common  $1.25^\circ \times \sim 1.24^\circ$  lat/lon grid, corresponding roughly to T95 resolution. As in SHO09, two subsamples have been selected from the model simulations. The 1901–2000 and 2051–2200 periods define the present (20c3m) and future climate, respectively.

In addition to monthly CMIP3 precipitation, the horizontal wind vector and pressure vertical velocity ( $\omega$ ) fields are used. These variables are used to estimate the strength and structure of the Eastern Hemisphere zonal (Walker) circulation and their projected changes. Three of the models\* used in the precipitation change analysis have been omitted in the analysis of the zonal circulation. The CGCM background Walker circulation is compared with that obtained from the Euro-

---

\* The ECHO-G model has been omitted because horizontal wind and pressure velocity fields are not available on the IPCC-AR4 archive in both their 20c3m and SRESA1b runs. For the CSIRO Mk3.0, the vertical velocity fields are not available. For the UKMO HadCM3, SRESA1b horizontal wind and vertical velocity fields are not available.

pean Centre for Medium-Range Weather Forecasts (ECMWF) 40-year Reanalysis (ERA40; Uppala et al., 2005).

Observed twentieth century precipitation used in this study was taken from the CRU TS2.1 gridded station data. Unlike in SHO09, dearth of station observations in the Global Historical Climatology Network (GHCN) data precluded delineating homogenous rainfall zones. For this reason, the climate zones defined by Indeje et al. (2000) have been adopted in this study. These zones are shown in Fig. 5.1. The western zones of Indeje et al. (2000) are combined into one zone (Zone III; Fig. 5.1) to allow a larger spatial sampling. In most models used here, precipitation in these areas have a similar probability density functions (PDFs; not shown). The CRU TS2.1 grid points falling within each zone are averaged. All the zones except much of Tanzania (Zone IV) have a semi-annual cycle. In Zone IV, the annual cycle of area-averaged precipitation showed a peak during austral summer-autumn months (November–April). The CMIP3 simulated precipitation is spatially averaged analogous to the CRU TS2.1 data. The coastal region, the central region of Kenya and the Lake Victoria area are small to be adequately resolved by some low-resolution CGCMs. These regions have therefore been omitted in the analysis. Monthly precipitation from the CRU TS2.1 gridded station and CMIP3 data are accumulated into seasonal totals for each rainfall season of East Africa. Mean precipitation rates ( $\text{mm day}^{-1}$ ) in a given season are calculated by dividing the seasonal totals by the number of days within that season. Climatologically wettest seasons are defined as those with the highest mean precipitation rates. On the other hand, driest seasons, characterizing meteorological droughts, have the lowest mean precipitation rates.

### 5.2.2 Extreme value analysis

The peak over threshold or Generalised Pareto Distribution (GPD) is used in this study to represent the distribution of observed and simulated extreme seasonal precipitation rates. A description of GPD and its applications is found in Coles (2001). The quality of the GPD fit is then assessed using Anderson-Darling goodness-of-fit tests (Laio, 2004). Details of how the GPD has been applied in our work including statistical tests is discussed by SHO09.

Return levels are estimated from the fitted GPD. Return levels are frequently used in extreme precipitation studies in climate research (e.g., Kharin and Zwiers, 2000; Meehl et al., 2005; Kharin et al., 2007) because of the simplicity of their interpretation. The return level ( $z_p$ ) is the threshold likely to be exceeded in a given year with probability  $p$ , or the level likely to be exceeded once in every  $1/p$  years. In this study 10-, 20-, 50- and 100-year return levels have been estimated. The return values are computed for each homogenous zone (Fig. 5.1) in both the OND and MAM seasons. Owing to the small sample size of threshold excesses, only results



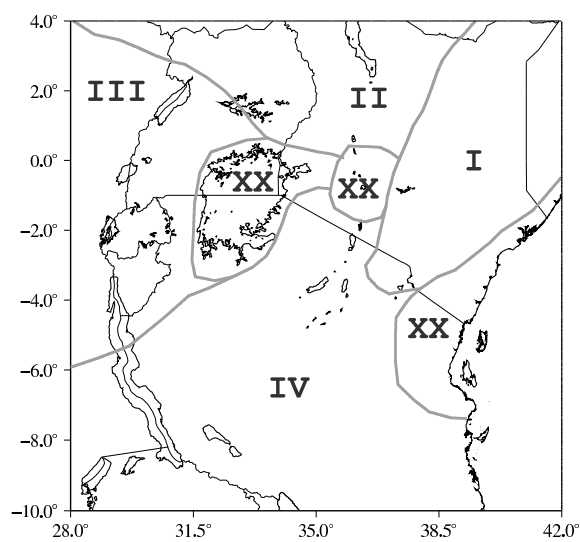


*Fig. 5.1:* Location map of East Africa's climatic zones adopted from Indeje et al. (2000). Region III on the west is a combination of two of the Indeje et al. (2000) original zones. Regions that are not large enough to be adequately resolved by the lowest resolution AR4 CGCMs (shown by XX) have been omitted in our analyses.

based on the least biased 10-year return levels are presented in this paper. These GPD quantiles (10-year return levels) are obtained from an interpolation rather than an extrapolation. Results obtained using 100-year return levels are available on the KNMI Africa scenarios web-site ([http://www.knmi.nl/africa\\_scenarios/](http://www.knmi.nl/africa_scenarios/)). When modelling dry extremes following the approach discussed by SHO09, a problem is encountered during extrapolation to much longer return periods because these extremes are by definition constrained by zero above (i.e. dry extremes have a finite upper bound). However, mean precipitation rates during the driest seasons are typically greater than zero. Also, the results presented in this paper are based on shorter 10-year return levels, which are obtained through an interpolation rather than an extrapolation. The limitation imposed by the upper finite bound of dry extremes is therefore not a concern in this study.

### 5.2.3 Multi-model ensembling

Uncertainties are inherent in long-term climate model simulations. These can be attributed to natural climate variability, different model responses to a given forcing (such as increases in greenhouse gas concentration) and those associated with the emission scenarios used to force the climate models. In climate change studies devoted to precipitation extremes and their possible future changes, it has become common practice to use simulations from a range of climate models (e.g., Kharin et al., 2007). Research on how best to combine simulations from several climate models through objective weighting is ongoing (e.g. Giorgi and Mearns, 2002, 2003; Tebaldi et al., 2004, 2005).

Using Bayes theorem and making certain assumptions, it is possible to objectively assign weights to different climate models leading to a probability distribution of future climate change. These assumptions detailed by Tebaldi et al. (2005) relate to model bias, model independence and the similarity of physical mechanisms determining the unforced and future climate. This method has been adopted in the present study. We note here that equal weighting of the models yields similar results to the Bayesian weighing method used to obtain the results presented in Section 5.3. The Bayesian method offered an additional value by, amongst other things, downweighting obvious outliers.

For comprehensive details of this method, the reader is referred to Tebaldi et al. (2005). The Bayesian method requires that the input variables have Gaussian likelihoods. Mean precipitation taken over sufficiently long periods (100 or 150 years in this study) meet this requirement from the central limit theorem. To fulfill this requirement in the case of extreme quantiles, the first step involved estimating the GPD parameters from maximum likelihood. After checking for model quality and inverting the GPD to obtain the 10-year return levels, we then use the delta method described by Coles (2001) to estimate the uncertainty on the return

levels. Using a profile likelihood function (Coles, 2001) has been deemed unnecessary when estimating the shorter 10-year return levels. More details of the methodology used to obtain the GPD quantiles can be found in Appendix A.

To summarize, in the Bayesian framework used, the ratio of the conditional posterior mean of future climate ( $\nu$ ) to control climate ( $\mu$ ) simulations is used to define the relative precipitation change ( $\Delta P$ ) as

$$\Delta P = 100\left(\frac{\nu}{\mu} - 1\right). \quad (5.1)$$

For mean precipitation rates and 10-year wettest events,  $\Delta P > 0$  is indicative of an increase in their intensity. An increase in the severity of 10-year driest events is indicated by  $\Delta P < 0$ . As previously mentioned, these changes compare statistics computed using data for the 1901–2000 (present) period with their counterparts in the 2051–2200 (future) period.

### 5.3 Changes in mean and extreme precipitation

In the following sub-sections, we present the 95% confidence interval of  $\Delta P$  as obtained from the Bayesian method for each zone and rainy season of East Africa. We present the results on maps to allow a concise visual interpretation and an easy assessment of the spatial pattern of the projected changes. Statistical significance at the  $\alpha\%$  significance level (i.e.  $p < \alpha/100$ ) is found whenever the  $(100-\alpha)\%$  confidence interval of  $\Delta P$  excludes zero (i.e. the null hypothesis of no precipitation change). Statistical significance at the  $\alpha\%$  level is achieved whenever there is strong evidence from the Bayesian weighted model simulations in support of a  $(100-\alpha)\%$  chance that  $\Delta P$  falls on one side of the zero line although some models can still give projections of the opposite sign. Using this convention, changes that are statistically significant at the 5% level (1% level) are shaded gray (shown by two asterisks) in the maps.

#### 5.3.1 Short-rains season (October–December; OND)

Mean OND precipitation increases are simulated almost everywhere in East Africa (Fig. 5.2a). Over the semi-arid areas in northern Kenya (Zones I and II; Fig. 5.1), the western parts, which include Rwanda and Burundi (Zone III), mean precipitation is projected to increase by more than  $\sim 10\%$ . These increases achieve statistical significance at the 5% level almost everywhere, and are even significant at the 1% level to the north. Over much of Tanzania (Zone IV), the model projections provide evidence in support of an increase in precipitation rates during austral summer–autumn months (November–April). While most models show an

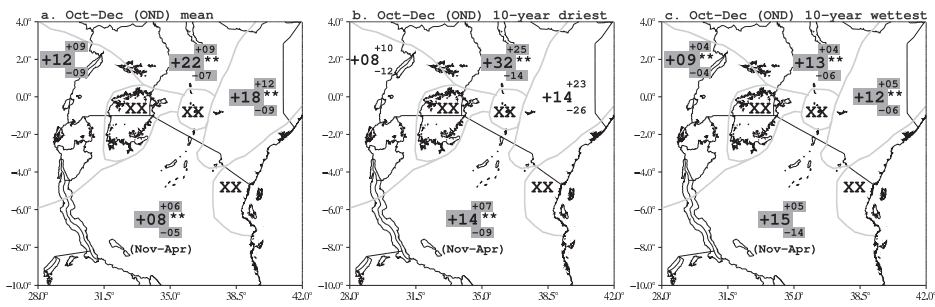


Fig. 5.2: Projected changes (%) in October–December (OND; short-rains) a) mean precipitation rates, b) 10-year driest events, and c) 10-year wettest events in each climatic zone. In much of Tanzania (Zone IV; Fig. 5.1), the displayed precipitation changes are for the austral summer–autumn (November–April) season. In each case, three values are plotted. The middle number gives the mean projected change preceded by its sign (+ve for increase and -ve for decrease). The number above (below) the mean change, preceded by a +ve (-ve) sign gives the distance to the upper (lower) critical value at the 5% level of significance. Projected changes that are significant at the 5% (1%) level are shaded in grey (shown by two asterisks).

increase in mean OND precipitation, the HadGEM1 model shows decreases in rainfall almost everywhere in the area. The convergence criterion used in the Bayesian weighting (Tebaldi et al., 2005) treats this model as an outlier and downweights it. A reduction of the severity of 10-year driest seasons are found over almost the entire East African region (Fig. 5.2b). The magnitudes of the simulated reduction in the severity of these OND dry extremes are comparable with those of the mean precipitation rates. Larger reductions ( $\sim 32\%$ ), significant at the 1% level, are found in northern Kenya and Uganda (Zone II). Elsewhere in the north, the projected lessening of 10-year droughts' severity is not statistically significant. Austral summer–autumn 10-year droughts are becoming less severe in much of Tanzania by about 14%.

In common with changes in the mean precipitation rates, widespread increases in the intensity of 10-year wettest OND seasons are simulated (Fig. 5.2c). Significant increases exceeding  $\geq 10\%$  are found in Kenya, Uganda and the western parts. In northeastern Democratic Republic of Congo (DRC) and much of Tanzania (Zone IV), increases in the 10-year wettest austral summer seasons average  $\sim 15\%$ .

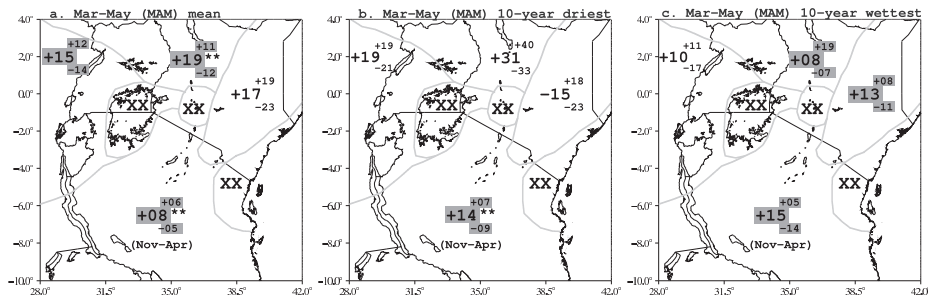


Fig. 5.3: Same as Fig. 5.2 but for the March–May (long-rains) season.

### 5.3.2 Long-rains season (March–May)

Changes in mean precipitation during the long-rains season (MAM) have generally the same sign and magnitudes as those simulated for the short-rains (Fig. 5.3a). The Bayesian weighted model simulations project more than  $\sim 15\%$  increase in mean precipitation rates over much of East Africa. The upper confidence limit exceeds  $\sim 25\%$  over a large area to the north and west. However, in contrast to the short-rains, the models perform poorly in simulating the twentieth century climate during this season. During the model pre-selection process, relative to the OND season, correlation between the monthly CRU and model simulated MAM precipitation was found to be low while the RMSE scores were found to be higher (not shown). The difficulty in modelling precipitation during the long-rains has been found in seasonal climate predictability studies, and is due to a dominance of internal atmospheric variations (not provably connected to other components of the climate system; Mutai et al., 1998). Despite the statistical significance in the simulated patterns of change, the uncertainty associated with these patterns is higher. The models show a reduction in the severity of 10-year droughts almost everywhere except over eastern Kenya (Fig. 5.3b). In eastern Kenya, where changes in dry and wet extremes have opposite signs, an increase in interannual rainfall variance is implied. Changes in 10-year wettest seasons are of the same sign as those of mean precipitation rates implying that floods are likely to become more intense (Fig. 5.3c). However, we place less emphasis on these projections owing to their lower reliability.

### 5.3.3 Time series analysis

Time series plots for East Africa precipitation during the twentieth (observed and simulated) and twenty-first centuries (simulated) and in each rainy season are

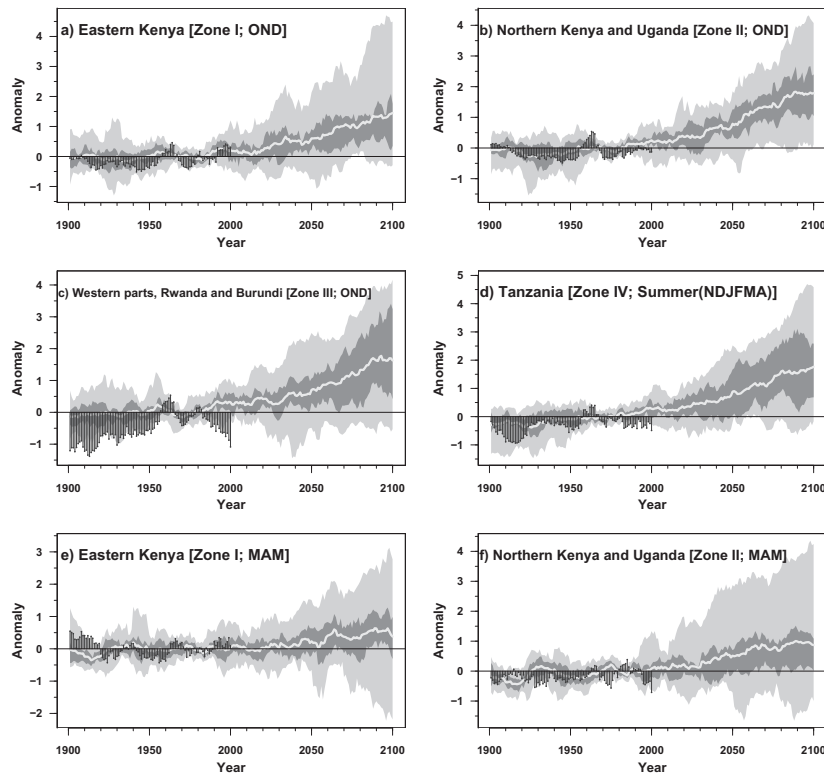


*Fig. 5.4:* Time series of observed and simulated precipitation anomalies (standard deviation;  $\sigma$ ) with reference to the 1961–1990 climatology. Panels a), b) and c) display the time-series for OND rainfall. Panel d) show the series for much of Tanzania (Zone IV; Fig. 5.1) during austral summer–autumn (November–April; NDJFMA), while the bottom two panels (e and f) display the series for MAM precipitation in eastern Kenya (Zone I), and northern Kenya and Uganda (Zone II), respectively. The black vertical lines terminated by circles display the observed twentieth century precipitation from CRU data. The white line show the ensemble average, with the darker grey shadings indicating 50% ( $[q_{0.25}, q_{0.75}]$ ) and 95% ( $[q_{0.025}, q_{0.975}]$ ) of the distribution, respectively.

shown in Fig. 5.4. Unlike in Figs. 5.2 and 5.3, where the CGCMs are subjected to a Bayesian weighting, the models are equally weighted in these plots. Despite the wider inter-model dispersion in their twenty-first century projections [caused mainly by the outlying HadGEM1 (dry) and MIROC3.2 (wet) CGCMs], there is substantial evidence in support of an increase in the amount of rainfall. The sharp precipitation increase in East Africa emerges from the early part of the twenty-first century and in most cases is a reversal of drier conditions experienced during much of last century. A trend toward predominantly positive precipitation anomalies is also present in the long-rains twenty-first century time series (Fig. 5.4e–f). However, the signal-to-noise ratio in these projections is low.

Noteworthy, the results from the Bayesian weighted and unweighted simulations are broadly similar. By down-weighting outlying CGCMs, the Bayesian procedure offered the additional value of reducing the model dispersion by about a factor two, particularly in the twenty-second century simulations when the model spread is largest.

#### 5.4 *Projected changes in large-scale forcing*

The robust climate change signal on East Africa precipitation presented above prompts us to endeavor to diagnose likely physical mechanisms and forcings. There is considerable consensus between observational, theoretical and modelling studies with regard to an increase in vertically-integrated atmospheric water vapour as the climate warms (Zveryaev and Chu, 2003; Trenberth et al., 2005; Zveryaev and Allan, 2005). Related to this is a robust projection of precipitation increase in the deep tropics, which has been detected in the current climate (Zhang et al., 2007). The zonal mean precipitation in the tropics increases because the  $7\%/^{\circ}\text{C}$  increase in precipitable water, which follows the Clausius-Clapeyron relationship, is not completely compensated by a slow-down of the tropical circulation (Held and Soden, 2006; Vecchi and Soden, 2007).

The increase in precipitation in the tropics is not zonally uniform, with East Africa precipitation projected to increase more than the zonal mean. These zonal asymmetries in tropical precipitation response to global warming suggest that other mechanisms also exert a significant influence. These partly stem from the atmospheric dynamic response, which is not zonally symmetric and leads to a horizontal redistribution of water vapor.

To understand this we turn to the well understood interannual variability in the region. Our hypothesis is that the climate change signal will be communicated to the rainfall field partly through the same factors which control interannual rainfall variability in the present climate. At interannual timescales, Hastenrath et al. (1993) discussed atmospheric forcing on the Indian Ocean hydrosphere. A num-

ber of papers documenting atmosphere-ocean coupling have appeared in literature (e.g. Webster et al., 1999; Saji et al., 1999; Goddard and Graham, 1999). It has been found that atmospheric anomalies of pressure and wind typically precede sea-surface temperature (SST) anomalies (Hastenrath and Polzin, 2005). Subsequent SST anomalies, in part forced by wind-stress anomalies, feed back to the atmosphere, further reinforcing atmospheric anomalies (Goddard and Graham, 1999), which often result in precipitation anomalies. Against this background, modelled changes in SST and atmospheric circulation during the short-rains season are examined in this section.

#### 5.4.1 *Projected OND Indian Ocean SST pattern and rainfall relationship*

Observational and modelling studies have linked East African high-frequency rainfall variability during boreal autumn to SST anomalies (Goddard and Graham, 1999; Black et al., 2003). Earlier studies aimed at understanding the link between East Africa precipitation and equatorial Pacific Ocean SSTs associated with the El Niño-Southern Oscillation (ENSO; e.g., Hastenrath et al., 1993; Indeje et al., 2000). It was found that ENSO exerts some influence on East Africa short-rains such that rainfall is enhanced (suppressed) during warm (cold) events in the eastern equatorial Pacific Ocean.

It has been shown that the Indian Ocean is one of the pathways through which the ENSO signal propagates into East Africa precipitation. Often, the west Indian Ocean warming lags that of the eastern equatorial Pacific by a few months (Klein et al., 1999). However, evidence has been presented supporting the existence of an Indian Ocean mode of SST variability independent of ENSO (Saji et al., 1999; Webster et al., 1999). In fact OND 1961, one of the wettest in the twentieth century, was not related to ENSO (figure not shown). The models used in this study do not give a robust signal with respect to changes in the mean state of ENSO (not shown). Based on these findings and the fact that changes in ENSO properties are unlikely to exceed natural variability (van Oldenborgh et al., 2005c), possible changes in Indian Ocean SST patterns are investigated in this paper. This is motivated by results from studies which found Indian Ocean SST anomalies to be the dominant factor controlling East Africa short-rains (Latif et al., 1999; Goddard and Graham, 1999; Black et al., 2003; Clark et al., 2003; Behera et al., 2005; Washington and Preston, 2006).

In this study, the 1901–2000 CGCM simulated East Africa short- and long-rains were subjected to a standard empirical orthogonal function (EOF) analysis (see e.g. van den Dool, 2007). The first EOFs are a monopole patterns describing the largest source of interannual variability in this region, particularly during the short-rains. The corresponding principal component series are then regressed on simultaneous Indian Ocean SSTs from each model. The regression of the first



principal components (PC 1) on Indian Ocean SSTs are displayed in the first and last columns of Fig. 5.5. Areas with significant regression at the 5% level (from a two-sided local *t*-test ) are shaded.

A statistically significant positive link is found with SSTs in the western tropical Indian Ocean (WTIO), west of  $\sim 80^\circ$  E in most models. In some models (e.g. CSIRO-Mk3.0, ECHAM5/MPI-OM, GFDL-CM2.0, GFDL-CM2.1 and ECHO-G) the ocean area with significant positive association with precipitation extends into the Bay of Bengal. Negative regression coefficients are found in the southeastern Indian Ocean off the coast of Sumatra in almost all models. The figures demonstrate that wetter conditions in East Africa in the CGCMs during boreal autumn often occur when SSTs are warmer in the western Indian Ocean and cooler close to the Maritime Continent. These results are broadly similar to previous findings on Indian Ocean–East Africa rainfall relationships in observational and modelling research work (Black et al., 2003; Clark et al., 2003). The major atmospheric response to the anomalous zonal SST gradients relevant for East Africa short-rains is a perturbed Indian Ocean Walker cell (Behera et al., 2005). Low-level easterly anomalies south and close to the equator are a prominent feature in this perturbed local Walker circulation. These moisture-laden winds feed the diabatic heating-induced anomalous convection close to the warm SST anomaly, with the obvious consequence of enhanced precipitation.

There is no similarly significant link between the long-rains (MAM) and simultaneous Indian Ocean SSTs in the models (last column of Fig. 5.5). Even in models which show some association (e.g. CNRM-CM3, MIROC3.2, ECHAM5/MPI-OM, ECHO-G and GFDL-CM2.0), the remarkable rainfall link to tropical Indian Ocean SST gradients found during the OND season is not present. We do not know of any documented external control (from other components of the climate system) for the long-rains interannual variability. For this reason, our discussion will focus on SST patterns likely to influence OND rainfall.

Having established the existence of the Indian Ocean SST signal on rainfall, the model simulated SST differences (2051–2200 minus 1901–2000) are examined. Boreal autumn (OND) Indian Ocean SST differences are displayed in the middle column of Fig. 5.5. Statistically significant (at the 1% level) basin-wide warming is found. Although SSTs warm throughout the tropical Indian Ocean basin, zonal asymmetries in the warming are evident in most models. The western part of the basin is generally projected to warm more than the eastern. These results are in qualitative agreement with Vecchi and Soden (2007) who show a tendency towards upwelling (downwelling) along the eastern (western) equatorial Indian Ocean in the twenty-first century (their Fig. 15).

A similar differential warming is observed in interannual variability. It stems from wind-evaporation-SST and wind-thermocline-SST feedbacks which cool the ocean

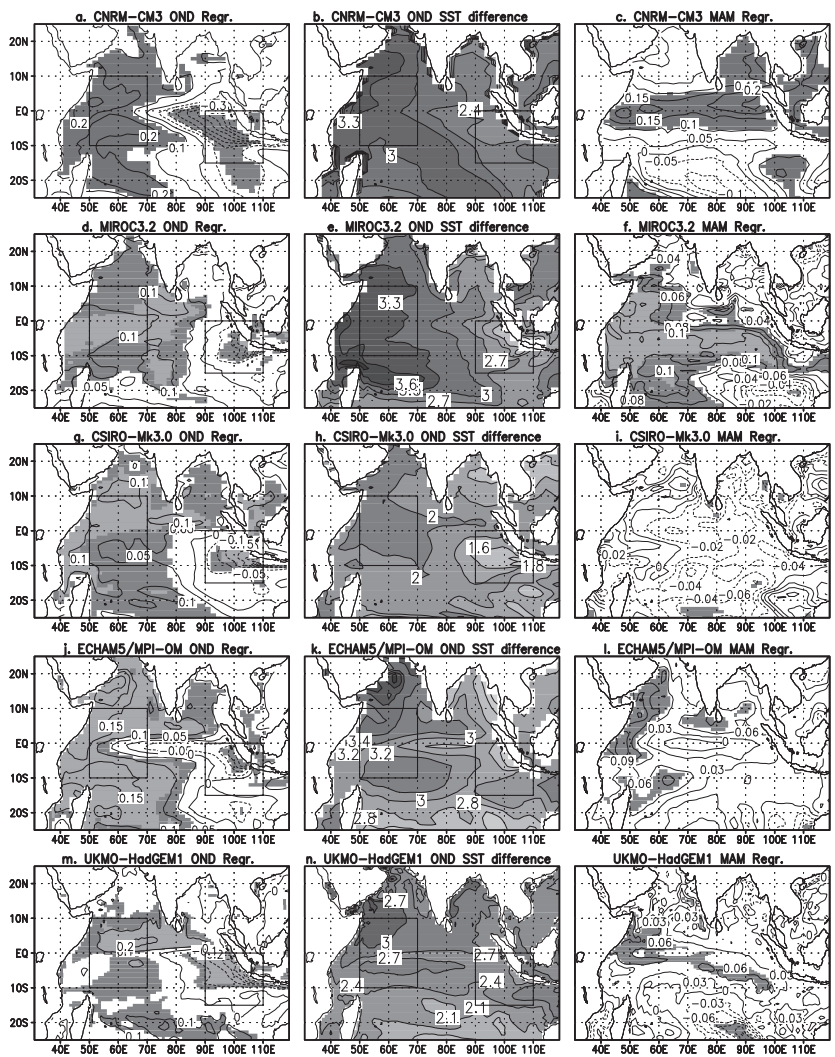


Fig. 5.5: Regression [+ve (solid lines) and -ve (dashed lines)] of model simulated 1901–2000 OND precipitation EOF 1 on simultaneous Indian Ocean SSTs (first column). For each model (name in the title), the second column displays the simulated OND SST difference (i.e. 2051–2200 minus 1901–2000; ° C). The third column shows the same statistics as column 1, but for MAM season. In each case, regression coefficients that are statistically significant at the 5% level are shaded grey. The rectangles show areas used to define the Indian Ocean Zonal Mode index (IOZMI).

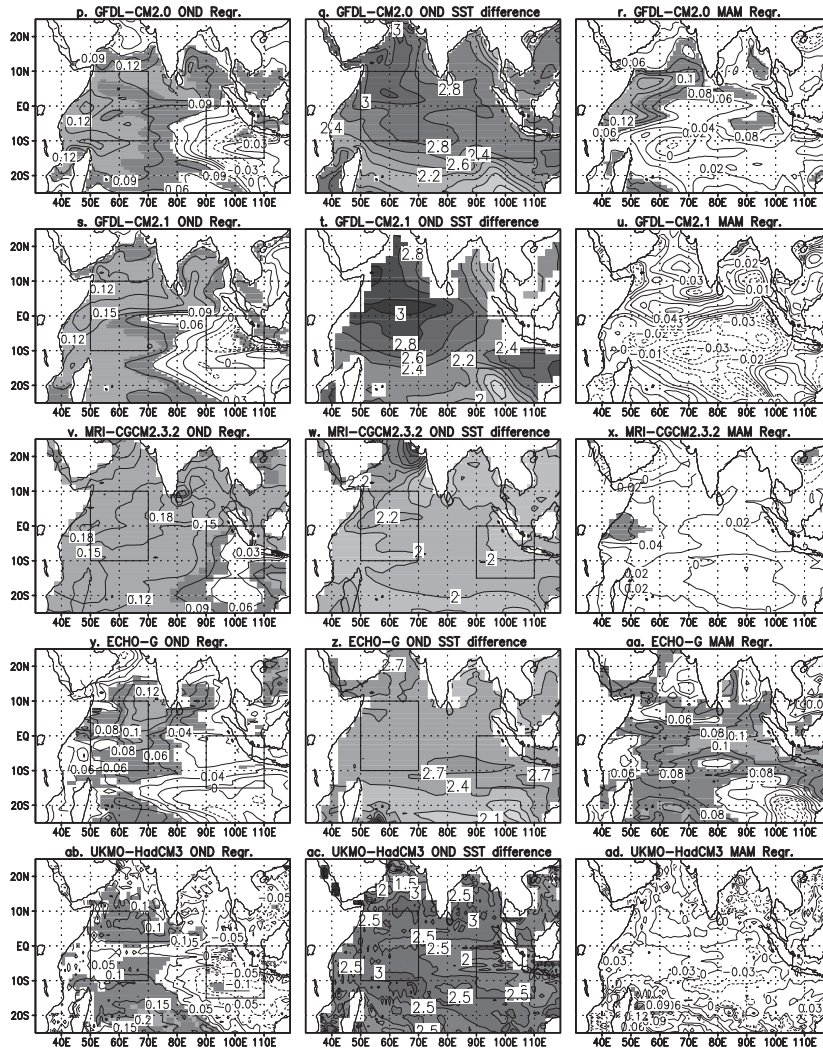


Fig. 5.5: continued...

surface in the south-east Indian Ocean (SEIO) from boreal summer to fall before giving way to basin wide warming from around December (Shinoda et al., 2004). Vecchi and Soden (2007) argue that atmospheric anomalies drive changes in tropical ocean dynamics, and hence the ocean thermal structure in the twenty-first century. The simulated differential warming and associated anomalous zonal SST gradients have implications for the east-west Indian SST dipole that occasionally peaks during boreal fall months (Behera et al., 2005). As demonstrated above, enhanced rainfall in East Africa is often associated with anomalously warm (cold) SSTs in the WTIO (SEIO).

We proceed by defining an index WTI expressed as average SST in the rectangular domain to the west ( $50^{\circ}$ – $70^{\circ}$  E,  $10^{\circ}$  N– $10^{\circ}$  S) and another index SEI for the box in the eastern extremity ( $90^{\circ}$ – $100^{\circ}$  E,  $0^{\circ}$ – $15^{\circ}$  S). The Indian Ocean zonal mode index (IOZMI), which represents zonal SST gradients across the near-equatorial Indian Ocean is then defined as  $IOZMI = WTI - SEI$ . These boxes are indicated in the first two columns of Figure 5.5.

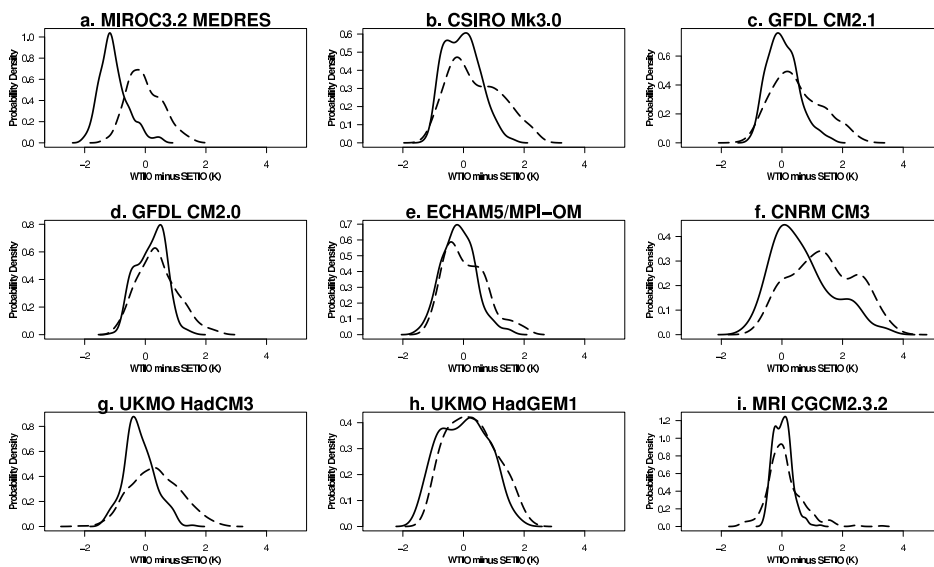


Fig. 5.6: Probability density functions (PDFs) of the IOZMI simulated by the selected CGCMs (name given in the title) in the twentieth century (solid line) and future climate (2051–2200; dashed line).

Probability density functions (PDFs) of IOZMI are shown in Fig. 5.6. Almost all the models displayed in the figure show a clear shift in the PDFs towards a higher probability of positive IOZMI phases. This enhanced probability translates to a

higher probability of excessive short-rains in East Africa in the future climate. These findings are consistent with the results presented in Section 5.3.1. On average, IOZM-shift contributes to  $\sim 30\%$  (95% confidence interval is [12,49]) of the overall precipitation change (results not shown).

#### 5.4.2 Changes in Eastern Hemisphere Walker circulation

In this section, we investigate the circulation changes that give rise to the correlation between the OND Indian Ocean zonal SST gradient and simultaneous precipitation in East Africa. The main changes are in the Walker circulation, which are shown for much of the eastern Hemisphere stretching from  $20^\circ\text{W} - 160^\circ\text{E}$ . To define the Walker circulation, we employ the approach used by Chen (2005), and many others, to define atmospheric overturning circulations. In this approach, the first step involves decomposing the horizontal wind vector into its divergent and rotational components. A zonal (meridional) cell is then defined from the zonal (meridional) component of the divergent wind and the vertical velocity.

The tropical zonal circulation plotted in Fig. 5.7a show three overturning cells: 1) A narrow cell featuring strong ascending motion to the west and subsidence to the east is found in East Africa extending towards the western Indian Ocean. The descending branch of this cell coincides with the semi-arid areas in East Africa. The ascending branch correspond to the major source of diabatic heating over Congo. We refer to this as the East African Walker cell. 2) A shallower East Atlantic cell is found on the west flank of the East African Walker cell. 3) To the east, the East African cell is flanked by a broader Indian Ocean cell. In most models used here, the background zonal circulation is broadly similar to that found in the ERA40 reanalysis despite the differences in the analysis period considered (1901–2000 and 1958–2000 for the PCMDI and ERA40 data, respectively).

A dominant feature in projected changes in atmospheric upward vertical velocity is a weakening of the ascending branch of the East Atlantic Walker cell over central Africa. A reduction in  $\omega$  exceeding  $2 \times 10^{-4} \text{ mbs}^{-1}$  is found in most models in the middle to upper troposphere. Almost all the CGCMs, show positive differences in the omega velocities over the descending branch of the narrow East African Walker cell. Although not statistically significant in some of the models, these changes imply a weakening of the climatological subsidence over the eastern semi-arid regions. These results are in qualitative agreement with Vecchi and Soden (2007), who used different metrics to measure the intensity of the zonal circulation than are used here.

The future behavior of the eastern Hemisphere Walker circulation show a tendency towards positive IOZM-like state, consistent with the results presented in Sec. 5.4.1 suggesting that the IPCC-AR4 models have physical parameterizations of convective processes that respond realistically to the changes in forcings found

here. Vecchi and Soden (2007) argue that atmospheric thermodynamics are the principal drivers behind the weakening of the Indo-Pacific Walker circulation. Investigating the cause of the weakening is not the objective of the present study. The aim of our analysis has been to diagnose physical factors underlying the modelled precipitation changes.

### 5.5 Discussion and Conclusions

In this study, we investigated possible changes in the intensity of mean and extreme precipitation rates in East Africa from the CMIP3 multi-model dataset. Evidence in support of a future positive shift in the rainfall distribution under global warming has been presented. Increases in both mean precipitation rates and the intensity of 10-year wettest events are simulated almost throughout the region, while dry extremes are becoming less severe. This is the case even in the semi-arid climate in northern Kenya and southern Somalia. The presence of a dipole between southern Africa (cf. SHO09) and East Africa in the precipitation response, a robust feature of interannual rainfall variability in the climate system (e.g. Goddard and Graham, 1999), is particularly reassuring. A prime example of this feature is the 2006–2007 austral summer season. Unprecedented wet conditions in East Africa (Kenya) in November preceded one of the worst droughts in much of southern Africa. The qualitative agreement with previous findings (Kharin and Zwiers, 2000; Giorgi and Mearns, 2002, 2003; Tebaldi et al., 2004) provides an additional reassurance.

A robust feature across the CGCMs is an increase in atmospheric column integrated water vapour during the transition seasons (autumn and spring), particularly in the tropical region. Despite discrepancies in the magnitudes of the linear trends, all models show upward trends in precipitable water in the future climate (not shown). Although the increase in water vapor in a warmer atmosphere is offset to some extent by a slowdown of the tropical circulation (Vecchi and Soden, 2007), this trend alone is favourable for an increase in the precipitation almost everywhere in the tropics by about 3% (Held and Soden, 2006). Dynamical effects however force spatial inhomogeneities in the global warming-induced tropical rainfall increases. For instance, projections for rainfall in East Africa are higher than the zonal mean. This is in part caused by anomalous moisture flux convergence over East Africa (discussed in the KNMI Africa scenarios web-site).

Most models show a stronger boreal autumn warming in the western tropical Indian Ocean relative to the south-eastern part of the ocean. This is favourable for a higher probability of positive IOZM events. An important attribute of the positive phase of the IOZM is that it forces excessive short-rains in East Africa. It is physically reasonable, therefore, to conclude from this ocean-atmosphere cou-

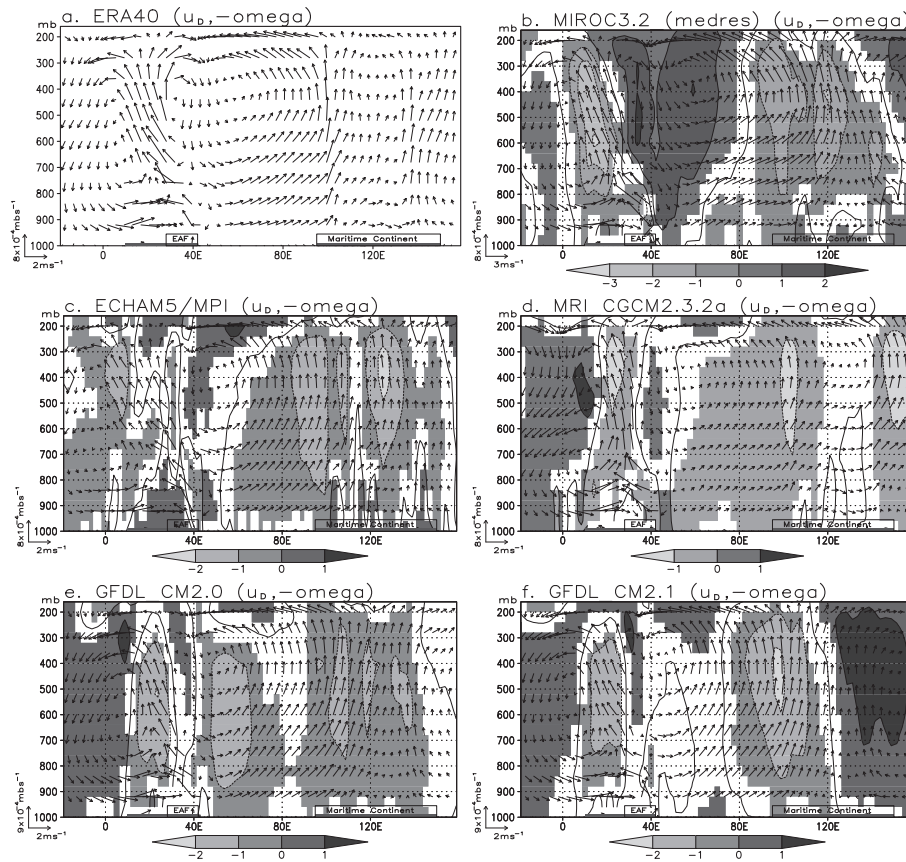


Fig. 5.7: October–December (OND) meridionally averaged ( $10^\circ \text{S}–4^\circ \text{N}$ ) divergent zonal wind ( $u_D$ ;  $\text{m s}^{-1}$ ) and negatively transformed pressure vertical velocity [ $-\omega$  ( $\text{mbs}^{-1}$ )] in the ERA40 reanalysis 1958–2000 (a) and the selected IPCC-AR4 models (b–h). The model names are shown in the titles. Future (2051–2200) minus present (1901–2000) differences in  $-\omega$  are superimposed; contour interval  $1 \times 10^{-4} \text{mbs}^{-1}$ . Positive (negative) differences are shown by the solid (dashed) lines. Statistically significant differences at the 5% level (from a  $z$ -test) are shaded (color bar units are  $\times 10^{-4} \text{mbs}^{-1}$ ). The approximate location of the East Africa (EAF) and the Maritime continent are indicated at the bottom of each figure.

pling pattern that global warming could enhance the likelihood of anomalously strong short-rains. In most subregions of East Africa, dynamically-driven rainfall increases, which contribute up to about 30%, are likely to work in concert with other mechanisms to force an overall increase in mean precipitation.

Related to changes in the tropical Indian Ocean zonal SST gradients are changes in the structure of the Eastern Hemisphere Walker circulation. Climatological subsidence over East Africa and the neighboring ocean area is projected to weaken. Boreal fall ascent over the Congo Basin is projected to become either shallower or slower. These features resemble a positive IOZM-like state of the Walker cell, which has been found to communicate the IOZM signal to East Africa precipitation. The presence of such a pattern in the future climate suggest that climate change will to a large extent resemble interannual variability in this regard.

The higher frequency of wetter conditions resulting in floods observed in recent years could give indications that the CGCM simulated precipitation responses are already occurring. Indeed, the time series of the simulated precipitation show upward trends from early in the present century. Nevertheless, from an applications perspective, there have also been reports of continued decline in stream flow and water levels in e.g. Lake Victoria, which may seem paradoxical given the recent dominance of wetter conditions in East Africa. However, we note that river/dam levels are also determined by other factors (e.g. water use, drainage and evaporation), which have not been considered in this paper. Despite the overall positive shift in the rainfall distribution projected in East Africa, the implications of climate change for water resources in this region can only be assessed on the basis of the pattern of precipitation minus evaporation (P-E), and its possible spatial and temporal variance, all of which deserve further investigation.

The increase in the intensity of 10-year wettest events translates into rising flood risks for the region, with implications for disaster management, development planning and local livelihoods. In addition, both the rising temperatures and the higher risk of excessive rainfall have implications for the health sector, for instance by shifting and/or extending the areas affected by vector-borne diseases such as malaria or the Rift Valley fever.



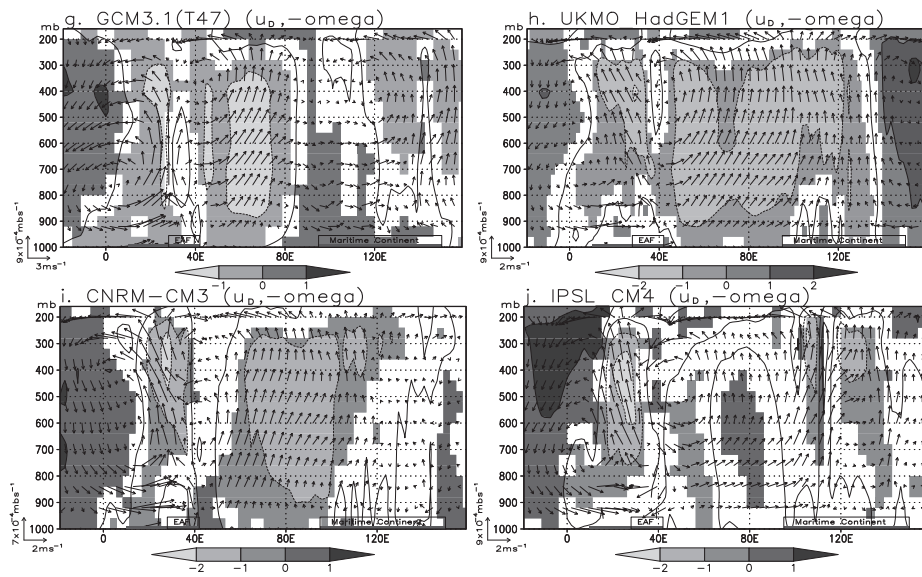


Fig. 5.7: continued...

## 6. SUMMARY AND IMPLICATIONS

### 6.1 *Summary*

In this thesis, seasonal climate extremes have been investigated with emphasis directed toward the mechanisms responsible for their occurrence, their predictability, and their likely response to global warming. To meet our goal, observations, reanalysis data, model simulations and predictions have been analyzed. Hitherto, climate models' ability to accurately mimic the behavior of the climate system in many parts of the globe including Europe varies with the season. Also the performance of the models depends on the meteorological variable. There is generally higher skill for temperature predictions than for precipitation. Against this background, the central focus of this thesis has been on specific seasons when climate extremes typically occur.

Owing to the non-stationarity of the climate and the recent occurrence of unprecedented seasonal climate extremes, numerical models have a clear advantage over purely statistical models, particularly those that are linear, in long-range prediction of the extremes. However, in order to make skilful seasonal predictions, adequate representation of the physical processes and feedbacks underlying the occurrence of climate extremes is necessary.

In **Chapter 2** we have investigated and identified the main driving controls of the extremely mild Autumn 2006 in Europe. We have provided a firm evidence supporting that anomalous surface turbulent-heat fluxes over the central North Atlantic Ocean, which previous studies overlooked, played an important role in forcing the extreme event. In contrast, previous studies assume that the warm ocean surface off the coast of north Africa provided the energy advected into Europe by the south-westerlies. Our results clearly invalidate this assumption. Within Europe, the water vapor feedback, which resulted from anomalously high precipitable water contributed cooperatively to enhance the warming.

The persistence of the surface heat flux anomalies in the North-Atlantic Ocean and their link to the unprecedented temperature anomalies are encouraging for prospects of predictability of extreme seasons in Europe. Our results which suggest some predictability of an extreme event such as Autumn 2006 from North Atlantic sea-surface conditions validates previous findings (Czaja and Frankignoul,

1999), who argued that the North-Atlantic Ocean exerts a discernible influence on the European climate in Autumn. However, that this unprecedented extreme season results mainly from atmospheric circulation and parameterized processes such as surface energy fluxes, radiative energy transfer, convection and condensation demonstrates that an inadequate representation of these processes places fundamental limits on the predictability problem.

In **Chapter 3** the predictability of extremely cold spring seasons in Europe has been associated with land-surface energy and hydrological processes. Our findings emphasize the importance of an accurate representation of snow processes during the melt season for skilful forecasts of cold spring seasons in Europe to be produced by numerical seasonal forecasting models. An observational analysis shows that land-surface forcing from snow exerts a discernible lagged influence on cold spring seasons. Hence this forcing can provide a predictable signal in eastern Europe. Seasons characterized by widespread snow from February to March tend to be followed by cold spring seasons in the vicinity of the snow zone. The mechanisms involved in this snow-forcing, which alter the surface energy balance, have been extensively documented in literature (e.g., Cohen and Rind, 1991).

The areas where the highest forecast skill is found in the best performing models tend to have the strongest influence from snow during spring. The skill in predicting the cold extreme seasons exceeds that of predicting near-average seasons and warm extremes. We have shown that the best performing models have a more realistic snow season, particularly during the crucial melting season. This study demonstrates that an improved and a more comprehensive representation of land-atmosphere processes involving snow in dynamical seasonal forecasting models will likely result in more skilful forecasts of cold spring seasons in Europe. In **Chapter 4** we have presented climate change scenarios for southern Africa. The associated uncertainties notwithstanding, some features agree relatively well among the selected climate models. First, a contraction of the rainfall season in southern Africa south of about  $15^{\circ}$  S is a consistent feature. This is due to the coexistence of a delayed rainfall onset and an early cessation found in the AR4 model simulations. It is hypothesized that a change in the pattern of lower-tropospheric moisture transported by the mean circulation is of central importance to limit precipitation formation during the onset season. Drier soils from the previous winter may play a secondary role, because local moisture recycling in spring is found to be weak. Second, a regional pattern similar to the "rich-get-richer" mechanism (Chou et al., 2009) featuring drying over the semi-arid areas close to the Kalahari Desert and wetting north of  $\sim 15^{\circ}$  S is found during austral summer months (i.e. the peak of the rainfall season). Close to the Kalahari, a significant decrease in mean seasonal precipitation parallels a change towards more severe 10-yr droughts. The risk of an expansion of the desert area is therefore high.

Third, low-frequency rainfall variability remains a prominent feature in the southern Africa future time-series. In the drying areas, the downward trend becomes notable after 2050. While not conclusive, our findings suggest that the future behavior of the tropical-temperate trough system is likely to play a role. However, owing to the lack of agreement across the selected climate models, the real physical mechanisms responsible for the dipole pattern of summer (DJF) precipitation change in southern Africa remain ambiguous.

An important finding in **Chapter 5** is a robust increase of precipitation in East Africa relative to other regions within the same latitudinal belt. A positive shift of the entire rainfall probability-density function is projected almost everywhere in East Africa. In the bimodal rainfall regime, precipitation increases are simulated during both the short- and the long-rains. Similar rainfall changes are simulated in the unimodal rainfall regime during the boreal winter–spring months. Mean precipitation increases emerge very early in the twenty-first century in qualitative agreement with observations over the last few years to a decade.

The selected IPCC AR4 models are able to reproduce the known empirical relationship between boreal autumn tropical Indian Ocean zonal SST gradients and East Africa short rains. The simulated precipitation changes are to some extent determined by a shift in the eastern Hemisphere Walker circulation and to changes in SST gradients associated with the Indian Ocean zonal mode (IOZM). In boreal autumn, during the positive IOZM phase which occurs with a higher probability under global warming, surface heat flux anomalies induce anomalous convection close to the warm pole and stronger low-level easterlies across the tropical Indian Ocean. This feature which is known from observational and model studies is adequately captured in most of the selected IPCC AR4 models. Because this teleconnection pattern influences interannual rainfall variability in East Africa, one can conclude that to a considerable extent, climate change resembles interannual variability in the present climate.

## 6.2 *Implications of this research*

Our findings are expected to contribute to current attempts to produce skilful forecasts of seasonal extremes and to improve our understanding of the mechanisms contributing to precipitation changes in southern and East Africa. Furthermore, our findings offer guidance into policy options and adaptation strategies for sustainable development in southern and East Africa.

How could these research findings be made useful for the communities requiring climate change adaptation strategies such as in southern and East Africa? This was one of the key questions raised during the Kenya Meteorological Society (KMS) workshop held in Kisumu, Kenya in September 2009. Based upon the discussions

during the workshop, our results on future precipitation projections can find useful applications. In Africa, cost-loss analyses that would help develop climate change adaptation policies focusing on water management and regulation of water use are required.

In East Africa, where an increase in precipitation is projected, the costs of developing and continuously maintaining water storage facilities need to be evaluated against the losses due to water shortages during dry periods. Although droughts are projected to become less probable in the future climate (cf. Chapter 5), whenever they occur, they still have devastating effects on humans, livestock and terrestrial ecosystems. The 2009 drought due to the failure of the long-rains is an example of a severe drought in an otherwise wetting climate.

Costs of confining water flows to predetermined channels by constructing high earthen walls along river banks in East Africa need to be evaluated against the losses due to spilling of water to adjoining areas. Extending river banks can also be a viable option.

Costs of improving drainage systems and maintenance of flood management structures in East Africa's flood prone areas need to be evaluated against the losses due to flash flooding and damages to infrastructure.

In those parts of southern Africa where precipitation is projected to decrease, the costs of replacing water hungry plant species such as eucalyptus trees with water friendly ones need to be considered. These can be compared against the effect these plants have on the scarce terrestrial water resources by draining ground water thereby leading to drying of stream and river flows.

Costs of human and wildlife resettlement should be considered in those areas in southern Africa where our results (cf. Chapter 4) point to a high risk of an extension of semi-arid climates such as in regions close to the Kalahari Desert.

The cost-benefit analyses recommended above should guide the decision making process in the midst of large uncertainties associated with future precipitation evolutions. The recommendations have been restricted to those regions where our analyses suggest a robust and consistently modelled climate change signal.

## APPENDIX

### *Appendix A: Methodology used in extreme value analysis*

The peak-over-threshold method or generalized Pareto distribution (GPD) has been used as the extreme value model in this study. We follow the approach described by Coles (2001). In this approach, a threshold intensity  $u$  is determined a priori. The data exceeding the threshold ( $z : z > u$ ) are then fitted to a GPD, defined as

$$G(z; \sigma, \xi, u) = \begin{cases} 1 - \left(1 + \frac{\xi(z-u)}{\sigma}\right)^{-1/\xi} & \xi \neq 0 \\ 1 - e^{-(z-u)/\sigma} & \xi = 0, \end{cases} \quad (\text{i})$$

where  $\sigma > 0$  and  $\xi$  are the scale and shape parameters of the distribution, respectively, such that

$$1 + \frac{\xi(z-u)}{\sigma} > 0. \quad (\text{ii})$$

This distribution gives the probability that a random variable  $z$  is higher than a high value conditional on it exceeding the predefined threshold  $u$ .

In this study, we set the threshold to the 80th percentile for the wet extremes to ensure an adequate number of excesses and a sufficiently small variance in the estimated model parameters. For dry extremes, the data are subjected to a negative transformation, and the excesses are defined analogously. For climate models with  $m$  integrations, each ensemble member is considered as an independent realization. The ensemble members are then concatenated to form a larger sample. This specification has allowed  $m \times 20$  ( $m \times 30$ ) exceedances in the control (future) climate record of 100 (150) years. However, in certain cases, notably when  $m > 1$ , the quality of the GPD fit, as assessed using an Anderson-Darling test (see below), was poor. Guided by the mean residual life plot (Coles, 2001), the threshold was then adjusted to improve the quality of the fit.

The GPD parameters (i.e.,  $\sigma$  and  $\xi$ ) have been estimated using maximum likelihood. The estimated parameters are then used to in the quantile function used to calculate the return level  $z_p$ . The return level  $z_p$  is that level which has probability  $p$  of being exceeded in a given year, or, defined differently, the level likely to be

exceeded once every  $1/p$  years. Based on Eq. (i), it is given by

$$z_p = \begin{cases} u + \frac{\sigma}{\xi} \left[ (p\zeta_u)^\xi - 1 \right] & \xi \neq 0 \\ u + \sigma \log(p\zeta_u) & \xi = 0. \end{cases} \quad (\text{iii})$$

The quantity  $\zeta_u$  gives the probability of exceeding the predefined threshold and has a variance approximately  $\zeta_u(1 - \zeta_u)/n$ . This follows from the argument that in a sample of size  $n$ , the number of threshold exceedances ( $n_u$ ) has a binomial distribution [i.e.,  $n_u \sim \text{Bin}(n, \zeta_u)$ ]. The uncertainties in the estimates of  $\zeta_u \approx n_u/n$ ,  $\sigma$  and  $\xi$  are incorporated in estimating the uncertainty associated with the estimate of  $z_p$ . This is achieved using the variance-covariance matrix for  $(\zeta_u, \sigma, \xi)$ , given by

$$V = \begin{bmatrix} \text{Var}(\zeta_u) & 0 & 0 \\ 0 & \frac{\partial^2 \ell(\theta)}{\partial \sigma^2} & \frac{\partial^2 \ell(\theta)}{\partial \sigma \partial \xi} \\ 0 & \frac{\partial^2 \ell(\theta)}{\partial \sigma \partial \xi} & \frac{\partial^2 \ell(\theta)}{\partial \xi^2} \end{bmatrix} \quad (\text{iv})$$

Here  $v_{12} = v_{21} = \text{cov}(\zeta_u, \sigma)$ ;  $v_{31} = v_{13} = \text{cov}(\zeta_u, \xi)$ ;  $v_{23} = v_{32} = \text{cov}(\sigma, \xi)$ ;  $v_{22} = \text{var}(\sigma)$ ;  $v_{33} = \text{var}(\xi)$ . In each case, the partial derivatives of the likelihood function  $[\ell(\theta)]$  are evaluated at the estimated GPD parameters.

The standard error in the estimate of  $z_p$  is obtained from the square root of  $\text{var}(z_p)$ , given by

$$\text{var}(z_p) = \begin{bmatrix} \frac{\partial z_p}{\partial \zeta_u} & \frac{\partial z_p}{\partial \sigma} & \frac{\partial z_p}{\partial \xi} \end{bmatrix}^T \begin{bmatrix} \text{Var}(\zeta_u) & 0 & 0 \\ 0 & \frac{\partial^2 \ell(\theta)}{\partial \sigma^2} & \frac{\partial^2 \ell(\theta)}{\partial \sigma \partial \xi} \\ 0 & \frac{\partial^2 \ell(\theta)}{\partial \sigma \partial \xi} & \frac{\partial^2 \ell(\theta)}{\partial \xi^2} \end{bmatrix} \begin{bmatrix} \frac{\partial z_p}{\partial \zeta_u} & \frac{\partial z_p}{\partial \sigma} & \frac{\partial z_p}{\partial \xi} \end{bmatrix}. \quad (\text{v})$$

The  $100(1 - \alpha)\%$  confidence interval of  $z_p$  is then expressed as

$$z_p \pm Z_{\alpha/2} \sqrt{\text{Var}(z_p)} \quad (\text{vi})$$

Where,  $Z_{\alpha/2}$  is the  $(1 - \alpha/2)\%$  point of the standard normal distribution. The return levels estimated from this approach have Gaussian likelihoods, which conforms with the requirement of the Bayesian multimodel ensembling method used in this study (see Tebaldi et al., 2005).

### Appendix B: Goodness of fit tests

Prior to estimating the return level  $z_p$ , Anderson-Darling goodness-of-fit tests have been performed. In this test, a quadratic measure of the discrepancies between

the fitted and empirical cumulative distribution functions (CDF), weighted by  $[G(z)(1 - G(z))]^{-1}$  is expressed as

$$A^2 = n_u \int_{z:z>u}^{z_{n_u}} [G_{n_u}(z) - G(z)]^2 [G(z)(1 - G(z))]^{-1} dG(z). \quad (\text{vii})$$

In this way, discrepancies occurring at the tails are weighted more than those in the central part of the distribution. The empirical CDF  $G_{n_u}(z)$  is calculated using

$$G_{n_u}(z) = \begin{cases} 0, & z < u \\ \frac{i}{n_u}, & z_i \leq z < z_{i+1}, \quad i = 1, \dots, n_u - 1 \\ 1, & z = z_{n_u}, \end{cases} \quad (\text{viii})$$

Conventionally, the test statistic is estimated by

$$A^2 = -n_u - \sum_{i=1}^{n_u} \frac{2i-1}{n_u} [\log G(z) + \log(1 - G(z_{n_u+1-i}))]. \quad (\text{ix})$$

The null hypothesis—that the data exceeding the predefined threshold ( $u$ ) has a generalized Pareto distribution—is rejected whenever the test statistic value exceeds the critical value at the specified level of significance (i.e., one-sided test).



## BIBLIOGRAPHY

African Development Bank (AfDB), Asian Development Bank (ADB), Department for International Development (DFID, UK), Federal Ministry for Economic Cooperation and Development (BMZ, Germany), Directorate-General for Development European Commission (EC), Ministry of Foreign Affairs – Development Cooperation (DGIS, The Netherlands), Organisation for Economic Cooperation and Development (OECD), United Nations Development Programme (UNDP), United Nations Environment Program (UNEP), and World Bank, 2003: Poverty and climate change: Reducing the vulnerability of the poor through adaptation. World Bank, Washington DC.

Alexander, L. V., X. Zhang, T. C. Peterson, J. Caesar, B. Gleason, A. M. G. K. Tank, M. Haylock, D. Collins, B. Trewin, F. Rahimzadeh, A. Tagipour, K. R. Kumar, J. Revadekar, G. Griffiths, L. Vincet, D. B. Stephenson, J. Burn, A. Aguilar, M. Brunet, M. Taylor, M. New, P. Zhai, M. Rusticucci, and J. L. Vazquez-Aguirre, 2006: Global observed changes in daily climate extremes of temperature and precipitation. *J. Geophys. Res.*, **111**, D05109, doi:10.1029/2005JD006290.

Anderson, D. L. T., T. Stockdale, M. A. Balmaseda, L. Ferranti, F. Vitart, P. Doblaser-Reyes, R. Hagedorn, T. Jung, A. Vidard, A. Troccoli, and T. Palmer, 2003: Comparison of the ECMWF seasonal forecast systems 1 and 2, including the relative performance for the 1997/8 El Niño. Technical Memoranda 404, ECMWF, Shinfield Park, Reading, U.K.

Anyah, R. O. and F. H. M. Semazzi, 2007: Variability of East African rainfall based on multiyear RegCM3 simulations. *Int. J. Climatol.*, **27**, 357–371.

Barnett, T. P. and R. Preisendorfer, 1987: Origins and levels of monthly and seasonal forecast skill for United States surface air temperatures determined by canonical correlation analysis. *Mon. Wea. Rev.*, **115**, 1825–1850, doi:10.1256/qj.04.176.

Barnston, A. G., A. Kumar, L. Goddard, and M. P. Hoerling, 2005: Improving seasonal climate prediction practices through attribution of climate variability. *Bull. Amer. Met. Soc.*, **86**, 59–72.

- Barnston, A. G. and T. M. Smith, 1996: Specification and prediction of global surface temperatures and precipitation from global SST using CCA. *J. Climate*, **9**, 2660–2697.
- Behera, S. K., J.-J. Luo, S. Masson, P. Delecluse, S. Gualdi, A. Navarra, and T. Yamagata, 2005: Paramount impact of the Indian Ocean dipole on the East African short rains: A CGCM study. *J. Climate*, **18**, 4514–4530.
- Behera, S. K. and T. Yamagata, 2001: Subtropical SST dipole events in the southern Indian Ocean. *Geophys. Res. Lett.*, **28**, 327–330.
- Beniston, M., 2004: The 2003 heat wave in Europe: A shape of things to come? An analysis based on swiss climatological data and model simulations. *Geophys. Res. Lett.*, **31**, doi:10.1029/2003GL018857.
- Beniston, M., D. B. Stephenson, O. B. Christensen, C. A. T. Ferro, C. Frei, S. Goyette, K. Halsnaes, T. Holt, K. Jylhä, B. Koffi, J. Palutikof, R. Schöll, T. Semmler, and K. Woth, 2007: Future extreme events in European climate: an exploration of regional climate model projections. *Climate Change*, **81**, 71–95, doi:10.1007/s10584-006-9226-z.
- Biasutti, M. and A. Giannini, 2006: Robust Sahel drying in response to late 20th century forcings. *Geophys. Res. Lett.*, L11706.
- Black, E., J. Slingo, and K. R. Sperber, 2003: An observational study of the relationship between excessively strong short rains in coastal East Africa and Indian Ocean SST. *Mon. Wea. Rev.*, **131**, 74–94.
- Bretherton, C., C. Smith, and J. M. Wallace, 1992: An intercomparison of methods for finding coupled patterns in climate data. *J. Climate*, **5**, 541–560.
- Brown, R. S., 2000: Northern Hemisphere snow cover variability and change, 1915–97. *J. Climate*, **13**, 2339–2355.
- Cassou, C., L. Terray, J. W. Hurrell, and C. Deser, 2004: North Atlantic winter climate regimes: spatial asymmetry, stationarity with time, and oceanic forcing. *J. Climate*, **17**, 1055–1068.
- Cassou, C., L. Terray, and A. S. Phillips, 2005: Tropical Atlantic influence on European heat waves. *J. Climate*, **18**, 2805–2811.
- Cattiaux, J., R. Vautard, and P. Yiou, 2009: Origins of the extremely warm European fall in 2006. *Geophys. Res. Lett.*, **36**, doi:10.1029/2009GL037339.

- Chase, T. N., K. Wolter, R. A. P. Sr., and I. Rasool, 2006: Was the 2003 European summer heat wave unusual in a global context? *Geophys. Res. Lett.*, **33**, L23709.
- Chen, T.-C., 2005: Maintenance of the midtropospheric north African summer circulation: Saharan high and African easterly jet. *J. Climate*, **18**, 2943–2962.
- Chou, C., J. D. Neelin, C.-A. Chen, and J.-Y. Tu, 2009: Evaluating the "rich-get-richer" mechanism in tropical precipitation change under global warming. *J. Climate*, **22**, 1982–2005.
- Ciais, P., M. Reichstein, N. Viovy, A. Granier, J. Ogee, V. Allard, M. Aubinet, N. Buchmann, C. Bernhofer, A. Carrara, F. Chevallier, N. D. Noblet, A. D. Friend, P. Friedlingstein, T. Grünwald, B. Heinesch, P. Keronen, A. Knohl, G. Krinner, D. Loustau, G. Manca, G. Matteucci, F. Miglietta, J. M. Ourcival, D. Papale, K. Pilegaard, S. Rambal, G. Seufert, J. F. Soussana, M. J. Sanz, E. D. Schulze, T. Vesala, and R. Valentini, 2005: Europe-wide reduction in primary productivity caused by the heat and drought in 2003. *Nature*, **437**, 529–533, doi:10.1038/nature03972.
- Clark, C. O., P. J. Webster, and J. E. Cole, 2003: Interdecadal variability of the relationship between the Indian Ocean zonal mode and East African coastal rainfall anomalies. *J. Climate*, **16**, 548–554.
- Cohen, J. and D. Rind, 1991: The effect of snow on climate. *J. Climate*, **4**, 689–706.
- Coles, S., 2001: *An Introduction to Statistical Modeling of Extreme Values*. Springer Series in Statistics, London, UK, 208 pp.
- Cook, B., G. B. Bonan, and S. Levis, 2006: Soil moisture feedbacks to precipitation in Southern Africa. *J. Climate*, **19**, 4198–4206.
- Cook, K., 2000a: A Southern Hemisphere wave response to ENSO with implications for southern Africa precipitation. *J. Atmos. Sci.*, **58**, 2146–2162.
- Cook, K. H., 2000b: The south Indian convergence zone and interannual variability over southern Africa. *J. Climate*, **13**, 3789–3804.
- Cook, K. H. and E. K. Vizy, 2006: Coupled model simulations of the West African monsoon system: twentieth- and twenty-first-century simulations. *J. Climate*, **19**, 3681–3703.
- Czaja, A. and C. Frankignoul, 1999: Influence of the North Atlantic SST on the atmospheric circulation. *Geophys. Res. Lett.*, **26**, 2969–2972.

Delworth, T. L., A. J. Broccoli, A. Rosati, R. J. Stouffer, V. Balaji, J. A. Beesley, W. F. Cooke, K. W. Dixon, J. Dunne, K. A. Dunne, J. W. Durachta, K. L. Findell, P. Ginoux, A. Gnanadesikan, C. T. Gordon, S. M. Griffies, R. Gudgel, M. J. Harrison, I. M. Held, R. S. Hemler, L. W. Horowitz, S. A. Klein, T. R. Knutson, P. J. Kushner, A. R. Langenhorst, H.-C. Lee, S.-J. Lin, J. Lu, S. L. Malyshev, P. C. D. Milly, V. Ramaswamy, J. Russell, M. D. Schwarzkopf, E. Shevliakova, J. J. Sirutis, M. J. Spelman, W. F. Stern, M. Winton, A. T. Wittenberg, B. Wyman, F. Zeng, and R. Zhang, 2006: GFDLs CM2 global coupled climate models. part I: Formulation and simulation characteristics. *J. Climate*, **19**, 643–674.

Dewey, K. F., 1977: Daily maximum and minimum temperature forecasts and the influence of snow cover. *Mon. Wea. Rev.*, **105**, 1594–1597.

Doblas-Reyes, F. J., V. Pavan, and D. B. Stephenson, 2003: The skill of multi-model seasonal forecasts of the wintertime north atlantic oscillation. *Climate Dyn.*, **21**, 501–514, doi:10.1007/s00382-003-0350-4.

Douville, H., 2000a: Influence of soil moisture on the Asian and African monsoons. Part II. Interannual variability. *J. Climate*, **15**, 701–720.

— 2000b: Relevance of soil moisture for seasonal climate predictions: A preliminary study. *Climate Dyn.*, **16**, 719–736.

— 2009: Relative contribution of soil moisture and snow mass to seasonal climate predictability: A pilot study. *Climate Dyn.*, in press.

Douville, H. and F. Chauvin, 2004: Relevance of soil moisture for seasonal atmospheric predictions: Is it an initial value problem. *Climate Dyn.*, **22**, 429–446.

Douville, H., F. Chauvin, and H. Broqua, 2000: Influence of soil moisture on the Asian and African monsoons. Part I. Mean monsoon and daily precipitation. *J. Climate*, **14**, 2381–2403.

Fan, Y. and H. van den Dool, 2008: A global monthly land surface air temperature analysis for 1948–present. *J. Geophys. Res.*, **113**, doi:10.1029/2007JD008470.

Ferranti, L. and P. Viterbo, 2006: The European summer of 2003: sensitivity to soil water initial conditions. *J. Climate*, **19**, 3659–3680.

Fischer, E. M., S. I. Seneviratne, D. Lüthi, and C. Schär, 2007: Contribution of land-atmosphere coupling to recent European summer heat waves. *Geophys. Res. Lett.*, **34**, L06707.

Flato, G. M., 2005: The third generation coupled global climate model (CGCM3). World Wide Web, <http://www.cccma.ec.gc.ca/models/cgcm3.shtml>.

- Foster, J., G. Liston, R. Koster, R. Essery, H. Behr, L. Dumenil, D. Verseghy, S. Thompson, D. Pollard, and J. Cohen, 1996: Snow cover and snow mass intercomparisons of general circulation models and remotely sensed datasets. *J. Climate*, **9**, 409–426.
- Gershunov, A., 1998: ENSO influence on intraseasonal extreme rainfall and temperature frequencies in the contiguous United States: Implications for long-range predictability. *J. Climate*, **11**, 3192–3203.
- Gershunov, A. and T. P. Barnett, 1998: ENSO influence on intraseasonal extreme rainfall and temperature frequencies in the contiguous United States: Observations and model results. *J. Climate*, **11**.
- Giannini, A., R. Saravanan, and P. Chang, 2003: Oceanic forcing of Sahel rainfall on interannual to interdecadal time scales. *Science*, **302**, 1027–1030.
- Gillett, N. P., A. J. Weaver, F. W. Zwiers, and M. D. Flannigan, 2004a: Detecting the effect of human-induced climate change on Canadian forest fires. *Geophys. Res. Lett.*, **31**, L18211, doi:10.1029/2004GL020876.
- Giorgi, F. and R. Francisco, 2000: Uncertainties in regional climate change predictions. A regional analysis of ensemble simulations with the HADCM2 GCM. *Climate Dyn.*, **16**, 169–182.
- Giorgi, F. and L. O. Mearns, 2002: Calculation of average, uncertainty range, and reliability of regional climate changes from AOGCM simulations via the "reliability ensemble average" (REA) method. *J. Climate*, **15**, 1141–1158.
- 2003: Probability of regional climate change based on reliability ensemble average (REA) method. *Geophys. Res. Lett.*, **30**, 1629, doi:10.1029/2003GL017130.
- Goddard, L. and N. E. Graham, 1999: The importance of the Indian Ocean for simulating rainfall anomalies over eastern and southern Africa. *J. Geophys. Res.*, **104**, 19099–19116.
- Goddard, L., S. J. Mason, S. E. Zebiak, C. F. Ropelewski, R. Basher, and M. A. Cane, 2001: Current approaches to seasonal to interannual climate predictions. *Int. J. Climatol.*, **21**, 1111–1152.
- Gordon, C., C. Cooper, C. Senior, H. Banks, J. Gregory, T. Johns, J. Mitchell, and R. Wood, 2000: The simulation of SST, sea ice extents and ocean heat transports in a version of the Hadley Centre coupled model without flux adjustments. *Climate Dyn.*, **16**, 147–168.

Gordon, H. B., L. Rotstayn, J. McGregor, M. R. Dix, E. A. Kowalczyk, S. P. O'Farrell, L. J. Waterman, A. C. Hirst, S. G. Wilson, M. A. Collier, I. G. Watterson, and T. I. Elliott, 2002: The CSIRO Mk3 climate system model. Technical Research Paper 60, CSIRO Atmospheric Research, Aspendale, Victoria, Australia, 130pp.

Graham, R. J., M. Gordon, P. J. Mclean, S. Ineson, M. R. Huddleston, M. K. Davey, A. Brookshaw, and R. T. H. Barnes, 2005: A performance comparison of coupled and uncoupled versions of the Met Office seasonal prediction general circulation model. *Tellus*, **57A**, 320–339.

Graversen, R. G., 2006: Do changes in the midlatitude circulation have any impact on the Arctic surface air temperature trend? *J. Climate*, **19**, 5422–5438.

Graversen, R. G., E. Källén, M. Tjernström, and H. Körnich, 2007: Atmospheric mass-transport inconsistencies in the ERA-40 reanalysis. *Quart. J. Roy. Meteor. Soc.*, **133**, 673–680.

Groisman, P. Y., T. R. Karl, and R. W. Knight, 1994: Changes of snow cover, temperature, and radiative heat balance over the Northern Hemisphere. *J. Climate*, **7**, 1633–1656.

Groisman, P. Y., R. W. Knight, D. R., Easterling, T. R. Karl, G. C. Hegerl, and V. N. Razuvaev, 2005: Trends in intense precipitation in the climate record. *J. Climate*, **18**, 1326–1350.

Haarsma, R. J., F. M. Selten, S. L. Weber, and M. Kluiphuis, 2005: Sahel rainfall variability and response to greenhouse warming. *Geophys. Res. Lett.*, **32**, L17702, doi:10.1029/2005GL023232.

Hagos, S. M. and K. H. Cook, 2008: Ocean warming and late-twentieth-century Sahel drought and recovery. *J. Climate*, **21**, 3797–3814.

Hallegatte, S., A. Lahellec, and J.-Y. Grandpeix, 2006: An elicitation of the dynamic nature of water vapor feedback in climate change using a 1D model. *J. Atmos. Sci.*, **63**, 1878–1894.

Hastenrath, S., A. Nicklis, and L. Greischar, 1993: Atmospheric-hydrospheric mechanisms of climate anomalies in the western equatorial Indian Ocean. *J. Geophys. Res.*, **98**, 20219–20235.

Hastenrath, S. and D. Polzin, 2005: Mechanisms of climate anomalies in the equatorial Indian Ocean. *J. Geophys. Res.*, **110**, D08113, doi:10.1029/2004JD004981.

Hastenrath, S., D. Polzin, and C. Mutai, 2007: Diagnosing the 2005 drought in equatorial East Africa. *J. Climate*, **20**, 4628–4637.

- Hasumi, H., S. Emori, A. Abe-Ouchi, A. Hasegawa, T. Inoue, M. Kimoto, S. Matsumura, T. Nagashima, H. Nakano, T. Nishimura, T. Nozawa, R. Ohgaito, A. Oka, N. Okada, K. Ogochi, T. Ogura, F. Saito, K. Saito, T. Sakamoto, T. Segawa, T. Soga, K. Sudo, A. Sumi, T. Suzuki, H. Takahashi, K. Takata, T. Takemura, M. Takigawa, Y. Tsushima, M. Watanabe, S. Watanabe, and T. Yokohata, 2004: K-1 technical report. Technical Report 1, CCSR/NIES/FRCGC, Meguro-ku, Tokyo, Japan.
- Hegerl, G. C., T. R. Karl, M. Allen, N. L. Bindoff, N. Gillett, D. Karoly, X. Zhang, and F. Zwiers, 2006: Climate change detection and attribution: beyond mean temperature signals. *J. Climate*, **19**, 5058–5077.
- Held, I. M. and B. J. Soden, 2006: Robust responses of the hydrological cycle to global warming. *J. Climate*, **19**, 5686–5699.
- Hellmuth, M. E., A. Moorhead, M. C. Thomson, and J. Williams, eds., 2007: *Climate risk management in Africa: Learning from practice*. International Research Institute for Climate and Society (IRI), New York, USA, 116 pp.
- Hewitson, B. C. and R. G. Crane, 2006: Consensus between gcm climate change projections with empirical downscaling: precipitation downscaling over South Africa. *Int. J. Climatol.*, **26**, 1315–1337.
- Hoerling, M., J. Hurrell, J. Eischeid, and A. Phillips, 2006: Detection and attribution of twentieth-century northern and southern African rainfall change. *J. Climate*, **19**, 3989–4008.
- Houghton, J. T., Y. Ding, D. J. Griggs, M. Noguer, P. J. van der Linden, X. Dai, K. Maskell, and E. C. A. Johnson, 2001: *Climate Change 2001: The Scientific Basis*. Cambridge University Press, 881pp.
- Huang, J., H. M. van den Dool, and A. G. Barnston, 1996: Long-lead seasonal temperature prediction using optimal climate normals. *J. Climate*, **9**, 809–817.
- Hulme, M., R. Doherty, T. Ngara, M. New, and D. Lister, 2001: African climate change: 1900–2100. *Climate Research*, **17**, 145–168.
- Hurrell, J. W., Y. Kushnir, G. Ottersen, and M. Visbeck: 2003, An overview of the North Atlantic Oscillation. *The North Atlantic Oscillation: Climate Significance and Environmental Impact*, Geophysical Monograph Series, volume 134, 1–35.
- Hurrell, J. W. and H. van Loon, 1997: Decadal variations associated with the North Atlantic Oscillation. *Climate Change*, **36**, 301–326.
- Indeje, M., F. H. M. Semazzi, and L. J. Ogallo, 2000: ENSO signals in East African rainfall seasons. *Int. J. Climatol.*, **20**, 19–46.

IPCC, 2007: *Climate Change 2007: The Physical Science Basis. Contribution of Working Group I to the Fourth Assessment Report on the Intergovernmental Panel on Climate Change*[Solomon, S. and D. Qin and M. Manning and Z. Chen and M. Marquis and K. B. Averyt and M. Tignor and H. L. Miller (eds)] Cambridge University Press, Cambridge, United Kingdom and New York, NY, USA, 996pp.

Jackson, J. E., 1991: *A User's Guide to Principal Components*. Wiley-InterScience, New Jersey, 569pp.

Johansson, A., 2007: Prediction skill of the NAO and PNA from daily to seasonal time scales. *J. Climate*, **20**, 1957–1975.

Johns, T., C. Durman, H. Banks, M. Roberts, A. McLaren, J. Ridley, C. Senior, K. Williams, A. Jones, A. Keen, G. Rickard, S. Cusack, M. Joshi, M. Ringer, B. Dong, H. Spencer, R. Hill, J. Gregory, A. Pardeans, J. Lowe, A. Bodas-Salcedo, S. Stark, and Y. Searl, 2004: Hadgem1 model description and analysis of preliminary experiments for the IPCC Fourth Assessment Report. Technical Note 55, UK Meteorological Office, Exeter, UK, 75pp.

Johnson, R. A. and D. W. Wichern, 2002: *Applied multivariate statistical analysis*. Prentice Hall, New Jersey, 767pp.

Jolliffe, I. T., 1972: Discarding variables in principal component analysis. II: Real data. *Appl. Stat.*, **21**, 160–173.

Jolliffe, I. T. and D. B. Stephenson, eds., 2003: *Forecast Verification. A Practitioner's Guide in Atmospheric Science*. Wiley & Sons Ltd., 254pp.

Jones, P. D., 1994: Hemispheric surface air temperature variations: A reanalysis and an update to 1993. *J. Climate*, **11**, 1794–1802.

Jones, P. D., T. Jónsson, and D. Wheeler, 1997: Extension to the North Atlantic Oscillation using early instrumental pressure observations from Gibraltar and south-west Iceland. *Int. J. Climatol.*, **17**, 1433–1450.

Joubert, A. M., S. J. Mason, and J. S. Galpin, 1996: Droughts over southern Africa in a doubled-CO<sub>2</sub> climate. *Int. J. Climatol.*, **16**, 1149–1156.

Kanamitsu, M., W. Ebisuzaki, J. Woollen, S.-K. Yang, J. J. Hnilo, M. Fiorino, and G. L. Potter, 2002: NCEP–DEO AMIP-II Reanalysis (R-2). *Bull. Amer. Met. Soc.*, **83**, 1631–1643.

Karoly, D. J. and K. Braganza, 2005: Attribution of recent temperature changes in the Australian region. *J. Climate*, **18**, 457–464.



- Kenyon, J. and G. C. Hegerl, 2008: Influence of modes of climate variability on global temperature extremes. *J. Climate*, **21**, 3872–3889.
- Kharin, V. V. and F. W. Zwiers, 2000: Changes in the extremes in an ensemble of transient climate simulations with a coupled atmosphere–ocean GCM. *J. Climate*, **13**, 3760–3788.
- Kharin, V. V., F. W. Zwiers, X. Zhang, and G. C. Hegerl, 2007: Changes in temperature and precipitation extremes in the IPCC ensemble of global coupled model simulations. *J. Climate*, **20**, 1419–1444.
- Kiehl, J. T. and K. E. Trenberth, 1997: Earth’s annual global mean energy budget. *Bull. Amer. Met. Soc.*, **78**, 197–208.
- Klein, S. A., B. J. Soden, and N. C. Lau, 1999: Remote sea surface temperature variations during ENSO: Evidence of a tropical atmospheric bridge. *J. Climate*, **12**, 917–932.
- Klein Tank, A., J. B. Wijgaard, G. P. Können, R. Böhm, G. Demarée, A. G. A., M. Mileta, S. Pashiardis, L. Hejkrlik, C. Kern-Hansen, R. Heino, P. Bessemoulin, G. Müller-Westmeier, M. Tzanakou, S. Szalai, T. Pálsdóttir, D. Fitzgerald, S. Rubin, M. Capaldo, M. Maugeri, A. Leitass, A. Bukantis, R. Aberfeld, A. F. V. van Engelen, E. Forland, M. Miletus, F. Coelho, C. Mares, V. Razuvaev, E. Nieplova, T. Cegnar, J. A. López, B. Dahlström, A. Moberg, W. Kirchhofer, A. Ceylan, O. Pachaliuk, L. V. Alexander, and P. Petrovic, 2002: Daily dataset of 20th-century surface air temperature and precipitation series for the European Climate Assessment. *Int. J. Climatol.*, **22**, 1441–1453.
- Klein Tank, A. M. G., 2004: *Changing temperature and precipitation extremes in Europe’s climate of the 20th century*. Ph.D. thesis, University of Utrecht, 124pp.
- Klein Tank, A. M. G. and G. P. Können, 2003: Trends in indices of daily temperature and precipitation extremes in Europe, 1946–1999. *J. Climate*, **16**, 3665–3680.
- Klein Tank, A. M. G., T. C. Peterson, D. A. Quadir, S. Dorji, X. Zou, H. Tang, K. Santhosh, U. R. Joshi, A. K. Jaswal, R. K. Kolli, A. B. Sikder, N. R. Deshpande, J. V. Revadekar, K. Yeleuova, S. Vandasheva, M. Faleyeva, P. Gomboluudev, K. P. Budhathoki, A. Hussain, M. Afzaal, L. Chandrapala, H. Anvar, D. Amanmurad, V. S. Asanova, P. D. Jones, M. G. New, and T. Spektorman, 2006: Changes in daily temperature and precipitation extremes in central and south Asia. *J. Geophys. Res.*, **111**, D16105, doi:10.1029/2005JD006316.
- Kuhnel, I., 1989: Tropical–extratropical cloudband climatology. *Int. J. Climatol.*, **9**, 441–463.

- Kumar, A. and F. Yang, 2003: Comparative influence of snow and SST variability on extratropical climate in northern winter. *J. Climate*, **16**, 2248–2261.
- Laio, F., 2004: Cramer–von Mises and Anderson-Darling goodness of fit tests for extreme value distributions with unknown parameters. *Water Resour. Res.*, **40**, doi:10.1029/2004WR003204.
- Landman, W. A. and S. J. Mason, 2001: Forecasts of near-global sea-surface temperatures using canonical correlation analysis. *J. Climate*, **14**, 3819–3833.
- Latif, M., D. Dommenges, M. Dima, and A. Grötzner, 1999: The role of Indian Ocean sea surface temperature in forcing East African rainfall anomalies during December/January 1997/98. *J. Climate*, **12**, 3497–3504.
- Le Clainche, Y., P. Braconnot, O. Marti, S. Joussaume, J.-L. Dufresne, and M.-A. Filiberti, 2001: The role of sea ice thermodynamics in the Northern Hemisphere climate as simulated by a global coupled ocean-atmosphere model. Notes du Pôle de Modélisation 21, Institut Pierre Simon Laplace (IPSL), Paris, France, 26pp.
- Lenderink, G., A. P. van Ulden, van den Hurk B., and E. van Meijgaard, 2006: Summertime inter-annual temperature variability in an ensemble of regional model simulations: analysis of the surface energy budget. *Climatic Change*, **accepted**.
- Lu, J. and T. L. Delworth, 2005: Oceanic forcing of the late 20th century Sahel drought. *Geophys. Res. Lett.*, **32**, L22706, doi:10.1029/2005GL023316.
- Luterbacher, J., D. D., E. Xoplaki, E. Grosjean, and H. Wanner, 2004: European seasonal and annual temperature variability, trends and extremes since 1950. *Science*, **303**, 1499–1503.
- Luterbacher, J., M. A. Liniger, A. Menzel, N. Estrella, P. M. Della-Marta, C. Pfister, T. Rutishauser, and E. Xoplaki, 2007: Exceptional European warmth of autumn 2006 and winter 2007: Historical context, the underlying dynamics, and its phenological effects. *Geophys. Res. Lett.*, **34**, doi:10.1029/2007GL029951.
- Mason, S. J. and N. E. Graham, 1999: Conditional probabilities, relative operating characteristics, and relative operating levels. *Wea. Forecasting*, **14**, 713–725.
- 2002: Areas beneath the relative operating characteristics (ROC) and relative operating levels (ROL) curves: Statistical significance and interpretation. *Quart. J. Roy. Meteor. Soc.*, **77**, 2145–2166.
- Mason, S. J. and G. M. Mimmack, 2002: Comparison of some statistical methods of probabilistic forecasting of ENSO. *J. Climate*, **15**, 8–29.

- Mason, S. J., P. R. Waylen, G. M. Mimmack, B. Rajaratnam, and J. M. Harrison, 1999: Changes in extreme rainfall events in South Africa. *Climate Change*, **41**, 249–257.
- Mathieu, P.-P., R. T. Sutton, B. Dong, and M. Collins, 2004: Predictability of winter climate of the North Atlantic European region during ENSO events. *J. Climate*, **17**, 1953–1974.
- Meehl, G. A., J. M. Arblaster, and C. Tebaldi, 2005: Understanding future patterns of increased precipitation intensity in climate model simulations. *Geophys. Res. Lett.*, **32**, L18719, doi:10.1029/2005GL023680.
- Mimmack, G. M., S. J. Mason, and J. S. Galpin, 2001: Choice of distance matrices in cluster analysis: defining regions. *J. Climate*, **14**, 2790–2797.
- Min, S.-K., S. Legutke, A. Hense, and W.-T. Kwon, 2005: Internal variability in a 1000-yr control simulation with the coupled climate model ECHO-G I. near-surface temperature, precipitation and mean sea level pressure. *Tellus*, **57A**, 605–621.
- Mulenga, H. M., M. Rouault, and C. J. C. Reason, 2003: Dry summers in NE South Africa and associated circulation anomalies. *Climate Research*, **25**, 29–41.
- Mutai, C. C. and M. N. Ward, 2000: East African rainfall and the tropical circulation/convection on intraseasonal to interannual timescales. *J. Climate*, **13**, 3915–3939.
- Mutai, C. C., M. N. Ward, and A. W. Colman, 1998: Towards the prediction of the East African short rains based on sea-surface temperature and atmosphere coupling. *Int. J. Climatol.*, **18**, 975–997.
- Neelin, J. D., D. S. Battisti, A. C. Hirst, F.-F. Jin, Y. Wakata, T. Yamagata, and S. E. Zebiak, 1998: ENSO theory. *J. Geophys. Res.*, **103**, 14261–14290.
- New, M., B. Hewitson, D. B. Stephenson, A. Tsiga, A. Kruger, A. Manhique, B. Gomez, C. A. S. Coelho, D. N. Masisi, E. Kululanga, E. Mbambalala, F. Adesina, H. Saleh, J. Kanyanga, J. Adosi, L. Bulane, L. Fortunata, M. L. Mdoka, and R. Lajoie, 2006: Evidence of trends in daily climate extremes over southern and west Africa. *J. Geophys. Res.*, **111**, D14102, doi:10.1029/2005JD006289.
- New, M., M. Hulme, and P. Jones, 2000: Representing twentieth-century space-time climate variability. Part II: Development of 1901–96 monthly grids of terrestrial surface climate. *J. Climate*, **13**, 2217–2238.

- New, M., R. Washington, C. Jack, and B. Hewitson, 2003: Sensitivity of southern Africa climate to soil-moisture. *Clivar Exchanges*, **27**, 45–47.
- Nicholson, S. E. and J. Kim, 1997: The relationship of the El Niño-Southern Oscillation to African rainfall. *Int. J. Climatol.*, **17**, 117–135.
- Palmer, T. N., A. Alessandri, U. Andersen, P. Cantelaube, M. Davey, P. Délecluse, M. Déqué, E. Díez, F. J. Doblas-Reyes, H. Feddersen, R. Graham, S. Gualdi, J. F. Guérémy, R. Hagedorn, M. Hoshen, N. Keenlyside, M. Latif, A. Lazar, E. Maisonave, V. Marletto, A. P. Morse, B. Orfila, P. Rogel, J. M. Terres, and M. C. Thomson, 2004: Development of a European Multi-Model Ensemble System for Seasonal to Inter-Annual Prediction (DEMETER). *Bull. Amer. Met. Soc.*, **85**, 853–872.
- Peng, S. and W. A. Robinson, 2001: Relationships between atmospheric internal variability and the responses to an extratropical SST anomaly. *J. Climate*, **14**, 2943–2959.
- Peng, S., W. A. Robinson, and S. Li, 2003: Mechanisms for the NAO responses to the North Atlantic SST tripole. *J. Climate*, **16**, 1987–2004.
- Peterson, T. C., H. Daan, and P. D. Jones, 1997: Initial selection of a GCOS surface network. *Bull. Amer. Met. Soc.*, **78**, 2145–2152.
- Piao, S., P. Ciais, P. Friedlingstein, P. Peylin, M. Reichstein, S. Luyssaert, H. Margolis, J. Fang, A. Barr, A. Chen, A. Grelle, D. Y. Hollinger, T. Laurila, A. Lindroth, A. D. Richardson, and T. Vesala, 2008: Net carbon dioxide losses of northern ecosystems in response to autumn warming. *Nature*, **451**, 49–53, doi:10.1038/nature06444.
- Raval, A. and V. Ramanathan, 1989: Observational determination of the greenhouse effect. *Nature*, **342**, 758–761.
- Reason, C. J. C., 2002: Sensitivity of the southern African circulation to dipole SST patterns in the South Indian Ocean. *Int. J. Climatol.*, **22**, 377–393.
- 2007: Tropical cyclone Dera, the unusual 2000/01 tropical cyclone season in the south west Indian Ocean and associated rainfall anomalies over southern Africa. *Meteor. Atmos. Phys.*, **97**, 181–188.
- Reason, C. J. C., S. Hachigonta, and R. F. Phaladi, 2005: Interannual variability in rainy season characteristics over the Limpopo region of southern Africa. *Int. J. Climatol.*, **25**, 1835–1853.
- Reason, C. J. C. and I. Keibel, 2004: Tropical cyclone Eline and its unusual penetration and impacts over the southern African mainland. *Wea. Forecasting*, **19**, 789–805.

- Reason, C. J. C. and H. M. Mulenga, 1999: Relationships between South African rainfall and SST anomalies in the South West Indian Ocean. *Int. J. Climatol.*, **19**, 1651–1673.
- Robinson, D. A., K. F. Dewey, and R. R. J. Heim, 1993: Global snow cover monitoring: An update. *Bull. Amer. Met. Soc.*, **74**, 1689–1696.
- Rocha, A. and I. Simmonds, 1997a: Interannual variability of south-eastern African summer rainfall. Part 1: Relationships with air-seas interaction processes. *Int. J. Climatol.*, **17**, 235–265.
- 1997b: Interannual variability of south-eastern African summer rainfall. Part II. modelling the impact of sea-surface temperatures on rainfall and circulation. *Int. J. Climatol.*, **17**, 267–290.
- Rodwell, M. J.: 2003, On the predictability of North Atlantic climate. *The North Atlantic Oscillation: Climate Significance and Environmental Impact*, Geophysical Monograph Series, volume 134, 173–192.
- Roeckner, E., G. Bäuml, L. Bonaventura, R. Brokopf, M. Esch, M. Giorgetta, S. Hagemann, I. Kirchner, L. Kornblueh, E. Manzini, A. Rhodin, U. Schlese, U. Schulzweida, and A. Tompkins, 2003: The atmospheric general circulation model ECHAM5. Technical Report 349, Max-Planck-Institut für Meteorologie, Hamburg, Germany, 140pp.
- Ropelewski, C. F. and M. S. Halpert, 1987: Global and regional scale precipitation patterns associated with the El Niño/Southern Oscillation. *Mon. Wea. Rev.*, **115**, 1606–1626.
- Rouault, M., S. A. White, C. J. C. Reason, J. R. E. Lutjeharms, and I. Jobard, 2002: Ocean–atmosphere interaction in the Agulhas current region and a South African extreme weather event. *Wea. Forecasting*, **17**, 655–669.
- Saha, S., S. Nadiga, C. Thiaw, J. Wang, W. Wang, Q. Zhang, H. M. van den Dool, H. L. Pan, S. Moorthi, D. Behringer, D. Stokes, M. Pena, S. Lord, G. White, W. Ebisuzaki, P. Peng, and P. Xie, 2006: The NCEP climate forecast system. *J. Climate*, **15**, 3483–3517.
- Saji, H. N., B. N. Goswami, P. N. Vinayachandran, and T. Yagamata, 1999: A dipole mode in the tropical Indian Ocean. *Nature*, **401**, 360–363.
- Salas-Méllia, D., F. Chauvin, M. Déqué, H. Douville, J. F. Guérémy, P. Marquet, S. Planton, J. F. Royer, and S. Tyteca, 2005: Description and validation of the CNRM-CM3 global coupled model. *CNRM working note* 103.

- Scaife, A. A., C. K. Folland, L. V. Alexander, A. Moberg, and J. R. Knight, 2008: European climate extremes and the North Atlantic Oscillation. *J. Climate*, **21**, 72–83.
- Schär, C. and G. Jendritzky, 2004: Hot news from summer 2003. *Nature*, **432**, 559–560.
- Schär, C., P. L. Vidale, D. Lüthi, C. Frei, C. Häberli, M. A. Liniger, and C. Appenzeller, 2004: The role of increasing temperature variability in European summer heatwaves. *Nature*, **427**, 332–336.
- Seneviratne, S. I., D. Lüthi, M. Litshi, and C. Schär, 2006: Land-atmosphere coupling and climate change in Europe. *Nature*, **443**, 205–209.
- Shinoda, T., M. A. Alexander, and H. H. Hendon, 2004: Remote response of the Indian Ocean to interannual SST variations in the tropical Pacific. *J. Climate*, **17**, 362–372.
- Shongwe, M. E., W. A. Landman, and S. J. Mason, 2006: Performance of recalibration systems for GCM forecasts for southern Africa. *Int. J. Climatol.*, **26**, 1567–1585.
- Simmons, A., S. Uppala, D. Dee, and S. Kobayashi, 2006: ERA-Interim: New ECMWF reanalysis products from 1989 onwards. ECMWF Newsletter 110, ECMWF, Reading, UK.
- Slater, A. G., C. A. Schlosser, C. E. Desborough, A. J. Pitman, A. Henderson-Sellers, A. Robock, K. Y. Vinnikov, K. Mitchell, A. Boone, H. Braden, F. Chen, P. M. Cox, P. de Rosnay, R. E. Dickinson, Y. J. Dai, Q. Duan, J. Entin, P. Etchevers, N. Gedney, Y. M. Gusev, F. Habets, J. Kim, V. Koren, E. A. Kowalczyk, O. N. Nasonova, J. Noilhan, S. Schaake, A. B. Shmakin, T. G. Smirnova, D. Verseghy, P. Wetzell, Y. Xue, Y. Z. L., and Q. Zeng, 2001: The representation of snow in land surface schemes: Results from PILPS 2(d). *J. Hydrometeor.*, **2**, 7–25.
- Smith, R., C. Tebaldi, D. Nychka, and L. O. Mearns, 2008: Bayesian modelling of uncertainty in ensembles of climate models. *J. Amer. Stat. Assoc.*, in press.
- Soden, B. J. and I. M. Held, 2006: An assessment of climate feedbacks in coupled ocean-atmosphere models. *J. Climate*, **19**, 3354–3360.
- Sterl, A., C. Severijns, H. Dijkstra, W. Hazeleger, G. J. van Oldenborgh, M. van den Broeke, G. Burgers, B. van den Hurk, van Leeuwen P. J., and P. van Velthoven, 2008: When can we expect extremely high surface temperatures? *Geophys. Res. Lett.*, **35**, L14703.

- Stott, P. A., D. A. Stone, and M. R. Allen, 2004: Human contribution to the european heatwave of 2003. *Nature*, **432**, 610–614.
- Tadross, M. A., B. C. Hewitson, and M. T. Usman, 2005: The interannual variability of the onset of the maize growing season over South Africa and Zimbabwe. *J. Climate*, **18**, 3356–3372.
- Tebaldi, C., K. Hayhoe, J. M. Arblaster, and G. A. Meehl, 2006: Going to the extremes: An intercomparison of model-simulated historical and future changes in extreme events. *Climate Change*, **79**, 185–211.
- Tebaldi, C., L. O. Mearns, D. Nychka, and R. L. Smith, 2004: Regional probabilities of precipitation change: A Bayesian analysis of multimodel simulations. *Geophys. Res. Lett.*, **31**, L24213, doi:10.1029/2004GL021276.
- Tebaldi, C. and B. Sanso, 2008: Joint projections of temperature and precipitation change from multiple climate models: a hierarchical Bayesian approach. *J. Roy. Stat. Soc.*, **172**, 83–106.
- Tebaldi, C., R. L. Smith, D. Nychka, and L. O. Mearns, 2005: Quantifying uncertainty in projections of regional climate change: a Bayesian approach to the analysis of multimodel ensembles. *J. Climate*, **18**, 1524–1540.
- Thompson, D. W. J. and J. M. Wallace, 2001: Regional climate impacts of the northern hemisphere annular mode. *Science*, **293**, 85–89, doi:10.1126/science.1058958.
- Todd, M. C. and R. Washington, 1999: Circulation anomalies associated with tropical-temperate troughs in southern africa and the south-west Indian Ocean. *Climate Dyn.*, **15**, 937–951.
- Todd, M. C., R. Washington, and P. I. Palmer, 2004: Water vapour transport associated with tropical-temperate trough systems over Southern Africa and the South-west Indian Ocean. *Int. J. Climatol.*, **24**, 555–568.
- Toothill, J., 2003: Central European flooding August 2002; An EQECAT Technical Report. World Wide Web, [http://www.absconsulting.com/resources/Catastrophe\\_Reports/flood\\_rept.pdf](http://www.absconsulting.com/resources/Catastrophe_Reports/flood_rept.pdf).
- Trenberth, K. E., 1991: Climate diagnostics from global analyses: Conservation of mass in ECMWF analyses. *J. Climate*, **4**, 707–722.
- 1999: Atmospheric moisture recycling: Role of advection and local evaporation. *J. Climate*, **12**, 1368–1381.

- Trenberth, K. E., D. P. Stepaniak and J. M. Caron, 2002: Accuracy of atmospheric energy budgets from analyses. *J. Climate*, **15**, 3343–3360.
- Trenberth, K. E., A. Dai, R. M. Rasmussen, and D. B. Parsons, 2003: The changing character of precipitation. *Bull. Amer. Met. Soc.*, **84**, 1025–1217.
- Trenberth, K. E., J. Fasullo, and L. Smith, 2005: Trends and variability in column integrated atmospheric water vapor. *Climate Dyn.*, **24**, 741–758.
- Tyson, P. D., T. G. J. Dyer, and M. N. Mametse, 1975: Secular changes in South African rainfall: 1880 to 1972. *Quart. J. Roy. Meteor. Soc.*, **101**, 817–833.
- Tyson, P. D. and R. A. Preston-Whyte, 2000: *The Weather and Climate of Southern Africa*. Oxford University Press, Cape Town, 396pp.
- Uppala, S., D. Dee, S. Kobayashi, P. Berrisford, and A. Simmons, 2008: Towards a climate data assimilation system: status update of ERA–Interim. ECMWF Newsletter 115, ECMWF, Reading, UK.
- Uppala, S. M., P. W. Kålberg, A. J. Simmons, U. An dræ, V. da Costa Bechtold, M. Fiorino, J. K. Gibson, J. Haseler, A. Hernandez, G. A. Kelly, X. Li, K. Onogi, S. Saarinen, N. Sokka, R. P. Allan, E. Anderson, K. Arpe, M. Balmaseda, A. C. M. Beljaars, L. van den Berg, J. Bidlot, N. Borman, S. Caires, A. Dethof, M. Dragosavac, M. Fisher, M. Fuentes, S. Hagemann, E. Hólm, B. J. Hoskins, L. Isaksen, P. A. E. M. Janssen, R. Jenne, A. P. McNally, J.-F. Mahfouf, J.-J. Mockette, N. A. Rayner, R. W. Saunders, P. Simon, A. Sterl, K. E. Trenberth, A. Untch, D. Vasiljevic, P. Viterbo, and J. Woollen, 2005: The ERA-40 re-analysis. *Quart. J. Roy. Meteor. Soc.*, **130**, 2961–3012.
- van Aalst, M. K., M. Helmer, C. de Jong, F. Monasso, E. van Sluis, and P. Suarez, 2007: Red cross/red crescent climate guide. Technical report, Red Cross/Red Crescent Climate Centre, The Hague, The Netherlands, 73pp.
- van den Brink, H., 2005: *Extreme winds and sea-surges in climate models*. Ph.D. thesis, University of Utrecht, 115pp.
- van den Dool, H., 2007: *Empirical methods in short-term climate prediction*. Oxford University Press, Oxford, 215pp.
- van den Dool, H. M. and J. L. Nap, 1985: Short and long range air temperature forecasts near an ocean. *Mon. Wea. Rev.*, **113**, 878–886.
- van den Hurk, B. and D. Jacob: 2009, The art of predicting climate variability and change. *Climate change and adaptation in the water sector*, F. Ludwig, P. Kabat, H. van Schaik, and M. van der Valk, eds., Earthscan, 9–22.



- van den Hurk, B. J. J. M., A. M. G. Klein Tank, G. Lenderink, A. P. van Ulden, G. J. van Oldenborgh, C. A. Katsman, H. W. van den Brink, F. Keller, J. J. F. Bessembinder, G. Burgers, G. J. Komen, H. W., and S. S. Drijfhout, 2006: KNMI climate change scenarios 2006 for the Netherlands. Technical Report WR-2006-01, KNMI.
- van Oldenborgh, G. J., 2005: Comment on 'predictability of winter climate over the North Atlantic European region during ENSO events'. *J. Climate*, **18**, 2770–2772.
- 2007: How unusual was autumn 2006 in Europe? *Clim. Past*, **3**, 659–668.
- van Oldenborgh, G. J., M. A. Balmaseda, L. Ferranti, T. N. Stockdale, and D. L. T. Anderson, 2005a: Did the ECMWF seasonal forecast model outperform statistical ENSO forecast models over the last 15 years? *J. Climate*, **18**, 3240–3249.
- 2005b: Evaluation of atmospheric fields from the ECMWF seasonal forecasts over a 15-Year period. *J. Climate*, **18**, 3250–3269.
- van Oldenborgh, G. J. and G. Burgers, 2005: Searching for decadal variations in ENSO precipitation teleconnections. *Geophys. Res. Lett.*, **32**, L15701, doi:10.1029/2005GL023110.
- van Oldenborgh, G. J., S. Y. Philip, and M. Collins, 2005c: El niño in a changing climate: a multi-model study. *Ocean Science*, **1**, 81–95.
- van Oldenborgh, G. J. and A. van Ulden, 2003: On the relationship between global warming in the Netherlands and changes in circulation in the 20th century. *Int. J. Climatol.*, **23**, 1711–1724.
- van Ulden, A. P. and G. J. van Oldenborgh, 2006: Large-scale atmospheric circulation biases and changes in global climate model simulations and their importance for climate change in Central Europe. *Atmos. Chem. Phys.*, **6**, 863–881.
- Vautard, R., P. Yiou, F. D'Andrea, D. D. Noblet, N. Viovy, C. Cassou, J. Polcher, P. Ciais, M. Kageyama, and Y. Fan, 2007: Summertime European heat and drought waves induced by wintertime Mediterranean rainfall deficit. *Geophys. Res. Lett.*, **34**, L07711.
- Vecchi, G. P. and B. J. Soden, 2007: Global warming and the weakening of the tropical circulation. *J. Climate*, **20**, 4316–4340.
- von Storch, H. and F. W. Zwiers, 1999: *Statistical Analysis in Climate Research*. Cambridge University Press, Cambridge, UK, 484pp.

- Walsh, J. E., W. H. Jasperson, and B. Ross, 1985: Influences of snow cover and soil moisture on monthly air temperature. *Mon. Wea. Rev.*, **113**, 756–768.
- Walsh, J. E., A. S. Phillips, D. H. Ports, and W. L. Chapman, 2001: Extreme cold outbreaks in the United States and Europe, 1948–99. *J. Climate*, **14**, 2642–2658.
- Walsh, J. E., D. R. Tucek, and M. R. Petersonvan, 1982: Seasonal snow cover and short-term climatic fluctuations over the United States. *Mon. Wea. Rev.*, **110**, 1474–1486.
- Ward, M. N., 1998: Diagnosis and short-lead time prediction of summer rainfall in tropical North Africa at interannual and multidecadal timescales. *J. Climate*, **11**, 3167–3191.
- Washington, R. and A. Preston, 2006: Extreme wet years over southern Africa : Role of Indian Ocean sea surface temperatures. *J. Geophys. Res.*, doi:10.1029/2005JD006724.
- Washington, R. and M. C. Todd, 1999: Tropical temperate links in southern Africa and Southwest Indian Ocean daily rainfall. *Int. J. Climatol.*, **19**, 1601–1616.
- Webster, P. J., A. M. Moore, J. P. Loschnigg, and R. R. Leben, 1999: Coupled ocean-atmosphere dynamics in the Indian Ocean during 1997–1998. *Nature*, **401**, 356–360.
- Wehner, M. F., 2004: Predicted twenty-first-century changes in seasonal extreme precipitation events in the Parallel Climate Model. *J. Climate*, **17**, 4281–4290.
- Weigel, A. P., M. A. Liniger, and C. Appenzeller, 2007: The discrete Brier and ranked probability skill scores. *Mon. Wea. Rev.*, **135**, 118–124.
- White, P. W., 2003: Part II: Data assimilation. IFS documentation cycle. Technical Report CY23r4, ECMWF, Shinfield Park, Reading, U.K., 126 pp.
- Wilks, D. S., 1995: *Statistical Methods in the Atmospheric Sciences: an Introduction*. Academic Press, San Diego, 464pp.
- World Bank, 2006: *Kenya Adaptation to Climate Change in Arid Lands (KACCAL)*, GEF Project Brief. World Bank, Washington DC.
- Xoplaki, E., J. Luterbacher, H. Paeth, D. Dietrich, N. Steiner, and M. Grosjean, 2005: European spring and autumn temperature variability and change of extremes over the last half millennium. *Geophys. Res. Lett.*, **32**, doi:10.1029/2005GL023424.

- Yang, F., A. Kumar, W. W., H. M. H. Juang, and M. Kanamitsu, 2001: Snow-albedo feedback and seasonal climate variability over north america. *J. Climate*, **14**, 4245–4248.
- Yiou, P., R. Vautard, P. Naveau, and C. Cassou, 2007: Inconsistency between atmospheric dynamics and temperatures during the exceptional 2006/07 fall/winter and recent warming in europe. *Geophys. Res. Lett.*, **34**, doi:10.1029/2007GL031981.
- Yukimoto, S. and A. Noda, 2001: Improvements of the Meteorological Research Institute global ocean-atmosphere coupled GCM(MRI-CGCM2) and its climate sensitivity. *CGER Supercomputer activity report*, **10**, 37–44.
- Zeng, N., J. D. Neelin, K.-M. Lau, and C. J. Tucker, 1999: Enhancement of interdecadal climate variability in the Sahel by vegetation interaction. *Science*, **286**, 1537–1540.
- Zhang, X., F. W. Zwiers, G. C. Hegerl, F. H. Lambert, N. P. Gillett, S. Solomon, P. A. Stott, and T. Nozawa, 2007: Detection of human influence on twentieth-century precipitation trends. *Nature*, doi:10.1038/nature06025.
- Zhang, Y., T. Li, and B. Wang, 2004: Decadal change of the spring snow depth over the Tibetan Plateau: The associated circulation and influence on the East Asian summer monsoon. *J. Climate*, **17**, 2780–2793.
- Zveryaev, I. I. and R. P. Allan, 2005: Water vapor variability in the tropics and its links to dynamics and precipitation. *J. Geophys. Res.*, **110**, doi:10.1029/2005JD006033.
- Zveryaev, I. I. and P.-S. Chu, 2003: Recent climate changes in precipitable water in the global tropics as revealed in National Centers for Environmental Prediction/National Center for Atmospheric Research reanalysis. *J. Geophys. Res.*, **108**, doi:10.1029/2002JD002476.

### *Samenvatting*

In dit proefschrift worden klimaatextremen onderzocht die een aantal maanden duren. De focus ligt op de mechanismen die ze veroorzaken, hun voorspelbaarheid en hun verwachte respons op de opwarming van de aarde. Om ons doel te bereiken zijn waarnemingen, heranalyses, model simulaties en verwachtingen geanalyseerd. Klimaatmodellen zijn nog niet in staat het gedrag van het klimaatstelsel voor elk seizoen even nauwkeurig te reproduceren. De prestaties van het model hangen ook af van de meteorologische variabele waarin men geïnteresseerd is. Zo presteren modellen over het algemeen beter op temperatuurverwachtingen dan op neerslagverwachtingen. De centrale focus van dit proefschrift is daarom op de specifieke seizoenen waarin de klimaatextremen gewoonlijk plaatsvinden. In het licht van de veranderingen in het klimaat en de recente ongekeerde seizoenextremen hebben klimaatmodellen in principe een duidelijk voordeel boven puur statistische methoden, met name de lineaire, in de lange-termijn verwachtingen van extremen. Om echter waardevolle seizoensverwachtingen te maken is een adequate weergave van de fysische processen en terugkoppelingen die aan de klimaatextremen ten grondslag liggen noodzakelijk.

In **Hoofdstuk 2** hebben we de belangrijkste drijvende krachten achter de extreem milde herfst in 2006 in Europa onderzocht en geïdentificeerd. We hebben met een degelijke onderbouwing aangetoond dat anomale turbulente warmtefluxen aan de oppervlakte over het centrum van de Noord-Atlantische Oceaan een belangrijke rol hebben gespeeld in het forceren van deze extreme gebeurtenis, iets wat in voorgaande studies niet aan de orde is gesteld. In deze studies was aangenomen dat het warme oceaanooppervlak voor de kust van Noord-Afrika de energie verschaft die door de zuidwestelijke stroming tot in Europa werd meegevoerd. Onze resultaten laten echter duidelijk zien dat deze aanname onjuist is. Binnen Europa droeg de waterdamp-feedback in de relatief vochtige lucht extra bij om de verwarming te versterken.

De persistentie van de warmtefluxanomalieën aan de oppervlakte in de Noord-Atlantische Oceaan en hun link met de ongekeerde temperatuur-anomalieën leveren een bemoedigend vooruitzicht op het gebied van de voorspelbaarheid van extreme seizoenen in Europa. Wanneer enige voorspelbaarheid van extreme oppervlakte condities van het Noord-Atlantisch gebied (zoals tijdens de herfst in 2006) wordt verondersteld, valideren onze resultaten voorgaande bevindingen (Czaja and Frankignoul, 1999). Deze stelden dat de Noord-Atlantische Oceaan een merkbare invloed uitoefent op het Europees klimaat in de herfst. Dat dit ongeëvenaard extreme seizoen voornamelijk het resultaat is van de atmosferische circulatie en ge-parameteriseerde processen (zoals energiefluxen aan het oppervlak, de overdracht van stralingsenergie, convectie en condensatie) laat zien dat een realistische weergave van deze processen van groot belang is voor het voorspelbaarheid-

sprobleem.

In **Hoofdstuk 3** wordt een verband gelegd tussen de voorspelbaarheid van extreem koude lentes in Europa enerzijds en hydrologische en energieprocessen aan het oppervlak anderzijds. Onze bevindingen benadrukken het belang van een nauwkeurige representatie van sneeuwprocessen gedurende het smeltseizoen voor zinvolle verwachtingen van koude lentes in Europa door numerieke seizoensverwachtingsmodellen. Een analyse van waarnemingen toont aan dat landoppervlakforceringen door sneeuw een merkbare, vertraagde invloed uitoefenen op de temperatuur in het voorjaar. Deze forcering kan dus een voorspelbaarheidssignaal verschaffen in het oosten van Europa. Jaren met wijdverbreide sneeuw in februari en maart worden in de buurt van de sneeuwzone relatief vaak gevolgd door een koud voorjaar. Deze sneeuwforcering, die de oppervlakte-energiebalans verandert, kent een aantal mechanismen die uitvoerig in de literatuur zijn gedocumenteerd (bijvoorbeeld Cohen and Rind, 1991). In de gebieden waar de hoogste voorspellende waarde wordt gevonden in de best presterende modellen is de invloed van sneeuw over het algemeen het grootst gedurende het voorjaar. De kwaliteit van de verwachtingen voor koude seizoenen is beter dan de verwachtingen voor bijna gemiddelde en warme seizoenen. We hebben aangetoond dat de best presterende modellen een realistischer sneeuwseizoen hebben, vooral gedurende het cruciale smeltseizoen. Deze studie laat zien dat een betere en uitgebreidere nabootsing van de land-atmosfeer processen die betrekking hebben op sneeuw waarschijnlijk resulteren in betere verwachtingen voor koude lentes in Europa.

In **Hoofdstuk 4** presenteren we scenario's voor klimaatverandering in zuidelijk Afrika. Ondanks de inherente onzekerheden komen bepaalde kenmerken redelijk overeen tussen de modellen onderling. Ten eerste vinden we een consistente verkorting van het regenseizoen in zuidelijk Afrika, ten zuiden van ongeveer 15° Z. Dit wordt zowel veroorzaakt door een verlate aanvang van de regenval alsook een vroege beëindiging in de modelsimulaties die voor het vierde IPCC Assessment Report gemaakt zijn. We veronderstellen dat een verandering in het vochtpatroon in de lage troposfeer, dat wordt getransporteerd door de gemiddelde circulatie, van cruciaal belang is in de beperkte neerslagvorming in het begin van het seizoen. Een drogere bodem in de vorige winter speelt een ondergeschikte rol, omdat lokale vochtrecycling in het voorjaar te zwak blijkt te zijn. In de tweede plaats is er een regionaal patroon gevonden tijdens de zuidelijke zomermaanden (d.w.z. de piek van het regenseizoen) dat vergelijkbaar is met het rijk-wordt-rijker-mechanisme (Chou et al., 2009) en gekenmerkt wordt door uitdroging boven semi-aride gebieden dichtbij de Kalahari woestijn en vernatting ten noorden van 15° Z. Dichtbij de Kalahari valt een aanzienlijke daling in de gemiddelde seizoensgebonden neerslag samen met een verandering naar ernstigere één-in-tien-jaar droogtes. De kans op uitbreiding van het woestijngebied is daarom hoog. Ten derde blijft de laagfre-

quente neerslagvariabiliteit een prominent kenmerk in de toekomstige tijdreeksen van zuidelijk Afrika. In de uitdrogende gebieden zal de neerwaartse trend pas na 2050 waarneembaar zijn boven de natuurlijke variaties.

Hoewel niet onweerlegbaar, suggereren onze bevindingen dat het toekomstige gedrag van trogsystemen in de subtropen hierin waarschijnlijk een rol speelt. Omdat er tussen de geselecteerde klimaatmodellen echter onvoldoende overeenstemming bestaat, blijft het vooralsnog onduidelijk welke fysische mechanismen verantwoordelijk zijn voor de verandering van het dipoolpatroon in de zomerneerslag (december tot februari) in zuidelijk Afrika.

Een belangrijke bevinding in **Hoofdstuk 5** is een robuuste toename van de neerslag in Oost-Afrika ten opzichte van andere regio's binnen dezelfde lengtegordel. Bijna overal in Oost-Afrika wordt een positieve verschuiving van de gehele kansdichtheidsfunctie voor neerslag voorspeld. In de gebieden waar twee keer per jaar meer regen valt door het overtrekken van de ITCZ (de regenzone in de tropen die met de zon mee naar het noorden en zuiden trekt) zijn neerslagtoenames berekend, zowel tijdens de korte als tijdens de lange regenperiodes. Soortgelijke verandering in regenval worden gesimuleerd in het gebied waar het één keer per jaar meer regent, in de lokale zomer. De toename is daar tijdens de zomer en najaar (onze winter en lente). Gemiddelde neerslagtoenames worden heel vroeg in de eenentwintigste eeuw zichtbaar, wat in kwalitatief opzicht overeenkomt met de waarnemingen van de afgelopen jaren.

De geselecteerde IPCC AR4 modellen zijn in staat om de bekende empirische relatie in ons najaar tussen de oost-west SST gradiënten in de tropische Indische Oceaan en de korte regens in Oost-Afrika te reproduceren: als het zeewater in het westen van de Indische Oceaan warmer is regent het meestal meer in Oost-Afrika in oktober–november. Dit wordt de IOZM genoemd, de Indische Oceaan Zonale Modus (IOZM). De gesimuleerde neerslagveranderingen worden tot op zekere hoogte door veranderingen in dezelfde SST gradiënten en dus de IOZM bepaald. In ons najaar neemt de verschijningskans van de IOZM toe onder opwarming van de aarde: de westelijke Indische Oceaan wordt vaker warm ten opzichte van de oostelijke kant. In deze situatie veroorzaken afwijkingen in de warmtestromen over het oppervlak meer regen boven het warme water in de westelijke tropische Indische Oceaan en krachtigere lage oostelijke winden over dit gebied. Dit fenomeen, dat bekend is uit observaties en modelstudies, wordt op een adequate wijze gerepresenteerd door het merendeel van de geselecteerde IPCC AR4 modellen. Omdat dit teleconnectiepatroon de interjaarlijkse variabiliteit in regenval in Oost-Afrika beïnvloedt, kan men concluderen dat klimaatverandering voor een aanzienlijk deel gelijkenis vertoont met de interjaarlijkse variabiliteit in het huidige klimaat.

In de verschillende delen in dit proefschrift zijn we verder gegaan dan alleen

een statistische analyse van seizoensextremen en hebben we er ook een fysische verklaring van gegeven. We hebben laten zien dat de huidige numerieke seizoensverwachtingsmodellen betere voorspellingen van deze extremen zouden kunnen geven als de onderliggende fysische mechanismen beter gerepresenteerd zouden worden in die modellen. Daarnaast zijn toekomstige veranderingen in de stralingsforcering van de aarde gerelateerd aan veranderingen in de gemiddelde en extreme neerslag in grote delen van Afrika ten zuiden van de Sahara. De projecties van het toekomstige regenklimaat in Afrika zijn bestudeerd als deel van een onderzoeksproject in samenwerking met het Rode Kruis/ Rode Halve Maan Klimaatcentrum. Andere resultaten van dit project zijn beschikbaar op de KNMI web site ([http://www.knmi.nl/africa\\_scenarios/](http://www.knmi.nl/africa_scenarios/)). We verwachten dit het begin is van een proces van validatie met betere modellen en waarnemingen dat zal bijdragen aan de wereldwijde wetenschappelijk inspanningen om klimaatextremen beter te voorspellen.

## ACKNOWLEDGMENTS

It is by the grace of THE ALMIGHTY GOD that I have been able to successfully undertake this PhD research. I give glory first and foremost to LORD for HIS divine help that has seen me through this study programme. I share the same testimony with the Psalmist who says "I will lift up mine eyes unto the hills, from whence cometh my help. My help cometh for THE LORD, which made heaven and earth." I also thank the THE ALMIGHTY for his mercy upon my life. It is written "For HE saith to Moses, I will have mercy on whom I will have mercy, and I will have compassion on whom I will have compassion. So then it is not of him that willeth, nor of him that runneth, but of GOD that sheweth mercy", Romans 9:15–16. Lastly, I would like to thank my GOD for the divine favour I have enjoyed throughout my stay in The Netherlands. I join the Psalmist to declare that "LORD, by thy favour thou hast made my mountain to stand strong... For I have not achieved anything by my own sword, neither did my own arm save me: but thy right hand, and thine arm, and the light of thy countenance because thou hadst a favour unto me."

I thank my Divinely appointed Mentor and Spiritual Father, Bishop David Oyedepo, who continues to be my source of inspiration in life.

I am profoundly grateful to Dr. Geert Jan van Oldenborgh, my co-promoter for his mentorship, unwaivering support, and all forms of encouragement throughout the course of my PhD work. Through Geert Jan's support and recommendations, I have been privileged to attend several summer schools, taught courses, workshops and conferences, from which I have learned a lot. I also thank his family for hosting me upon my arrival and for providing all the support I needed after losing most of my belongings en-route to The Netherlands.

I am indebted to my promoter Prof. Bart van den Hurk who has guided me through this work and whose contribution substantially improved the articles constituting this thesis.

I also would like to gratefully acknowledge the technical assistance I received from Henk van den Brink during the course of my research work.

Melanie Schultz is thanked for facilitating the creation of the PhD research position as an 150 year anniversary present to KNMI.

We acknowledge the modeling groups, the Program for Climate Model Diagnosis



and Intercomparison (PCMDI) and the WCRP's Working Group on Coupled Modelling (WGCM) for their roles in making available the WCRP CMIP3 multi-model dataset. Support of this dataset is provided by the Office of Science, U.S. Department of Energy.

I have substantially benefitted from collaboration with Rune Graversen (KNMI, The Netherlands), Chris Ferro (Exeter, UK), Caio Coelho (CPTEC, Brazil), Francisco Doblas-Reyes (ECWMF, UK), Maarten van Aalst (Netherlands Red Cross/Red Crescent Climate Centre) and Bas de Boer (University of Utrecht, The Netherlands). Special thanks are expressed to Prof. Willem Landman for the unwavering support he has rendered before and during my PhD study.

I also express my heartfelt appreciation to Brigitta Kamphuis for helping with all the administrative work and to Leo Dogterom Verburg for recovering my data after my disk crashed. Many thanks also to all colleagues and senior scientists I have been privileged to interact with at KNMI. In particular, I thank Gerrit Burgers, Wilco Hazeleger, Rein Haarsma, Otto Hooghoudt, Pui-Kei Fung, Wim-Paul Breugem, Robert Leander, Astrid Manders and Sjoukje Philip for the help and support they have rendered from time to time.

## CURRICULUM VITAE

Mxolisi Excellent Shongwe was born in Mfabantfu, Manzini District, Swaziland on 04 March 1970. He attended high school at Mankayane High School from 1987 to 1988. In May 1991, he was employed by the Civil Service of The Kingdom of Swaziland, Department of Civil Aviation as a meteorological assistant based at Matsapha Airport.

From January 1993, Mxolisi attended a one-year World Meteorological Organization (WMO) Class III course at the Institute for Meteorological Training and Research (IMTR) in Nairobi, Kenya. From January 1995, he attended a two-year WMO Class II course at IMTR. From September to December 1998, he was attached to the African Desk under the National Centers for Environmental Prediction (NCEP), Maryland, United States. From February to July 2000, he was attached to the African Centre of Meteorological Applications for Development (ACMAD), Niger. From October 2000, he enrolled at the University of Nairobi (UON), Kenya for a BSc. degree in Meteorology. He graduated at the UON in May 2004. Between July 2003 and September 2004, he was a World Meteorological Organisation (WMO) Consultant at the Southern African Development Community (SADC) Drought Monitoring Centre (DMC), Harare, Zimbabwe. While at SADC DMC, he registered at the University of Pretoria for an MSc. degree, which he did on a part-time basis.

In September 2005, Mxolisi started working on his PhD at KNMI, Netherlands working on seasonal climate extremes. This research produced four publications, which have been presented in this thesis.

## PUBLICATIONS

**Shongwe, M. E.**, R. G. Graversen, G. J. van Oldenborgh, B. J. J. M. van den Hurk and F. J. Doblas-Reyes, 2009: Energy budget of the extreme Autumn 2006 in Europe. *Climate Dyn.*, (doi:10.1007/S00382-009-0689-2; Chapter 2 of this thesis).

**Shongwe, M. E.**, G. J. van Oldenborgh, B. J. J. M. van den Hurk, B. de Boer, C. A. S. Coelho and M. K. van Aalst, 2009: Projected changes in mean and extreme precipitation in Africa under global warming. Part I: Southern Africa. *J. Climate*, **22**, 3819–3837. (Chapter 4 of this thesis).

**Shongwe, M. E.**, G. J. van Oldenborgh, B. J. J. M. van den Hurk and M. K. van Aalst, 2008: Projected changes in mean and extreme precipitation in Africa under global warming. Part II: East Africa. *J. Climate* (submitted; Chapter 5 of this thesis).

**Shongwe, M. E.**, C. A. T. Ferro, C. A. S. Coelho and G. J. van Oldenborgh, 2007: Predictability of cold spring seasons in Europe. *Mon. Wea. Rev.* **135**, 4185–4201. (Chapter 3 of this thesis).

**Shongwe, M. E.**, W. A. Landman and S. J. Mason, 2006: Performance of recalibration systems for GCM forecasts for southern Africa. *Int. J. Climatol.* **26**, 1567–1585.

Landman, W. A., S. Botes, L. Goddard and **M. Shongwe**, 2005: Assessing the predictability of extreme rainfall seasons over southern Africa. *Geophys. Res. Lett.*, **32**, L23818, doi:10.1029/2005GL023965.